

MANUFACTURE OF INFRARED OPTICS IN BRITTLE MATERIALS

by

Joseph Daniel Owen

A dissertation submitted to the faculty of
The University of North Carolina at Charlotte
in partial fulfillment of the requirements
for the degree of Doctor of Philosophy in
Mechanical Engineering

Charlotte

2015

Approved by:

Dr. Matthew A. Davies

Dr. Christopher J. Evans

Dr. Thomas J. Suleski

Dr. Tony L. Schmitz

Dr. Angela Davies

©2015
Joseph Daniel Owen
ALL RIGHTS RESERVED

ABSTRACT

JOSEPH DANIEL OWEN. Manufacture of infrared optics in brittle materials. (Under the direction of DR. MATTHEW A. DAVIES)

Infrared optics are manufactured for many different applications including: thermal imaging, surveillance, night vision, medical, laser machining, laser surgery, etc. Most infrared transparent materials are hard, brittle, or both. Unless special conditions are generated, diamond machining will lead to surfaces dominated by brittle fracture. The overall purpose of this dissertation is to further the state-of-the-art of infrared optics manufacturing. The first piece of this dissertation is to explore the ductile-brittle behavior of two different infrared materials: germanium and IRG 26 (a chalcogenide glass by Schott). These two materials are very useful IR materials: germanium for its high index of refraction and IRG 26 for its low glass transition temperature allowing for easy molding. The cutting mechanics for these materials was experimentally observed during a series of different cutting operations: face turning, planing/ruling, orthogonal turning, and ball milling. Cutting and thrust forces were measured and analyzed for the force coefficients as a function of the cutting parameters. The cutting force coefficients were found to have a significant drop as the cutting mechanics became increasingly brittle with higher chip thicknesses. The reduced cutting forces at more aggressive parameters could lead to a means of rapid prototyping of IR optics. The second piece of this dissertation is to outline a procedure developed to correct tool errors of a diamond ball mill. Two dominant tool shape errors of a ball mill are diamond position and cutting edge irregularity. An artifact based procedure was used to imprint the tool errors on a measureable part.

DEDICATION

I would like to dedicate this work to my wife Allison who has stood by and supported me through the years while I pursued degree after degree. I could not have done this without her. I would also like to dedicate this to my mother Kathleen who has always been a source of encouragement for me throughout my education.

ACKNOWLEDGMENTS

I am very grateful to my committee chairman, Professor Matthew A. Davies, without whose dedication and encouragement I could not have succeeded in completing my dissertation. Hopefully, one day I will be as inspiring a mentor as he was to me. I am also grateful to my committee members, Professors Chris Evans, Thomas Suleski, and Tony Schmitz, for their support and help in writing this dissertation. Dr. Chris Evans and Dr. Thomas Suleski have been a wealth of knowledge for me throughout my research.

I would like to thank the UNC Charlotte machine shop staff for encouraging my interest in machining: Joel Pritchard, Brian Dutterer, Roland Hege, and Joe Dalton. Their expertise and guidance throughout my education was the foundation for my passion in manufacturing. Dr. Jimmie Miller also deserves special thanks for the many hours I spent in his office with my endless questions. I would also like to thank my lab and research mates Jenn, Alex, Luke, Bryan, Paul, and Daniel.

For financial support I would like to thank the National Science Foundation, the II-VI Foundation, the Center of Freeform Optics, and the Center of Precision Metrology.

Last, I would like to thank Mr. Hudson Welch and DigitalOptics Corporation for the opportunity to experience the advanced training of an industrial company. I could not be where I am today without the knowledge and experience I gained from my time working there. Special thanks go to my co-workers Adam and Greg and to my manager David.

TABLE OF CONTENTS

| | |
|----------------------------------------------------|----|
| LIST OF ABBREVIATIONS | x |
| CHAPTER 1: BACKGROUND AND MOTIVATION | 1 |
| 1.1 Introduction | 1 |
| CHAPTER 2: EQUIPMENT AND EXPERIMENTAL SETUP | 9 |
| 2.1 Introduction | 9 |
| 2.2 Facilities and Equipment | 9 |
| 2.2.1 Metrology Lab | 9 |
| 2.2.2 Diamond Turning/Milling Machine. | 9 |
| 2.2.3 Dynamometer | 10 |
| 2.2.4 Cutting Fluids | 11 |
| 2.2.5 Data Acquisition and Analysis | 11 |
| 2.2.6 Surface Metrology | 12 |
| 2.3 Experimental Setup | 13 |
| 2.3.1 Orthogonal Turning | 13 |
| 2.3.2 Face Turning | 15 |
| 2.3.3 Ruling | 16 |
| 2.3.4 Ball End-Milling | 17 |
| CHAPTER 3: DIAMOND MACHINING OF CHALCOGENIDE GLASS | 19 |
| 3.1 Introduction | 19 |

| | |
|-------------------------------------------------------|-----|
| | vii |
| 3.2 Experimental Summary | 20 |
| 3.3 Orthogonal Cutting | 20 |
| 3.3.1 Force Versus Chip Thickness With Constant Speed | 20 |
| 3.3.2 Force Versus Speed With Constant Chip Thickness | 24 |
| 3.3.3 Hysteresis | 26 |
| 3.4 Face Turning | 30 |
| 3.5 Ball End-Milling | 35 |
| CHAPTER 4: DIAMOND MACHINING OF GERMANIUM | 40 |
| 4.1 Introduction | 40 |
| 4.2 Ruling of Germanium | 41 |
| 4.2.1 Experiment Description | 42 |
| 4.2.2 Results | 44 |
| 4.2.3 Analysis | 47 |
| 4.2.4 Discussion | 52 |
| 4.3 Orthogonal Turning of Germanium | 53 |
| 4.3.1 Experimental Description | 53 |
| 4.3.2 Results | 54 |
| 4.3.2.1 Force Versus Chip Thickness | 54 |
| 4.3.2.2 Force Versus Speed | 57 |
| 4.3.2.3 Force Versus Spindle Position | 61 |

| | |
|-------------------------------------------------------|------|
| | viii |
| 4.3.3 Analysis | 63 |
| CHAPTER 5: TOOL ERROR CORRECTION | 65 |
| 5.1 Introduction | 65 |
| 5.2 Sources of Tool Errors | 65 |
| 5.2.1 Tool Location Error | 66 |
| 5.2.2 Diamond Waviness | 67 |
| 5.3 Measuring Tool Errors | 67 |
| 5.3.1 Calibration Artifact | 68 |
| 5.3.2 Metrology of Calibration Artifact | 70 |
| 5.4 Analysis of the Calibration Artifact Measurement | 70 |
| 5.5 Tool Path Generation | 77 |
| 5.6 Tool Path Validation | 82 |
| 5.7 Additional Sources of Error | 83 |
| CHAPTER 6: APPLICATION | 85 |
| 6.1 Making Optics | 85 |
| 6.2 Aspheric Thermal Landscape Imaging Lens in IRG 26 | 85 |
| 6.2.1 Characteristics of Final Component | 90 |
| 6.3 Higher Order Alvarez Freeform in IRG 26 | 92 |
| 6.4 Extreme Freeform Twisted Pyramid | 96 |
| CHAPTER 7: DISCUSSION AND CONCLUSIONS | 97 |

| | |
|--------------------------------------|-----|
| | ix |
| 7.1 Summary | 97 |
| 7.2 Future Work and Open Questions | 98 |
| 7.2.1 High Speed Machining | 98 |
| 7.2.2 Dead Sharp Grooves | 99 |
| 7.2.3 Speed Dependence | 99 |
| 7.2.4 Fracture Depth Prediction | 100 |
| 7.2.5 Rake Angle Variations | 100 |
| 7.2.6 Interrupted Cutting | 100 |
| REFERENCES | 102 |
| APPENDIX A: MATLAB CODE | 107 |
| A.1 Setup Sphere Analysis Code | 107 |
| A.2 Setup Sphere Tool Path Generator | 114 |
| A.3 Best Fit Sphere | 120 |
| A.4 ROCKpoly | 120 |
| A.5 ROCKpolySlope | 121 |
| A.6 Torus_center_yawed_Zeroed | 121 |
| A.7 Zernpolyfitn | 123 |
| A.8 Zernpolyvaln | 126 |

LIST OF ABBREVIATIONS

| | |
|-------|--------------------------------------------------------------------------|
| fpr | feed per revolution |
| TNR | tool nose radius |
| F_c | cutting force |
| F_t | thrust force |
| K_c | cutting force coefficient |
| K_t | thrust force coefficient |
| F | friction force |
| N | normal force |
| T_g | glass transition temperature |
| t_c | chip thickness |
| LWIR | long wave infrared (8 μm – 12 μm wavelength light) |

CHAPTER 1: BACKGROUND AND MOTIVATION

1.1 Introduction

For centuries, most optical devices have consisted predominantly of combinations of spherical and flat components due to the relative ease of manufacture. However, recent advances in manufacturing equipment and software for simulation and manufacturing of optics now make it possible to implement optimized freeform optical designs that can arbitrarily redirect light in three-dimensions. In fact, freeform optics appear poised to radically change optical designs in many areas ranging from imaging to light management, with applications in consumer electronics, night vision, surveillance, directed lighting, medical testing, etc. [1]. Advantages of integrating freeform surfaces with optics include: (1) the ability to replace multiple traditional optics with a single freeform; (2) the capability to simultaneously machine an optical surface with precision alignment features; and (3) the capability to accomplish new optical functions, such as in the Alvarez lens [2]. However, freeform optics presents manufacturing and metrology challenges. There are examples in the literature of freeform lens manufacturing [3] [4] [5] [6] [7] [8].

Ultra-precision diamond machining and freeform milling are paths to production, particularly for infrared (IR) applications where form and finish requirements are less stringent than for visible light applications [9] [10]. To achieve this, cutting under the complex geometric and dynamic conditions encountered in freeform milling must be

predicted and controlled. This requires improved understanding of the cutting mechanics of brittle IR-materials.

For decades, it has been known that brittle materials can be successfully diamond turned [11] [12] [13] [14] [15] [16] [17] [18] [19] [20] [21] [22] [23]. Although the mechanics are not fully understood, the practical ramifications of this are substantial. Germanium optics for infrared imaging systems have been diamond turned for decades. Other IR materials such as zinc selenide, cadmium telluride, zinc sulfide [24] and in some cases silicon can be successfully turned to produce complex optics for IR systems. More recently chalcogenide glasses have become important for infrared imaging. These materials, containing one of the three elements: sulfur, selenium, or tellurium, can also be diamond turned [25]. As optics become more complex, for example *freeform optics*, it becomes more important to understand the mechanics of so-called “ductile-regime” and “brittle-regime” cutting especially under complex geometric and/or dynamic conditions.

This dissertation focuses on the cutting mechanics of two important brittle IR materials: germanium and chalcogenide glass. The results of simplified cutting geometries are used to understand the mechanics of more complex milling geometries, and two applications are presented.

As stated, ductile/curly chips can be formed when cutting brittle materials, a phenomenon that has been observed for over a century [26] [27] [28]. Scientific study of the phenomenon is more recent. Citing the indentation literature [29] [30], Giovanola et al. [15], Nakasuji et al. [31] and Blake et al. [12] proposed that ductile chip formation can occur when the material is under high hydrostatic pressure and when the chip thickness are below a critical value dependent upon material properties. Under these conditions,

optical quality surfaces can be obtained in crystalline materials important for IR-imaging such as germanium [32] [33]. Optical glasses have also been the subject of diamond turning investigations (e.g. [15] [34] [35]).

Some researchers, chiefly led by Scattergood and co-workers, postulate a transition from a ductile chip formation mechanism at some critical length scale - typically the local uncut chip thickness [12] [36]. They further postulate that above a critical chip thickness, fractures forming ahead of the tool begin to propagate into the surface ahead of the tool. If the fracture is severe enough, the tool does not fully remove the damaged material, and a surface with fractures remains behind [12]. Other researchers, for example Lucca et al. [14], postulate that surface fractures form behind the tool due to the stress state. They showed that when the resultant cutting force vector rotates to produce tensile stresses behind the tool, surface fracture will be initiated. While there remains disagreement over whether a truly “ductile mode” of cutting exists, researchers do agree that hydrostatic pressure, often generated by a tool with a negative rake angle, will suppress fracture and some brittle materials may be cut to leave a surface free of visible fracture damage.

For the purposes of this dissertation, we define ductile-mode machining as a process where the chip formation in the cutting operation is similar to that of metal machining. The material is plastically deformed and flows off the rake face of the tool forming chips that appear similar to those obtained in the conventional machining of metals [34]. Further, the surface forms a structure that replicates the tool path – for example forming a cusp structure in turning with a round nosed tool – and the surface is free of significant surface fracture. As described in this dissertation, special care must be

taken to achieve this type of machining in a brittle material, and the behavior is dependent on the properties of the material being cut. The opposite of “ductile-mode” machining is “brittle-mode” or “fracture-dominated” machining where the chips are rough, fractured chunks of material that predominately underwent elastic deformation followed by fracture. The research literature cites many examples [15] [31] [12] [32] [33] [34] [36] [14] [11] [13] [16] [17] [37] [38] [39] [40] of an apparent transition, as a function of certain machining parameters, between “brittle mode” and “ductile-mode” machining. Examples show that when a critical value of a certain parameter is exceeded, brittle fracture will be apparent on the finished surface, whereas if a critical value is not exceeded a “smooth” fracture-free surface is achieved [12]. The combinations of parameters that produce a fracture-free surface are typically empirically determined. While there has been a qualitative link made between the nano-indentation literature and “ductile machining” behavior that relates the critical machining parameters to material properties [12] [34], there is no generic formula to determine the machining parameters that produce a surface free of fracture in a brittle material.

One reason an analytical solution to the problem has eluded researchers is that the number of free parameters even in a simple turning operation is large. These include tool nose radius, tool edge radius, rake angle, cutting speed, cutting fluid, workpiece material, depth of cut, and feed per revolution. Environmental conditions can play a role in the machining process as well. The most commonly varied parameters are: tool radius, rake angle, depth of cut, and feed per revolution. Research has focused on two main quantities that can be derived from these, the local rake angle and the uncut chip thickness. The common consensus in literature is that a negative rake angle tool will generate increased

hydrostatic pressure in the cutting region, suppressing fracture while a ductile chip formation is generated. Without the hydrostatic pressure, the force required to fracture the material is less than the force required to plastically deform the chip [14] and thus brittle fracture will be the more energetically favorable mode of deformation/material removal. Based on the indentation literature [29] [30] [41], several attempts have been made to connect the indentation depth at which fracture is initiated to a critical uncut chip thickness at which brittle machining will ensue. Other researchers surmise that it is the change in the force system during machining and in particular a rotation of the resultant cutting force vector that leads to a tensile stress behind the tool and surface fractures occurring after the cutting tool has passed. Although these viewpoints are not necessarily incommensurate, a “unified” view of “ductile mode” machining does not currently exist.

Ductile-mode machining has also been reported in the literature in diamond milling [42] [43] [44] [45] [46] [47] [48]. The authors report an increase in brittle fracture with an increase in uncut chip thickness. This is consistent with the turning of brittle materials literature mentioned above. Matsumura et al. [43] showed an increase of cutting force as the chip thicknesses increased until fracture occurs and the force stops increasing and becomes more chaotic.

We have conducted simplified orthogonal cutting experiments to add to the understanding of these complex mechanics. As was first pointed out in the metal cutting literature by Merchant [49] and later elaborated by Shaw [30] and others [50], the complexities inherent in a practical machining operation can be simplified using two dimensional, orthogonal cutting tests. In this arrangement, the deformation occurs in a nearly plain strain configuration, and only two cutting force components are required to

describe the macroscopic cutting behavior. The forces on the tool parallel and perpendicular to the cutting direction are measured, and these are termed the cutting force F_c and thrust force F_t , respectively [35]. Reducing the cutting mechanics to two orthogonal forces simplifies the analysis of the machining operation. An orthogonal cutting test has a known, fixed width and a feed speed that creates a constant chip thickness. The uncut chip area is rectangular and is equal to the product of the chip width and the thickness. The measured force and the chip area are used to compute force coefficients. The force coefficient in the cutting direction is equal to the energy per unit volume of material removed and is often called the specific energy. In metals, the force coefficients typically remain roughly constant over a relatively large range of cutting parameters. The force coefficients will remain roughly constant if the mechanism of material removal – ductile flow – remains unchanged. Therefore, the force in more complex cutting operations can be predicted by so-called mechanistic models that integrate the differential force contributions over the uncut chip area.

In this dissertation, by conducting orthogonal cutting experiments on brittle material, we demonstrate drastic changes in cutting force coefficients not typical of metals. We surmise that these changes are related to fundamental changes in the cutting mechanics, and these changes can be linked to practical performance – surface quality. Further, when attempting to predict forces in more complex geometries such as milling and turning by mechanistic models [51] [52] [53] [54] [55], the local force coefficients must be used and a mechanistic model that integrates force contributions over a complex chip area requires a look-up table for the highly nonlinear and sometimes discontinuous cutting force coefficients. While the experimental results given here shed some light on

cutting mechanics in brittle materials, they also leave many unanswered questions that are subjects for future research.

While cutting mechanics are important, the production of freeform optics with tolerances in the range of $0.1\ \mu\text{m}$, also leads to challenges with machine programming and error compensation techniques. Many (most) commercial software packages aimed at cutting freeform surfaces do not have the fidelity to produce tool paths for optics machining. Freeforms cut for the die-mold industry do not require submicron tolerances, and so software packages were not designed for such a situation. Thus, to cut freeform optics, custom codes for tool path generation were developed as described in this thesis. Further, because freeform designs often require milling, error compensation techniques for turning are not fully applicable. This dissertation describes an artifact based technique for compensating for milling tool error akin to the techniques used for corrections tool centering errors in turning.

Understanding the programming, error compensation, and cutting mechanics then enables applications to novel freeform optics in IR-materials. The demonstration of the capability to manufacture near arbitrary freeform IR optics with form tolerances in the range of $0.1\ \mu\text{m}$ and local surface finish error in the range of $5\ \text{nm RMS}$ is a major research product of this dissertation.

This dissertation is arranged as follows. Chapter 2 summarizes the equipment and experimental arrangements used throughout. Chapter 3 gives the result on the diamond machining of chalcogenide glass. Chapter 4 shows results for diamond machining of germanium and notes the similarities and differences with the behavior of chalcogenide glass. In Chapter 5, tool error correction is discussed. Finally in Chapter 6 example

applications are discussed. We end with Chapter 7 where we summarize major conclusions and point toward future research.

The original contributions of this research are: (1) the demonstration of a force “jump” in chalcogenide glass which appears to correspond to a dramatic change in cutting mechanics; (2) the buildup of damage in orthogonal cutting of brittle material that leads to a gradual change in the cutting mechanics over time; (3) the mechanistic prediction of the forces associated with the turning and milling of a brittle material.

CHAPTER 2: EQUIPMENT AND EXPERIMENTAL SETUP

2.1 Introduction

Specialize equipment and tools were required to complete the work in this dissertation. The equipment was set up to conduct the experiments and research in this dissertation as described below.

2.2 Facilities and Equipment

2.2.1 Metrology Lab

The UNC Charlotte Mechanical Engineering building, Duke Centennial Hall, houses a 1500 sq. ft. climate controlled metrology lab with temperature controlled to $20^{\circ}\text{C}\pm 0.1^{\circ}\text{C}$. The metrology lab is also rated as a 10,000 class cleanroom with a maximum humidity of 50%. Relevant equipment housed in the metrology lab includes a Zygo NewView 5000 Scanning White Light Interferometer and a Mitutoyo Finescope microscope.

2.2.2 Diamond Turning/Milling Machine.

The work horse of this dissertation is the Moore Nanotechnology 350 Freeform Generator 5-axis diamond machining center with three linear axes (X-Y-Z) and two rotary axes (B-C) shown in Figure 2.1. The B-axis was not required for this research and was therefore not installed during these tests. The C-axis can either function as a turning axis with speeds ranging from zero to 10,000 rpm or as a servo-controlled rotary axis. An auxiliary 60,000 rpm milling/grinding spindle was also used in the experiments. It

was mounted directly to the Z-axis table with discrete angles relative to the C-axis. The Moore 350 FG has hydrostatic linear slides. Both the C-axis and the high speed milling spindles are supported by air bearing spindles produced by Professional Instruments (<http://www.airbearings.com/>). The milling spindle has an axial stiffness of $65 \text{ N}/\mu\text{m}$ and a radial stiffness of $20 \text{ N}/\mu\text{m}$ and axial and radial error motions less than 25 nm . The C-axis has axial and radial stiffnesses of $228 \text{ N}/\mu\text{m}$ and $98 \text{ N}/\mu\text{m}$ respectively with axial and radial error motions less than $12.5 \text{ N}/\mu\text{m}$.

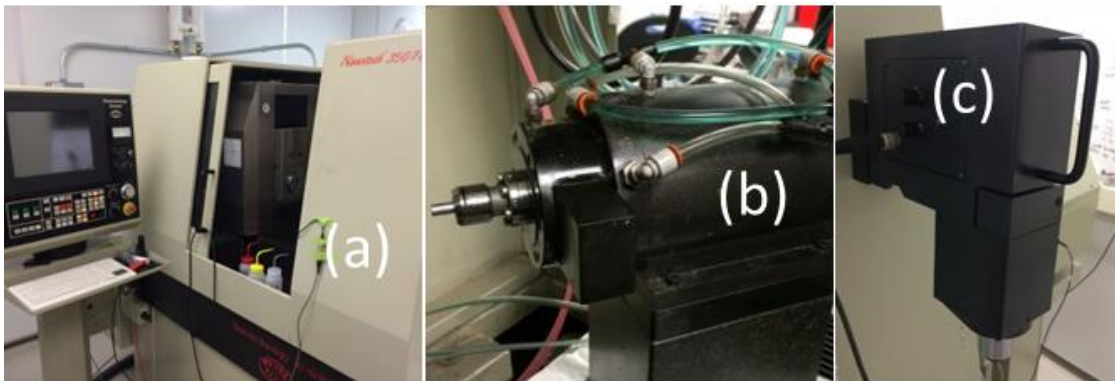


Figure 2.1: (a) Moore Nanotechnology 350 Freeform Generator 5-axis ultra-precision machine tool, (b) 60k rpm milling spindle, (c) tool setter microscope

2.2.3 Dynamometer

Kistler 9256C1 and 9256C2 (Figure 2.2) dynamometers were used in this work. These are designed for the measurement of small forces such as those that typically occur in diamond turning applications. The main difference between the two models is the size of the mounting area and bandwidth. The bandwidths for all axes on both dynamometer designs are in the range of $4.0\text{-}5.6 \text{ kHz}$. The smaller model has a higher bandwidth. The stiffness is greater than $250 \text{ N}/\mu\text{m}$ for the three orthogonal directions. The measurement range is $\pm 250 \text{ N}$ with a minimum threshold of 0.002 N .



Figure 2.2: Kistler mini-dynamometer 9256C1 (left) and the charge amplifier (right)

2.2.4 Cutting Fluids

Two cutting fluids were used in the diamond turning and milling work described here. For these experiments, unless otherwise noted, a food-grade mineral oil and a low odor (or “odorless”) mineral spirit was used. Typically, the mineral oil was used during the cutting operations and mineral spirits were used to help clean the part, however mineral spirits were also used in operations where chips adhered to the workpiece surface. Some cutting was done without fluid (dry) as will be described in the relevant sections.

2.2.5 Data Acquisition and Analysis

Data acquisition was performed with a National Instruments NI cDAQ-9174 DAQ board with an NI 9215 module and Labview 2010 Academic Version with a custom made virtual instrument (.vi) program (Figure 2.3). Typically, raw data was recorded at a sample rate greater than 2 times the mechanical bandwidth of the measurement equipment (for example a dynamometer and tool), and then a digital low-pass filter was applied to remove noise to allow depiction of the data more clearly. Unless otherwise stated, raw unfiltered data was used for analysis (e.g. calculation of average forces; error

bars, etc.). Data analysis was performed with MATLAB[®] 2013a. Relevant codes developed in this work are included in the Appendices.



Figure 2.3: NI DAQ board

2.2.6 Surface Metrology

Measurements of form, mid-spatial frequency error, and surface finish of the optical and test surfaces were made with various instruments. Form and mid-spatial error measurements were measured with a Zygo Verifire Fizeau interferometer at UNC Charlotte (Figure 2.4), and a OptiPro OptiTrace 5000 at OptiPro in Rochester, NY (Figure 2.5) [56]. Surface finish measurements were taken with a Zygo Newview 5000 scanning white light interferometer (Figure 2.4).



Figure 2.4: Zygo Verifire Fizeau interferometer (left), Zygo NewView 5000 (right)



Figure 2.5: OptiPro's OptiTrace 5000 with measurement stylus capabilities [56]

2.3 Experimental Setup

The three machining configurations were used to investigate material behavior and machining performance: orthogonal turning, face turning, ruling, and ball milling.

2.3.1 Orthogonal Turning

Orthogonal turning experiments allow greater understanding of material behavior and cutting mechanics in a simplified two-dimensional cutting operation as shown in Figure 2.6 and Figure 2.7. A dynamometer was mounted with the dynamometer axes aligned with the axes of the diamond turning machine. Turning tools were mounted directly on the dynamometer as shown in Figure 2.6. Orthogonal cutting was done on the outer diameter of a cylinder with pointed, deadsharp tools having a 60° included angle as shown in Figure 2.6. The tools had a 0° rake angle and a 7° clearance angle but could be rotated to produce a negative rake angle as will be described in later sections

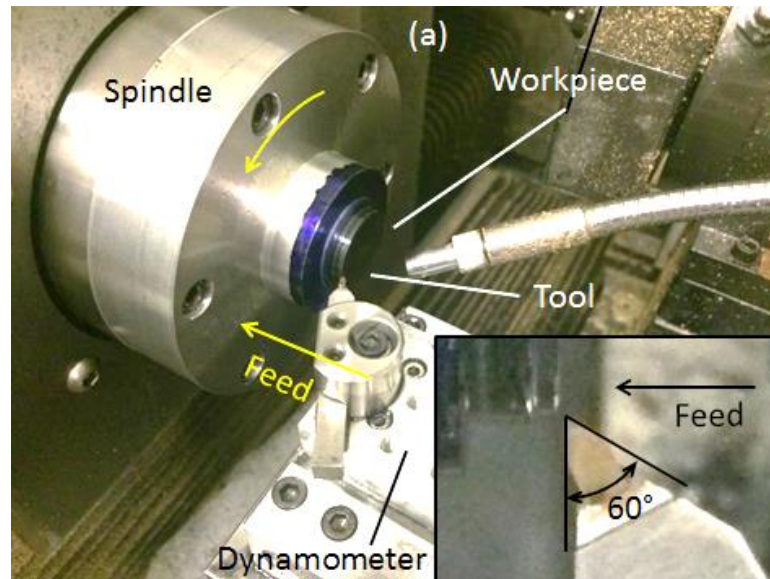


Figure 2.6: Orthogonal turning setup (shown here for IRG 26 cutting)

A simplified view of orthogonal cutting is shown in Figure 2.7. The cutting velocity is V_c . The cutting force F_c is parallel to the cutting velocity and the thrust force F_t is perpendicular to this direction. By dividing by the uncut chip area, cutting force coefficients can be obtained. The force system F_c and F_t forms a force vector \mathbf{R} with a resultant direction relative to the uncut surface θ . The force components can also be transformed into normal and friction forces on the tool rake face N and F . If the cutting is localized to a ductile deformation on a well-defined shear plane, and the shear angle is known, they can also be transformed to obtain a shear force F_s and normal force F_N on the shear plane. Cutting force coefficients K_c and K_t are obtained by dividing by the uncut chip area t_c , where w is the chip width. These force systems will be used in the data analysis to be presented in later chapters.

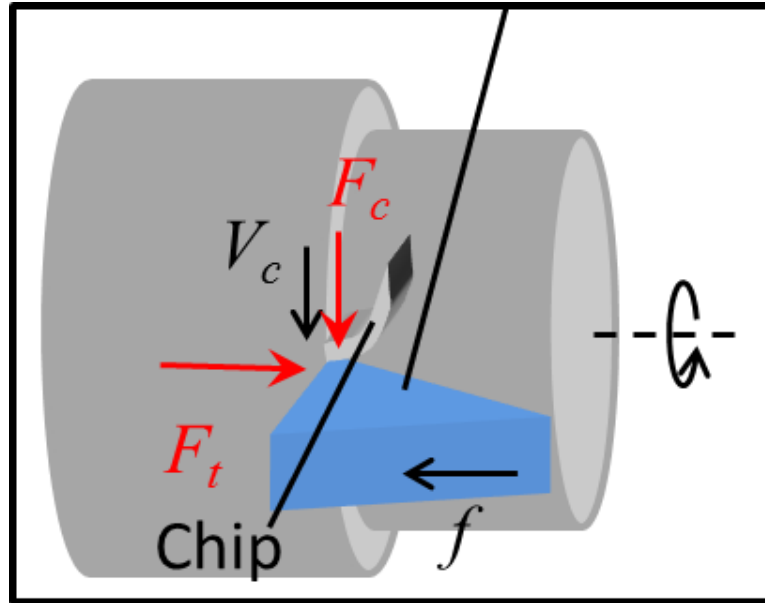


Figure 2.7: Schematic cross section of an orthogonal cutting operation

2.3.2 Face Turning

Face turning, or facing, is the cutting operation typically used to diamond turn optics. Much of the development of and research on so-called ductile regime machining has been done in face turning with round nose tools. Figure 2.8 shows a top view of the geometric characteristics of a facing operation with a round nose tool. The most relevant parameters are: tool nose radius (TNR), spindle speed, feed per revolution (fpr), feed rate, and depth of cut. The surface finish of a faced part is dependent on the TNR and the fpr, the chip thickness is dependent on the TNR, fpr, and the depth of cut, and the behavior of a brittle material in a facing operation is dependent on all of these parameters. This behavior determines whether the machined surface will have acceptable levels of surface and subsurface damage and/or brittle fracture.

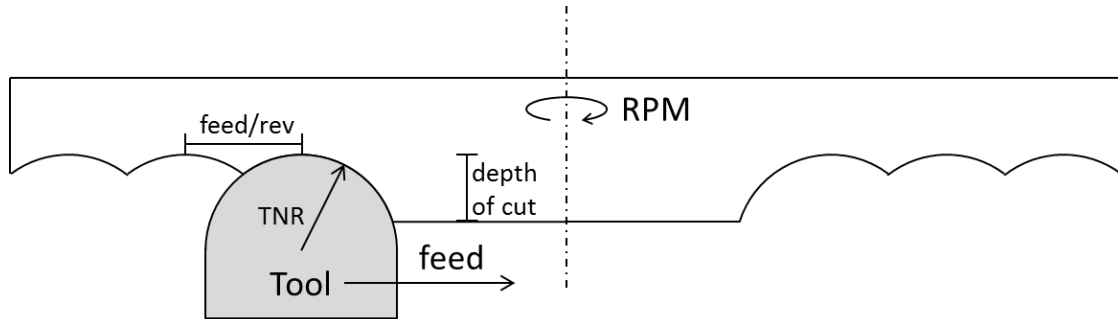


Figure 2.8: Face turning schematic

2.3.3 Ruling

Ruling uses a planing-like geometry to make linear non-overlapping and/or overlapping structures. As in turning the tool is stationary and the part is moving. Unlike turning the cuts typically do not overlap. The part can either be rotating or moving in a straight line and the cutting velocity may thus be generated by the machine spindle or the machine slide drive motors. The tool is plunged into the material while the material is moving. The tool can either be plunged straight in and back out or held at some depth for a time before being pulled out of the cut. The geometric character of the ruling motions used in these investigations is demonstrated in Figure 2.9. In Figure 2.9 (a) a round nosed tool is moved along a line and ramped in and out of the material. In Figure 2.9 (b) a round nosed is ramped in and out of a rotating part. In Figure 2.9 (c) a pointed tool is moved along a linear path and ramped into the part, held at a certain depth and then ramped out of the part. These operations have different utility for research. The configuration of Figure 2.9 (a) allows the measurement of forces and the appearance of surface damage as a function of depth. The configuration of Figure 2.9 (b) allows for similar measurements, but also involves a constantly changing orientation of the tool cutting direction relative to the part; this is useful for examining the effect of crystal orientation as occur for example in the machining of single crystal germanium. The

configuration of Figure 2.9 (c) typically generates forces that are too small to resolve with the dynamometers used in this work, but does allow for the generation of structures that can affect the optical behavior of the machined surface (e.g. gratings).

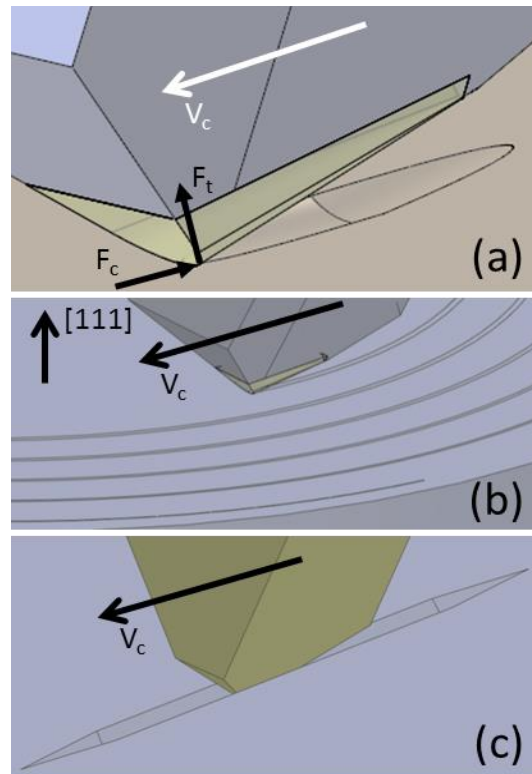


Figure 2.9: Ruling Configurations: (a) ramp in ramp out, (b) spiral, and (c) straight grooves

2.3.4 Ball End-Milling

All of the milling tests performed used a diamond ball end mill as the cutting tool. The type of milling is referred to as “raster” milling to describe the scan-like pattern that defines the path of the machine when generating an optical surface. The layout and parameters for raster milling can be seen in Figure 2.10.

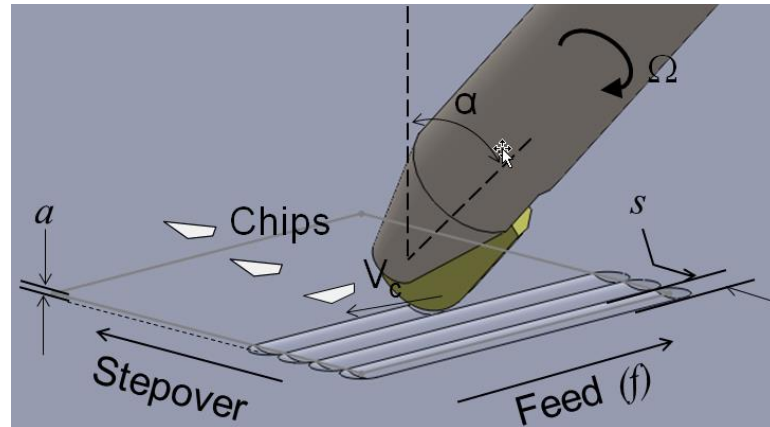


Figure 2.10: Raster milling with a ball end mill

There are two different ways to raster mill: uni-directional or bi-direction. Uni-directional milling means that when you are cutting the tool is moving in the same direction; when the end of the part is reached the tool is lifted away from the part and repositioned at the opposite end of the part. Bi-directional milling means that when the tool reaches the end of the part a sideways move is made and the tool continues back in the opposite direction. Refer to Figure 2.11 for a sketch of uni- and bi-directional raster milling.

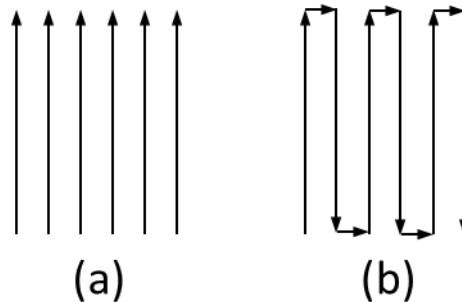


Figure 2.11: Uni-directional (a) and bi-directional (b) raster milling tool path pattern

CHAPTER 3: DIAMOND MACHINING OF CHALCOGENIDE GLASS

3.1 Introduction

In this chapter, turning and milling results in an arsenic-selenium, infrared, chalcogenide glass ($\text{As}_{40}\text{Se}_{60}$ or “IRG 26”) are discussed. Because of its relatively high index (2.8) and high transmittance (>60%) over wavelengths ranging from 0.85 μm to 12 μm , this material is particularly suited to IR imaging. The density, thermal conductivity and specific heat capacity are 4630 kg/m^3 , 0.24 W/m-K , and 360 J/kg-K , respectively. The material has a fracture toughness of $0.285 \text{ MPa-m}^{1/2}$, a Knoop hardness of 1.04 GPa, and a Young’s modulus of 18.3 GPa. The glass transition temperature, T_g , is relatively low, 185°C , making mass production by molding feasible. However while the material has brittle behavior (see Chapter 1), this chapter demonstrates that it can be successfully machined, and conditions for producing a fracture free surface are identified here.

To understand the cutting mechanics, forces are measured for orthogonal turning and face turning. Conditions under which the material deformation becomes fracture dominated are identified and correlated to the machined surfaces. Orthogonal cutting data is combined with a mechanistic model to estimate the forces in high-speed, single crystal diamond, ball milling of the material. Milling tests are completed to identify the effect of machining parameters on surface finish. Milling is then applied to the manufacture of a freeform surface incorporating an aspheric thermal landscape imaging lens and kinematic alignment features (lens specifications: F/1.18, 30 mm effective focal

length, 30° field of view). While diamond turned chalcogenide glass lenses have been reported [25], this work shows that freeform milling is a viable path for prototyping and small volume production of IR-optics in $As_{40}Se_{60}$.

3.2 Experimental Summary

Three different cutting operations were used through-out testing: (1) orthogonal turning, (2) face turning, and (3) ball end-milling. The work piece was held by a vacuum chuck with or without additional adhesives applied after the vacuum was turned on. Turning tools were mounted to the MiniDyn for in-process force measurements, using the NI DAQ board and LabVIEW with a sampling rate of 25kHz. The details of these experimental arrangements are described in Chapter 2.

3.3 Orthogonal Cutting

Turning tools were mounted directly on a Kistler 9256C1 dynamometer as shown in Figure 2.6. Orthogonal cutting was done on the outer diameter of a 14 mm diameter cylinder with a pointed, deadsharp tool having a 60° included angle as shown in Figure 2.6. The tool had a 0° rake angle and a 7° clearance angle, and the chip width was 200 μm .

3.3.1 Force Versus Chip Thickness With Constant Speed

The uncut chip thickness was varied from 0.1 μm to 8 μm and the cutting speeds were varied from 0.5 m/s to 8 m/s. In this material a negative rake angle was not required to obtain fracture free surfaces. For each parameter set, 80 revolutions of data were recorded, trimmed to avoid lead in and lead out effects, and mean values were calculated. The procedure was repeated three times for each parameter set.

Figure 3.1 shows the average F_c and F_t as a function of t_c for orthogonal cutting. For the lowest value of t_c (0.1 μm) F_t was greater than F_c , consistent with the edge effects described in other work [8]. After an initial increase, a rapid decrease in F_c and F_t is seen at t_c equal to 1 μm . Then, further increases in forces at reduced slope were seen as t_c was increased up to 8 μm . For t_c less than 1 μm , the chips appear to be the result of predominately ductile deformation (inset for t_c equal to 0.2 μm). As t_c was increased beyond 1 μm , the chips appear more fragmented (inset for t_c equal to 2 μm). The percent deviations in mean force values reached a maximum at t_c equal to 1 μm ($\pm 35\%$), but was generally less than $\pm 10\%$.

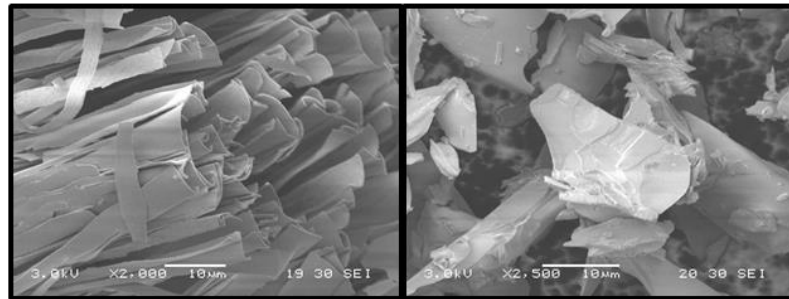
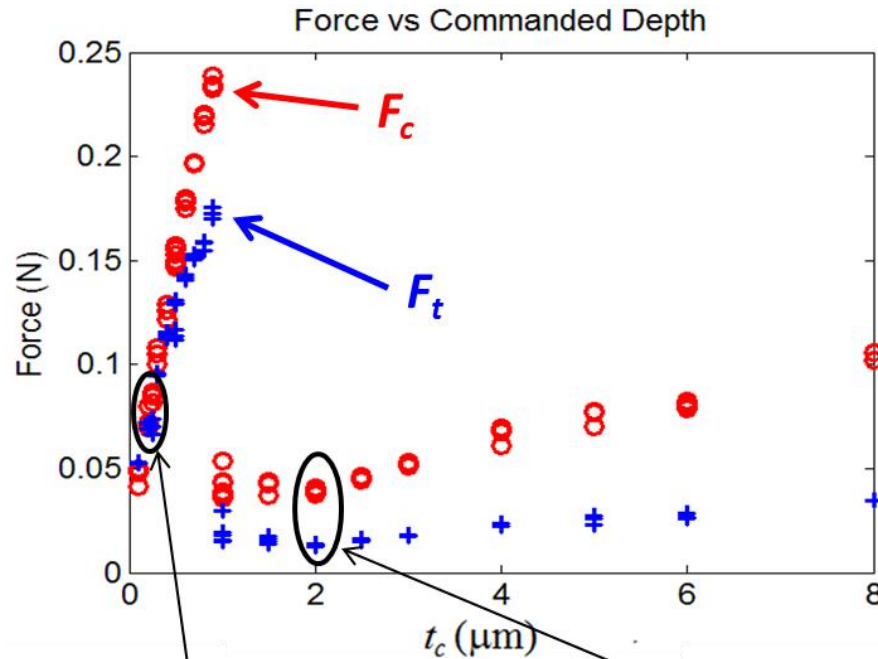


Figure 3.1: Cutting force data at a constant cutting speed (4 m/s) with corresponding SEM images of ductile and brittle chips and specific cutting parameters

Cutting force coefficients, K_c and K_t , are shown in Figure 3.2. For t_c below 1 μm , K_c decreases continuously from approximately 2.5 kN/mm^2 to 1.25 kN/mm^2 , and K_t decreases from approximately 2.6 kN/mm^2 to 1.0 kN/mm^2 . When t_c exceeds 1 μm , a sharp decrease in K_c and K_t to less than 0.25 kN/mm^2 is seen. K_c and K_t then decreased gradually with further increase in t_c .

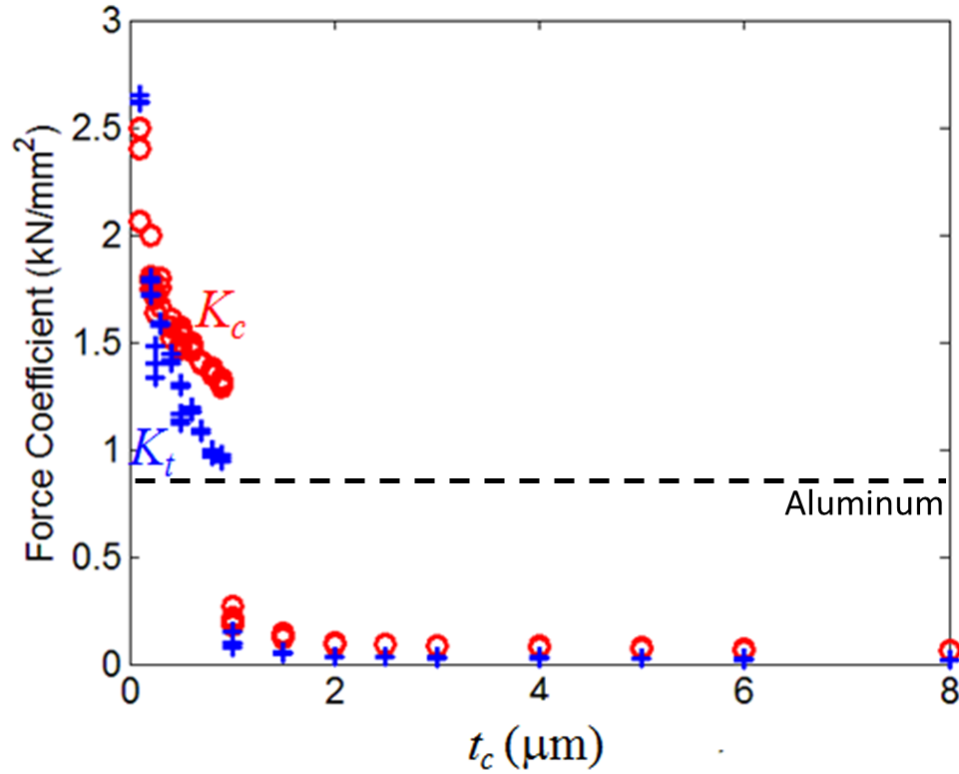


Figure 3.2: Force coefficients with a constant cutting speed of 4 m/s

Figure 3.3 shows the resultant cutting force direction as a function of uncut chip thickness. The angle between \mathbf{R} and the surface is given by equation Eq 3.1.

$$\mathbf{R} = \tan^{-1}\left(\frac{F_t}{F_c}\right) \quad \text{Eq 3.1}$$

As described by Lucca et al. [14], the development of a surface with greater brittle fracture is accompanied by a rotation of the resultant force vector toward the machined surface (decreasing θ). Lucca et al. [14] surmise that the rotation of the force vector generates a tensile region behind the tool and this results in fractures forming on the surface behind the tool.

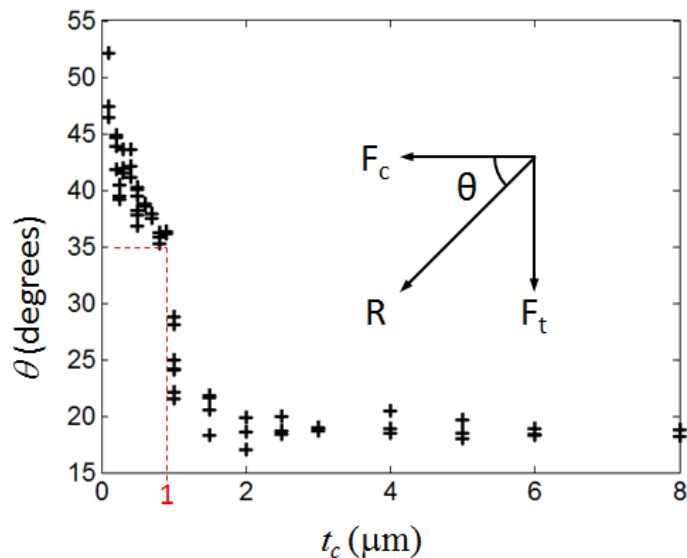


Figure 3.3: Resultant force vector direction as a function of uncut chip thickness was calculated from the cutting forces, using the geometry defined in Figure 2.7.

3.3.2 Force Versus Speed With Constant Chip Thickness

Despite the relatively low T_g of this material (185 °C) and potential thermal softening, little change in F_c and F_t as a function of cutting speed (up to 8 m/s) as shown in (see Figure 3.4).

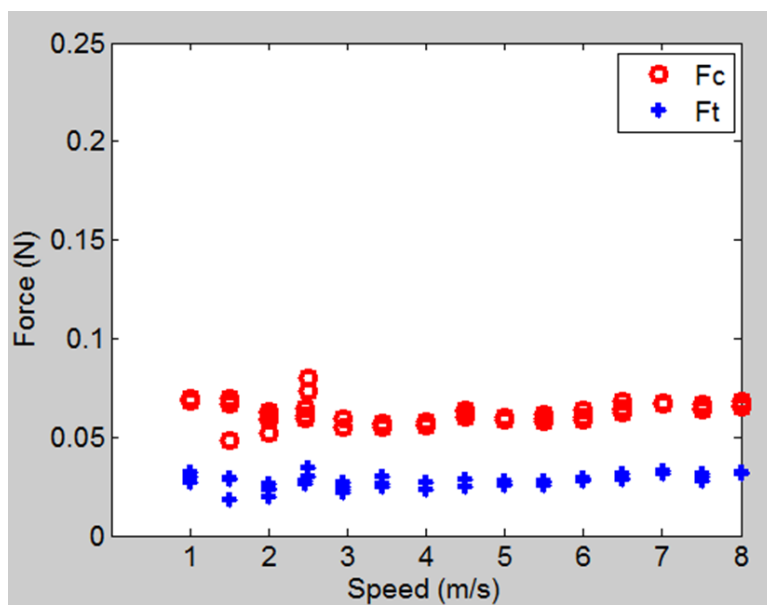


Figure 3.4: Force versus speed with a constant chip width (0.200 mm) and chip thickness (0.002 mm) (shown with same vertical scale as Figure 3.1 for comparison)

Figure 3.4 An anomalous behavior was found for one test completed at a cutting speed of 0.5 m/s. Three cutting tests were performed at 0.5 m/s immediately after the surface was prepared with many shallow “ductile” cuts to remove any sign on brittle fracture, i.e. the force would have reached a steady state at a known ductile fpr. For these three cutting tests the average values of F_c and F_t were found to be 0.49 N and 0.43 N respectively, almost ten times greater than the corresponding forces at a cutting speed of 1 m/s, This anomalous cutting behavior was found after the entire battery of cutting tests was complete.

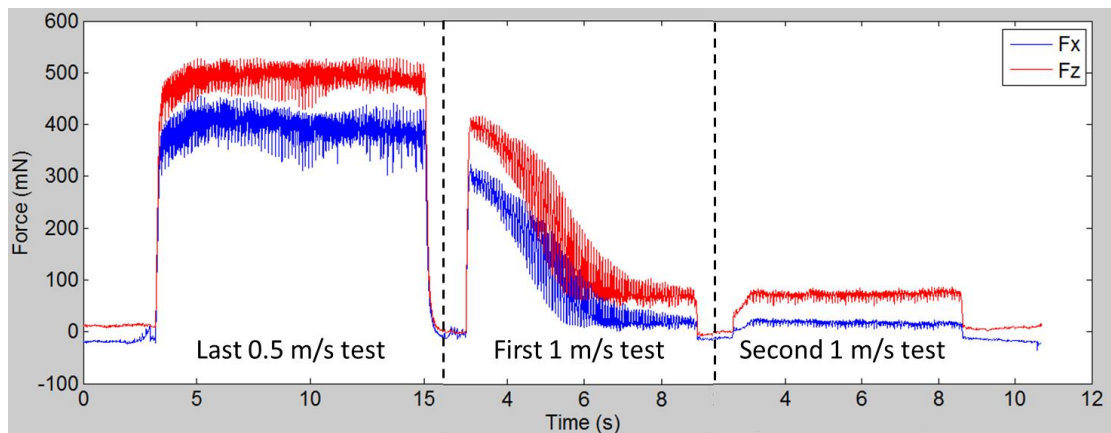


Figure 3.5: The transition from the 0.5 m/s tests to the 1 m/s tests (filtered with a 60 Hz low-pass)

To investigate the behavior more thoroughly, the force signal traces, 80 revolutions in time duration, for the last cut completed at 0.5 m/s and the first two cuts completed at 1 m/s were compared. Figure 3.5 shows the results. The last test at a cutting speed of 0.5 m/s shows the high force levels. The first test at 1 m/s begins at a high force level, but is seen to decrease to the lower force levels seen in Figure 3.5, however this drop requires more than half of the test duration – more than 40 revolutions of cutting – to occur. The next test at the cutting speed of 1 m/s then remains at the lower force level from beginning to end. Thus, it appears that there is a change in the cutting

mechanics occurring over a relatively long cutting distance. This suggests a hypothesis that depending on the cutting parameters relatively more or less damage is propagated into the surface to be cut again on the next revolution. Under some conditions, the damage build-up is rapid enough that it continues to be propagated into the surface until it causes a change from ductile-dominated to brittle-fracture-dominated cutting mechanics. In future work a new experimental arrangement will be devised to: (1) investigate even lower cutting speeds and (2) make an orthogonal cut over a surface not damaged by a previous pass, for example as might be done by a facing pass with a slightly tilted dead sharp tool. At this point it is not clear whether there is a speed effect in this material. It is possible that for very low cutting speeds less than 1 m/s, steady-state forces will be maintained and will drop very rapidly with cutting speed becoming essentially constant as shown in Figure 3.4. However based on the transient force data it remains unclear whether the steady-state forces do in fact remain at steady-state for very low cutting speeds. If there is a speed effect it may be a strain rate dependency that causes a transition from a ductile-dominated to a brittle-dominated deformation mechanism. Clearly this is a topic for future investigation as discussed in Chapter 7.

3.3.3 Hysteresis

The observation made in the last section was that potentially a build-up of damage within a surface may lead to changes in cutting mechanics. This suggested that the character of the change in cutting forces showing in Figure 3.1 might be different for increasing rather than decreasing chip thickness. The experiments summarized by Figure 3.2 were repeated with decreasing rather than increasing feed/rev. If the damage build-up in the surface caused a change in the cutting mechanics it was hypothesized that the

transition back to the higher force levels would occur at a different critical depth of cut depending on the character of the surface being cut. Said another way, it was hypothesized that the change in cutting mechanics might exhibit a hysteretic behavior. Experiments were conducted as follows. We started with a smaller chip thickness and increased the chip thickness in increments of $0.1 \mu\text{m}$ until the transition at 1 micrometer was observed. Then once the brittle cutting was at a steady state, we then decreased the chip thickness in increments of $0.1 \mu\text{m}$ back through the transition. The average cutting forces clearly show hysteresis depending on the previous cutting parameters/surface quality. This is demonstrated in Figure 3.6 and detailed in Figure 3.7. When the chip thickness is increased, the transition in the cutting mechanics occurs between $0.9 \mu\text{m}$ and $1 \mu\text{m}$, consistent with the results shown in Figure 3.2. However, when the chip thickness is decreased, the transition back to the higher force levels occurs between $0.8 \mu\text{m}$ and $0.7 \mu\text{m}$. The cutting force coefficients also show hysteretic behavior as shown in Figure 3.8.

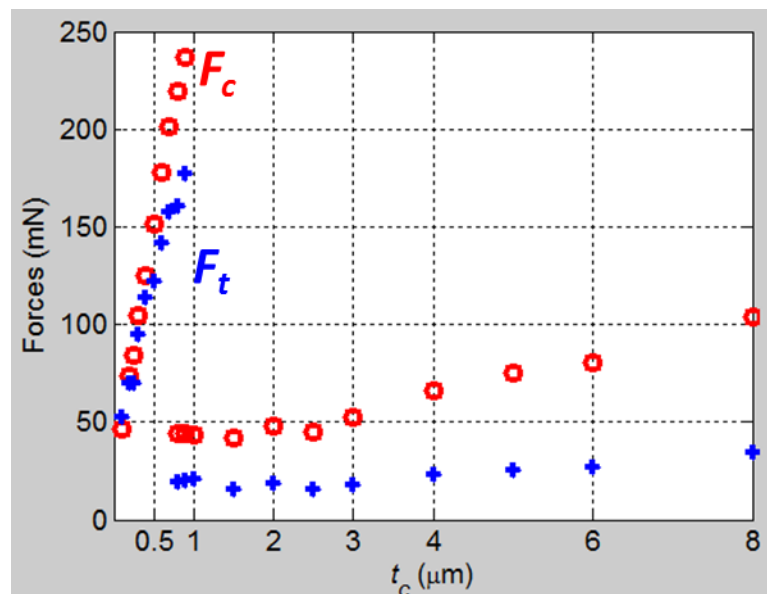


Figure 3.6: Force averages showing hysteresis in the cutting mechanism due to different prior surface qualities

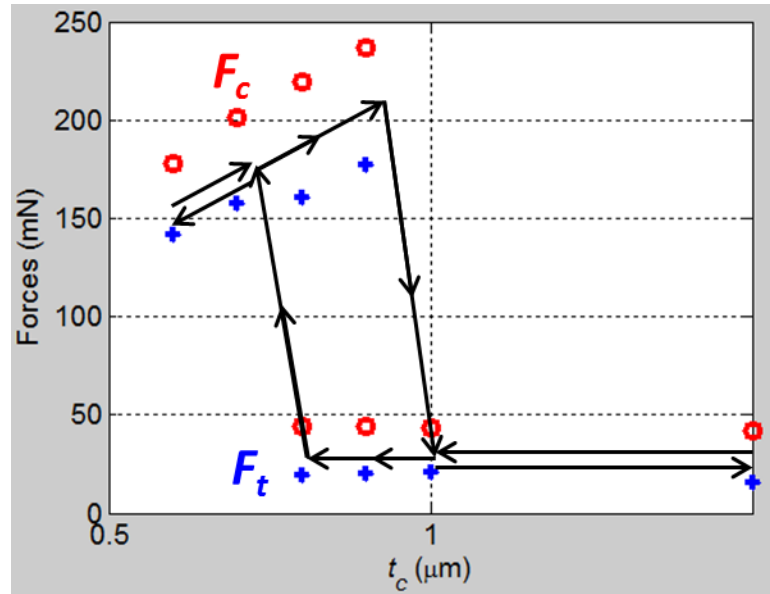


Figure 3.7: Enlarged view of the hysteresis in the cutting forces shown in Figure 3.6

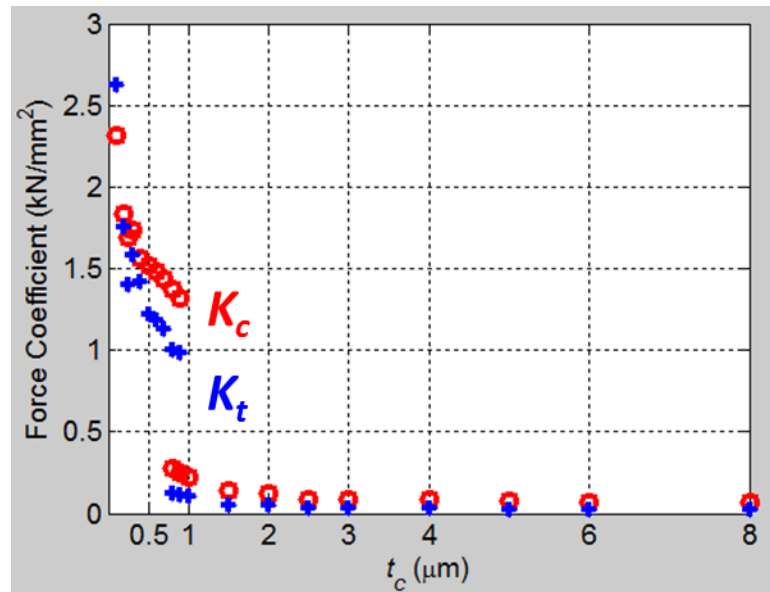


Figure 3.8: Force coefficients for the forces shown in Figure 3.6 for the hysteric behavior of the cutting mechanism

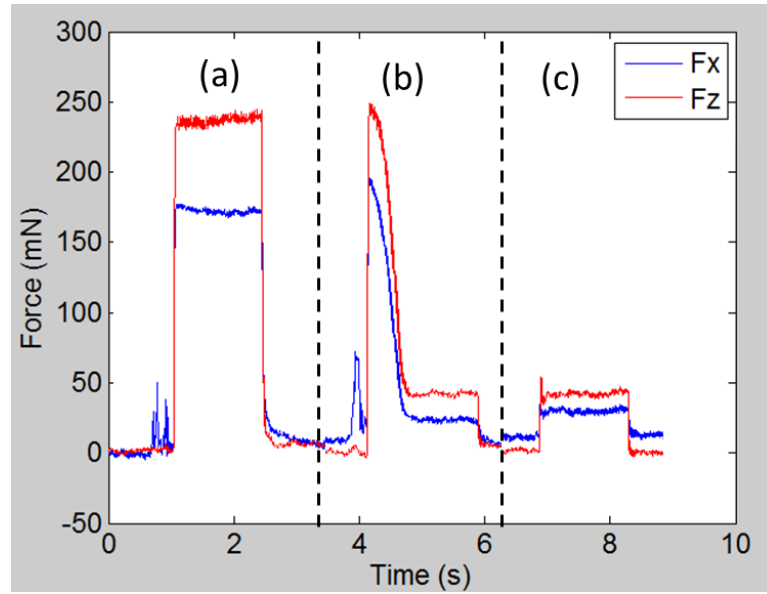


Figure 3.9: Transition from 0.9 $\mu\text{m}/\text{rev}$ to 1.0 $\mu\text{m}/\text{rev}$. (a) steady-state reached for 0.9 $\mu\text{m}/\text{rev}$, (b) 1.0 $\mu\text{m}/\text{rev}$ immediately after (a), (c) steady-state reached for 1.0 $\mu\text{m}/\text{rev}$

Putting together force traces 80 revolutions in length further illustrates the character in the transition region. Figure 3.9 shows a steady high force or ductile-dominated cutting mechanism stabilized at an uncut chip thickness of 0.9 micrometer. The next trace shows the force levels at an uncut chip thickness of 1 micrometer with the forces beginning at the higher levels and then decreasing over approximately 30 revolutions to the lower level. A subsequent cutting test again at 1 micrometer uncut chip thickness then shows that the lower force level is maintained. This behavior is further detailed in Figure 3.10; showing that in order to achieve a ductile-dominated cut after the previous cut was brittle-fracture dominated, an uncut chip thickness of 0.7 μm was needed. It took less than 80 revolutions to remove and not continue to propagate the brittle fracture when an uncut chip thickness of 0.7 μm was used. The cutting mechanism then remained at a steady-state for subsequent cuts at uncut chip thicknesses of 0.7 μm and 0.8 μm . When the uncut chip thickness was returned to 0.9 μm , the transition back

to the lower force level required four full cutting tests (320 revolutions), reaching steady-state brittle-fracture dominated cutting in the fifth test.

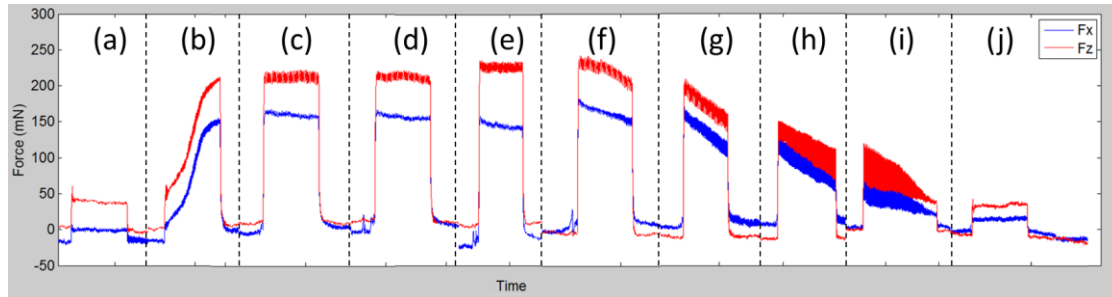


Figure 3.10: Brittle-Ductile-Brittle transition through multiple sequential tests. (a) brittle at $0.8 \mu\text{m}/\text{rev}$, (b) transition to ductile at $0.7 \mu\text{m}/\text{rev}$, (c & d) steady-state ductile at $0.7 \mu\text{m}/\text{s}$, (e) steady-state ductile at $0.8 \mu\text{m}/\text{s}$, (f, g, h, and i) transition back to brittle at $0.9 \mu\text{m}/\text{s}$, (j) steady-state brittle at $0.9 \mu\text{m}/\text{s}$

3.4 Face Turning

To correlate cutting mechanics with surface characteristics, forces were also measured in face turning with a single crystal diamond tool having a nose radius of 0.5 mm , a 0° rake angle, and a 7° clearance angle. The feed per revolution (fpr) or chip thickness (t_c) was varied from $0.25 \mu\text{m}$ to $10 \mu\text{m}$ while the depth of cut and cutting speeds were held constant at $25 \mu\text{m}$ and 4 m/s respectively. Measured forces as a function of fpr are shown in Figure 3.11. After an initial sharp increase, the turning forces begin to decrease at an fpr greater than $2 \mu\text{m}$.

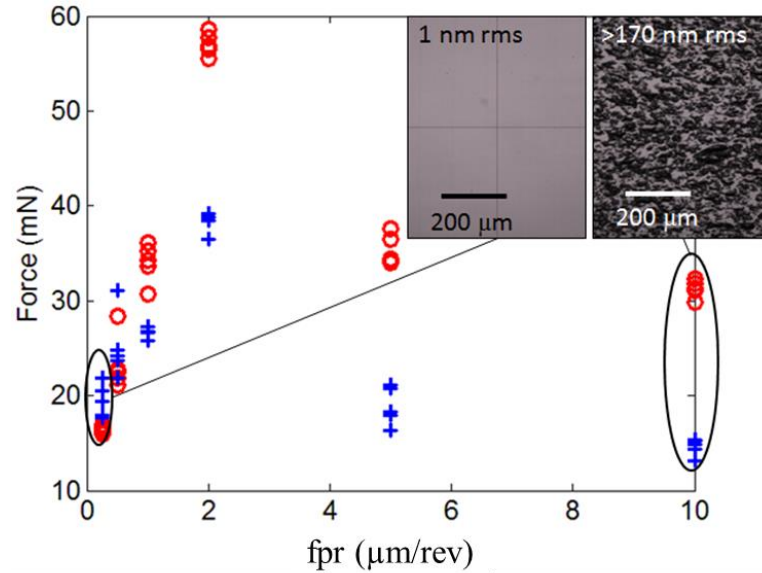


Figure 3.11: Round nose face turning force versus feed per revolution

A mechanistic force prediction model was used to help understand the drop in force after an fpr of 2 μm . Chip thicknesses were calculated along the tool edge for each fpr tested. Using the cutting force coefficients from the orthogonal cutting, we were able to correlate the drop of force in the facing between 2 μm and 5 μm fpr to the drop of force coefficients between 0.9 μm and 1.0 μm uncut chip thickness in the orthogonal turning. The chip thickness variation around the tool nose is illustrated in Figure 3.12.

Figure 3.13 shows the maximum calculated chip thickness and the average chip thickness along the cutting edge for different feed per revolutions with a constant depth of cut of 25 μm to match the facing experiments. These values were determined numerically using a simulated tool shape. At 2 μm fpr, all the chip thicknesses are less than 1 μm , but at 5 μm some of the chip thickness is greater than 1 μm . By 10 μm fpr, the average chip thickness is more than 1.5 μm .

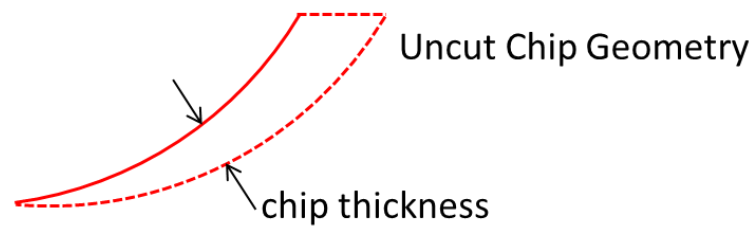
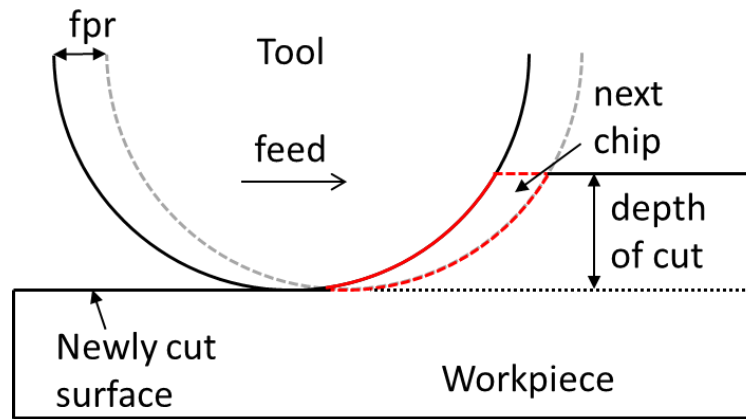


Figure 3.12: Face turning chip geometry

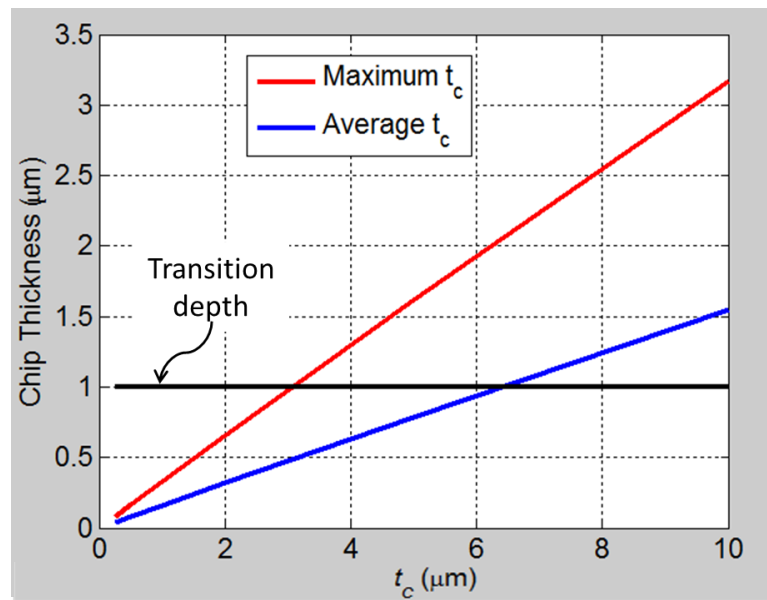


Figure 3.13: Predicted chip thicknesses at different feed to understand when to expect a drop in cutting forces, see chip thickness geometry in Figure 3.12

To estimate the cutting forces, the differential forces on each differential chip area element were integrated as shown in Figure 3.14. A look up table was used to find the cutting force coefficient on each differential area element. The force as a function of f_{pr} is shown in Figure 3.15. The qualitative character of the calculated and measured turning forces is similar. However, comparing the measured data in Figure 3.11 to the simulated forces in Figure 3.15, we note that there is a drop in measured forces after $2 \mu\text{m}/\text{rev}$ whereas the simulated forces do not both drop until after $5 \mu\text{m}/\text{rev}$.

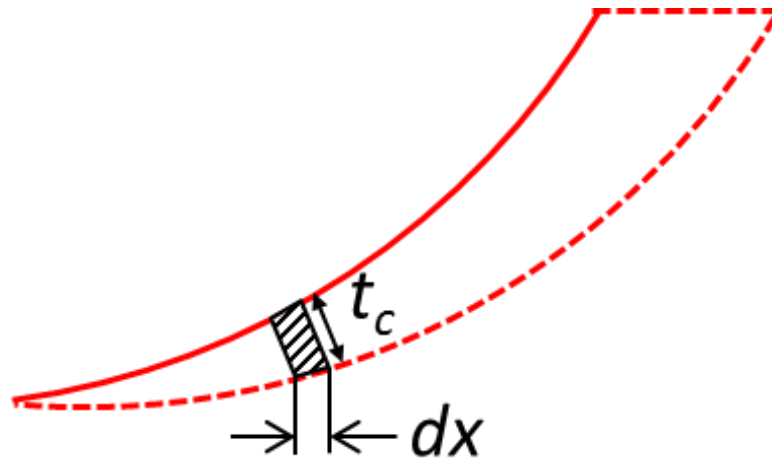


Figure 3.14: Integral to determine the cutting force on a round nosed tool.

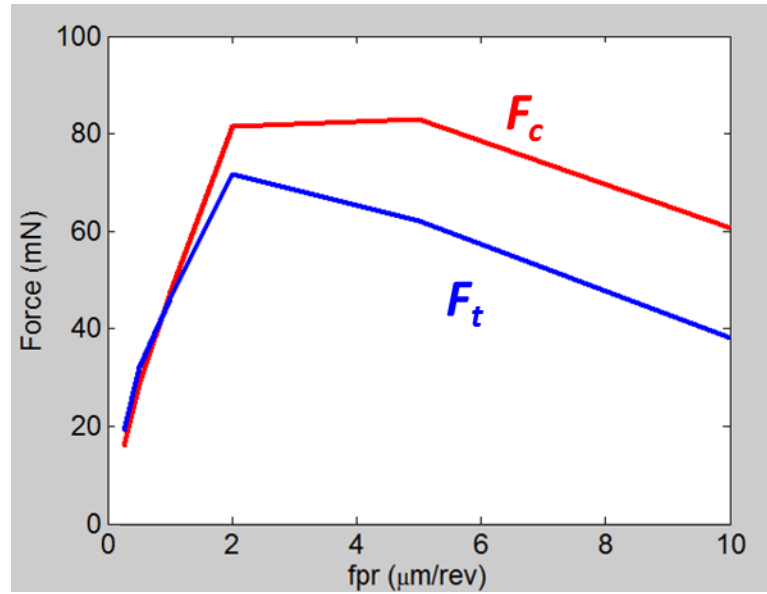


Figure 3.15: Predicted face turning forces using force coefficients shown in Figure 3.2

It was hypothesized that the discrepancy was the result of the hysteretic behavior. In other words, in the region between $0.7 \mu\text{m}$ chip thickness and $0.9 \mu\text{m}$ chip thickness, there are two possible values for the cutting force coefficients. To generate Figure 3.15 the higher ones were used. Using the lower ones where fracture already exists in the surface and is allowed to propagate produces the results shown in Figure 3.16. The assumption is reasonable because in round nose facing. If fracture was created higher up along the tool it seems likely that the fracture would continue to propagate down the tool until it reached a chip thickness that will not propagate fracture.

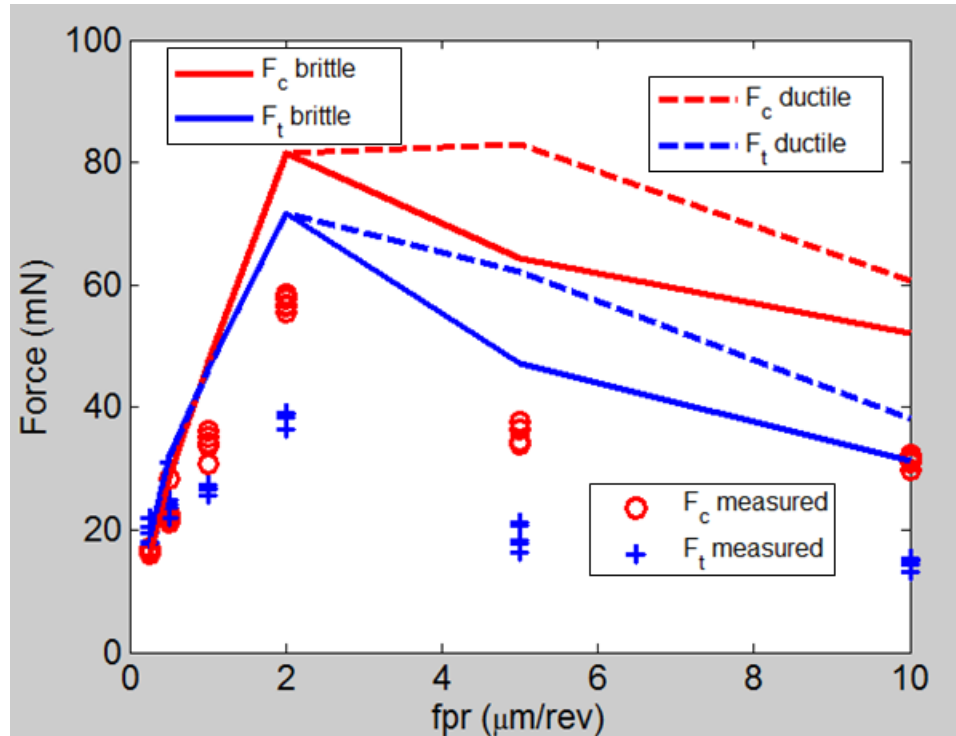


Figure 3.16: Comparison between measured facing data and simulated facing data using both directions of the hysteric behavior of the cutting forces

More understanding is needed in the various effects of the ductile-brittle transition to better predict the turning forces from orthogonal data; the trend follows the measured data but the magnitude does not match.

3.5 Ball End-Milling

Since the end goal of the work is to cut complex optics, including freeform surfaces, milling was also evaluated. Milling performance was evaluated by raster milling 2 mm square patches. Each patch was examined with optical microscopy and SWLI. The milling spindle inclination was found to have an insignificant effect of surface finish. Surface fracture was observed only for the most aggressive parameters (60 μm stepover, 10 $\mu\text{m}/\text{rev}$ feed). The measured finish was compared with ideal surfaces generated using MATLAB[®]. Figure 3.17 shows that the finish is a strong function of stepover and is less sensitive to feed rate over the range of variables examined. The

relationship between surface finish and feed/rev and stepover is similar to the “square root of the sum of the squares” of the feed/rev and stepover. In other words, the theoretical surface finish is mostly affected by the highest value between the feed/rev and stepover.

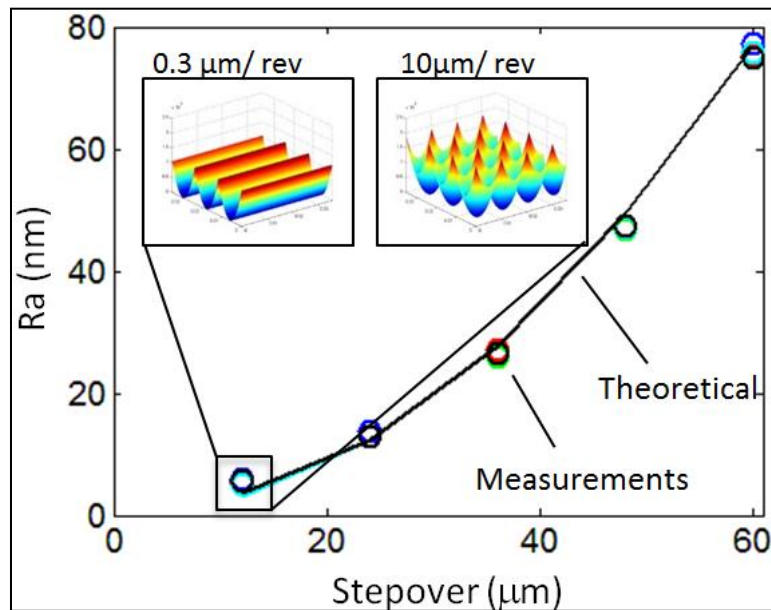


Figure 3.17: Measured and theoretical surface finished of milled test patches

For example, the surfaces shown in the insets for 0.3 $\mu\text{m}/\text{rev}$ and 10 $\mu\text{m}/\text{rev}$ at 12 μm stepover produce nearly the same surface finish. Surface finishes as low as 5 nm Ra were obtained.

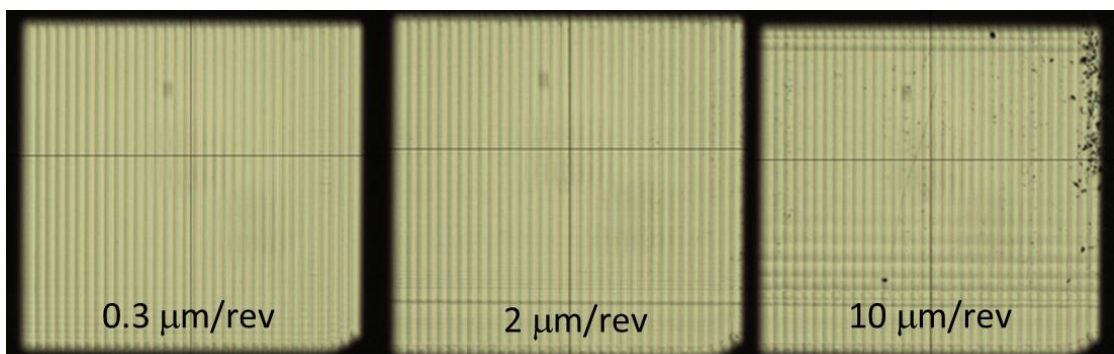


Figure 3.18: Milling patch testing showing a stepover of 60 μm and three feeds: 0.3 $\mu\text{m}/\text{rev}$, 2 $\mu\text{m}/\text{rev}$, and 10 $\mu\text{m}/\text{rev}$

To evaluate milling performance a large grid of machining parameters was tested. With a constant depth of 100 μm , five stepovers of 12, 24, 36, 48, and 60 μm , and five fprs of 0.3, 1, 2, 5, 10 $\mu\text{m}/\text{rev}$ were used to create a grid of 25 tests. Figure 3.18 shows three different feed rates for the same stepover. Only the highest feed rate of 10 $\mu\text{m}/\text{rev}$ showed signs of surface fracture. The fracture occurred during the first passes where the tool was plunged into the material and therefore the maximum uncut chip thickness was greater. Of the other parameters tested, only the 10 $\mu\text{m}/\text{rev}$ feed rate showed fracture with the most fracture occurring at the initiation of cutting, which is full slot cutting. The surface showed minor defects, but not nearly as severe as the lead-in fracture. It was observed that the width of fractured surface was independent of stepover as shown in Figure 3.19. This seems to imply that nearly all the fracture occurred in the first slot cut.

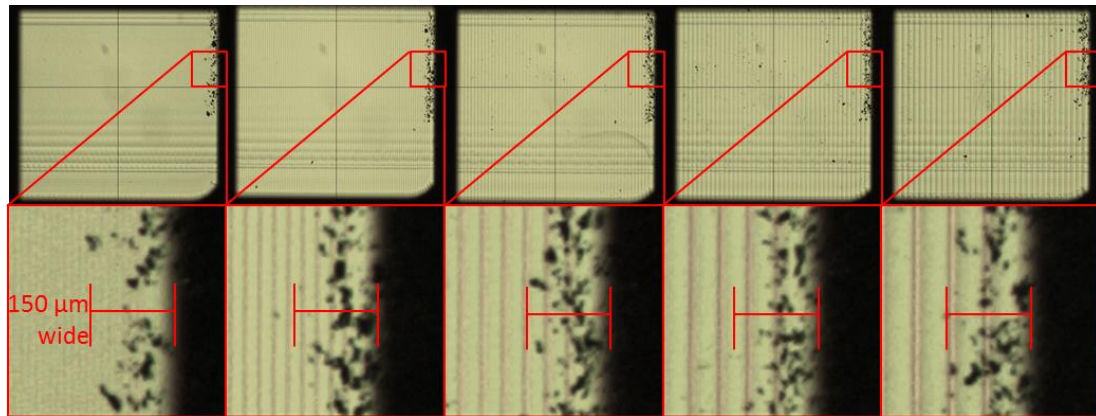


Figure 3.19: All five stepovers performed at 10 $\mu\text{m}/\text{rev}$ (left to right: 12 μm , 24 μm , 36 μm , 48 μm , and 60 μm stepover) show the same width damaged region.

As shown in Figure 3.17, the surface finish followed the theoretically predicted value for ball milling. A typical scanning white light interferometer measurement of one of the test patches is shown in Figure 3.20. Because the fpr is low (2 μm) compared to the stepover of 24 μm a cusp structure with a spatial period of 24 μm dominates the surface finish.

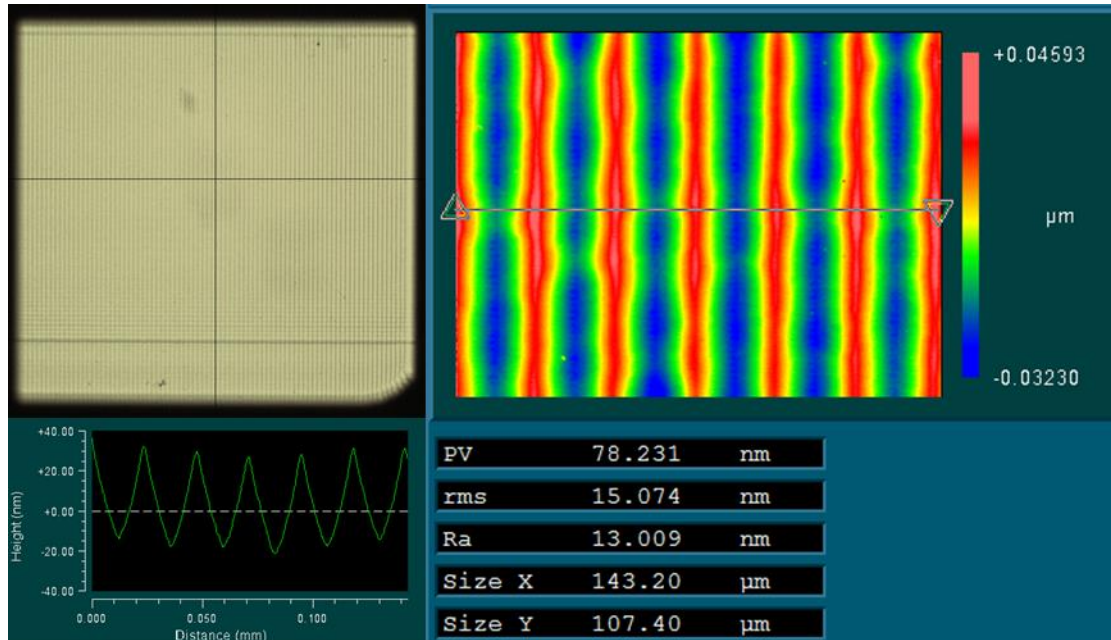


Figure 3.20: Milling test patch with parameters stepover, feed/rev, and spindle speed of $24\ \mu\text{m}$, $2\ \mu\text{m}$, and 45,000 RPM respectively

A qualitative comparison of the cutting parameters $10\ \mu\text{m}/\text{rev}$ fpr and $60\ \mu\text{m}$ stepover between three different tool and machine configurations can be seen in Figure 3.21. The three configurations are -25° rake and 45° inclination, 0° rake and 0° inclination, and 0° rake and 22.5° inclination. The first path fracture is greatest with zero rake and inclination and the least in the highest rake and inclination imply the fracture is reduced with a negative rake and/or inclining the milling spindle. Since the -25° rake left small areas of re-adhered chips (shown in Figure 3.22), the best milling conditions were with the 0° rake tool away from the center of rotation.

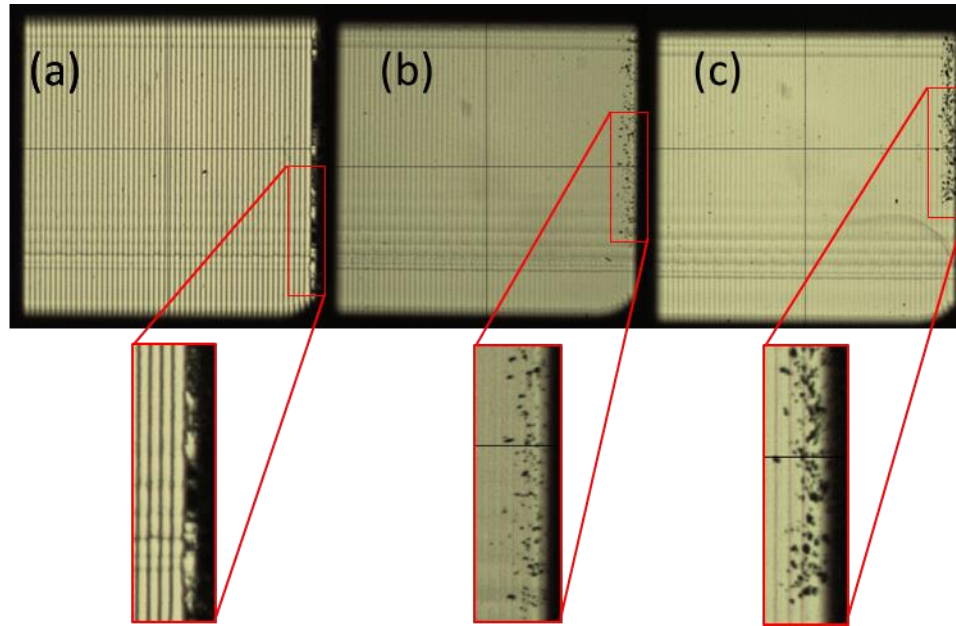


Figure 3.21: Milling patch tests showing the same cutting parameters (10 $\mu\text{m}/\text{rev}$ feed/rev and 60 μm stepover) but with three different tool geometry variations: (a) -25° rake and 45° mill inclination, (b) 0° rake and 22.5° mill inclination, and (c) 0° rake and 0° mill inclination

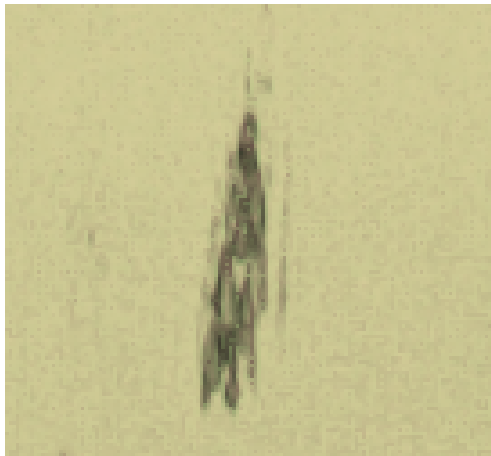


Figure 3.22: Example of a re-adhered chip from a patch test using a -25° rake milling tool

CHAPTER 4: DIAMOND MACHINING OF GERMANIUM

4.1 Introduction

For many years, optical design has been limited to rotationally symmetric refractive optics and planar diffractive optics. Ultra-precision diamond machining has the ability to open up the optical design space to include optics with freeform and structured surfaces that can perform multiple refractive and diffractive functions simultaneously. Examples of this type of multiple scale optics can be found in nature. A moth's eye (Figure 4.1 [57] [58] [59]) has a large base sphere on the millimeter scale, micro-optics on the scale of tens of micrometers, and sub-micrometer (sub-wavelength) structures that act as an anti-reflective coating. For other biological eyes such as the mantis shrimp, the structured surfaces have other more complex functions such as polarization sensitivity.

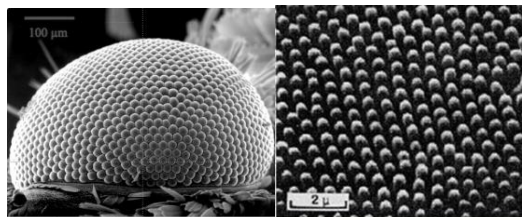


Figure 4.1: (Left) Compound moth eye [57]. (Right) Scanning electron microscope image of fine detail on surface of moth's eye showing anti-reflective sub-wavelength surface structures [58] [59]

Ultra-precision machining is particularly applicable for multi-scale optics in the infrared (IR) because: (1) wavelengths of operation are longer so the demands on process uncertainty are less; and (2) many IR transparent materials are brittle but amenable to

diamond machining. Germanium aspheric and freeform optics, in particular, are difficult to manufacture in any other way. Further, ultra-precision machining offers a single platform on which freeforms can be manufactured with low positioning uncertainty, thus allowing for ruling as a secondary process.

IR/thermal optical systems typically use materials with an index of refraction of 2.5-4 and thus there is a very high reflectivity at each surface: 18-36%, respectively. They thus require a sub-wavelength anti-reflective coating for proper function. Other sub-wavelength structures can produce phenomena ranging from polarization sensitivity to complex diffractive optical functions. Further, reduction of the number of surfaces to reduce reflective losses in IR systems is desirable. Thus replacing several conventional optics with one freeform optic [16] is desirable. One goal of this work is to enable the manufacture of a complex/freeform macro-lens shapes with an integrated sub-wavelength structure. In order to accomplish this, the cutting mechanics of ruling and other mechanical structuring techniques need to be understood. In this chapter, research on the cutting behavior of germanium is conducted using three cutting geometries: (1) ruling; (2) orthogonal cutting; and (3) milling. We report results from non-overlapping ruling tests with dead sharp and round nose tools. Cutting and thrust forces are measured and resultant normal and friction forces and friction coefficient are reported. Tests are also conducted to determine minimum spacing of ruling lines for optical applications. The effects of crystal orientation are also investigated.

4.2 Ruling of Germanium

4.2.1 Experiment Description

The workpiece material for all experiments was single crystal germanium with the (111) crystal orientation perpendicular to the top face. A Kistler 9245C2 dynamometer was used in all experiments, as shown in Figure 4.2. Three test configurations, shown schematically in Figure 4.3, were used: (a) Ramp-in/ramp-out with a round-nose tool; (b) ramp-in spiral with a round-nose tool; and (c) linear grooves with a dead-sharp tool. For each arrangement the tools were single crystal diamond with a rake angle α of -45° . The round-nose tool had a radius of 0.381 mm and the dead-sharp had a radius less than 100 nm. The relief angle for the round-nose and dead-sharp were 7° and 2.5° , respectively. The included angle of the dead-sharp was 60° .



Figure 4.2: Kistler 9256C2 MiniDyn, mounting plate, diamond tool, and workpiece in the configuration used during testing

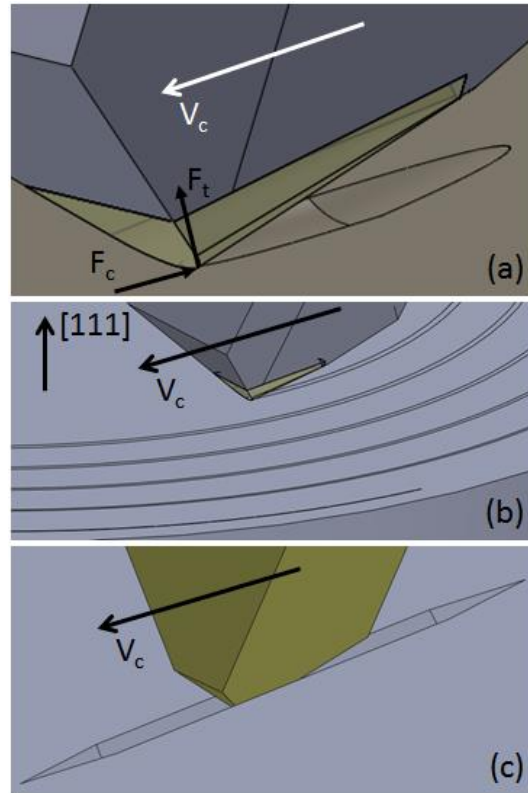


Figure 4.3: Cutting geometries (a) ramp; (b) spiral; (c) dead-sharp.

In arrangements (a) and (c), the cutting speed (V_c) is generated by the machine slides. In arrangement (b), the cutting speed is generated by coordinated C-axis motion (C-axis mode) to synchronize crystal orientation with force measurements. The dynamometer measured forces F_c and F_t at a sample rate of 1000 Hz for arrangements (a) and (b). The forces were too small to measure in arrangement (c). The cutting parameters for each arrangement are summarized in Table 4.1.

Table 4.1: Machining parameters for the three different ruling experiments

| Arrangement | V_c (mm/min) | Spindle Speed (RPM) | Depth of Cut (μm) |
|-------------|-------------------|------------------------|-----------------------------------|
| 1 | 100 | n/a | 0-2 |
| 2 | n/a | 10 | 0-2 |
| 3 | 100 | n/a | 0.05-0.2 |

4.2.2 Results

In arrangements (a) and (b) as the depth of cut increased, the cutting becomes more fracture dominated, and this causes an increase in fluctuation of the forces and surface pitting in the workpiece. In all cases, the amount of brittle fracture depended on crystal orientation. The spiral cut allowed us to measure the changes in cutting mechanics as a function of depth and crystal orientation simultaneously.

A representative micrograph of cuts made in arrangements (a) is shown in Figure 4.4. Forces in configurations (a) and (b) are shown in Figure 4.5. The data in Figure 4.5 (a) and (b) are both low-pass FFT-filtered at 60Hz and the data in (b) is additionally low-pass Gaussian filtered with a cut-off of 0.5 seconds. Figure 4.4 and Figure 4.3 (a) shows a ramp-in/ramp-out with a maximum depth 1 μm at 100 mm/min. Brittle fracture appears to dominant cutting forces at approximately 0.5 μm depth of cut. Figure 4.5(b) shows forces data from a spiral ramp-in with maximum depth of 2 μm at a spindle speed of 10 rpm at an increasing depth of 27.8 nm/rev. The slope of the force curve changes at approximate 0.5 μm , correlating with the ramp cut.

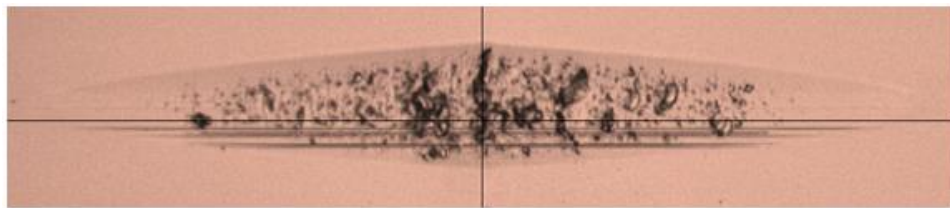


Figure 4.4: Micrograph of ramp in/out.

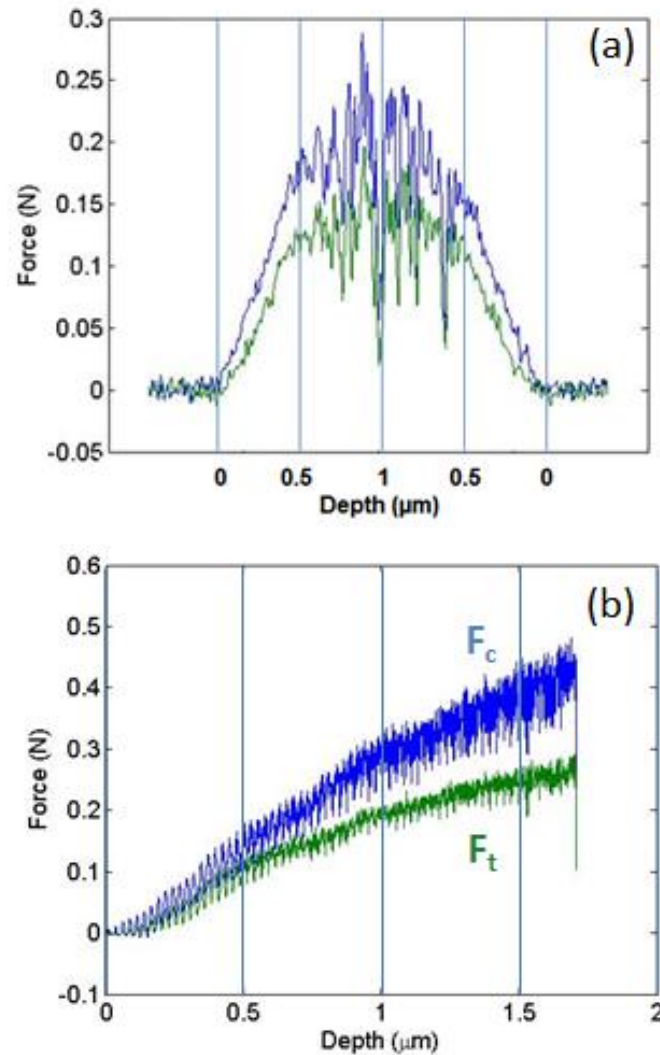


Figure 4.5: (a) Raw force signal samples.(ramp); (b) Raw force signal samples.(spiral)

The ramp tests were conducted at a number of depths of cut and crystal orientations. Figure 4.6 shows the cutting and thrust forces for 5 ramp experiments ranging in maximum depth from 0.25 μm to 1.25 μm at 100 mm/min at the center of the wafer in the same direction. To clarify the data for display, it was low-pass Gaussian filtered at 0.075 seconds. The 0.25 μm and 0.50 μm depths appear as smooth triangles, whereas the 750 nm, 1 μm and 1.25 μm cuts all show a marked transition corresponding

to the increase in brittle fracture occurring in the cutting. This further verifies the observation that increased brittle fracture appears to occur at 0.5 μm depth.

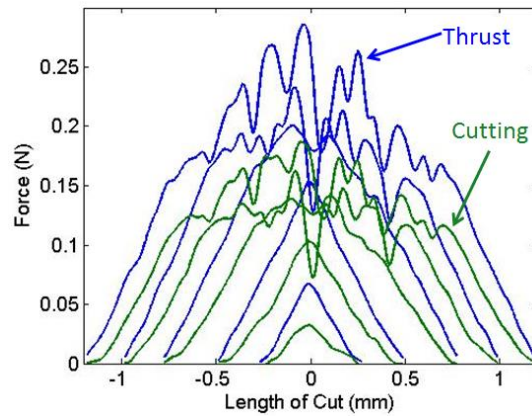


Figure 4.6: Ramp test force comparisons.

Configuration (c) is targeted at producing features with optical function. Linear grooves with a spacing near the wavelength of the light passing through will produce both a polarization sensitivity and an antireflective effect. Cross-cut grooves (i.e. two sets of grooves cut over one another at a 90 degree angle) will produce a strong antireflective effect.

Cutting tests show that this geometry of configuration (c) can produce well-defined grooves with little surface fracture, as shown in Figure 4.7. The groove depths range from 0.1-1.5 μm and the groove spacing ranges from 1-10 μm . To reduce the likelihood of fracture, grooves were cut to the final depth in several passes each below 200 nm and less than the 400 nm transition depth identified in the previous experiments.

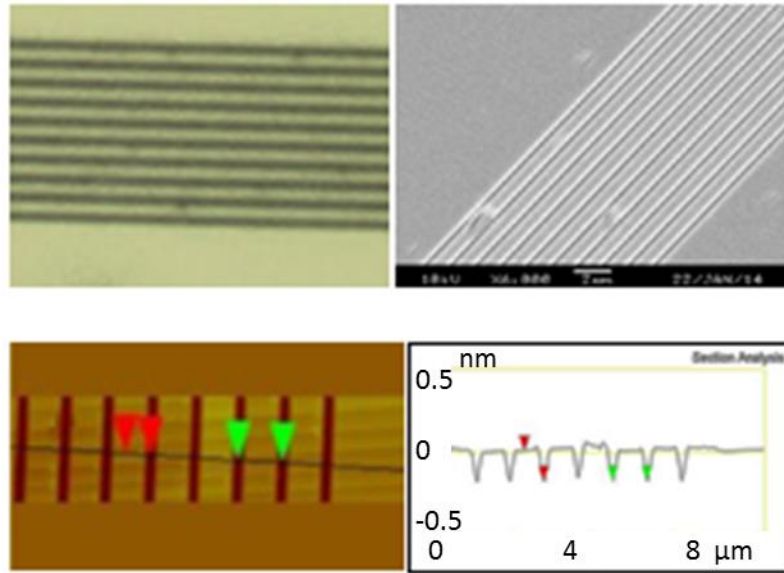


Figure 4.7: 10 grooves, 1 μm spacing, and 0.2 μm deep. (Top Left) Micrograph, (Top Right) SEM images, (Bottom Left) AFM scan, (Bottom Right) AFM Profile.

However, the direction of cut relative to the crystal orientation greatly affected the formation of fracture, as shown in Figure 4.8. Simply changing the cut orientation 90°, without changing the cutting geometry caused clean grooves Figure 4.8 (left) to become fractured Figure 4.8 (right).

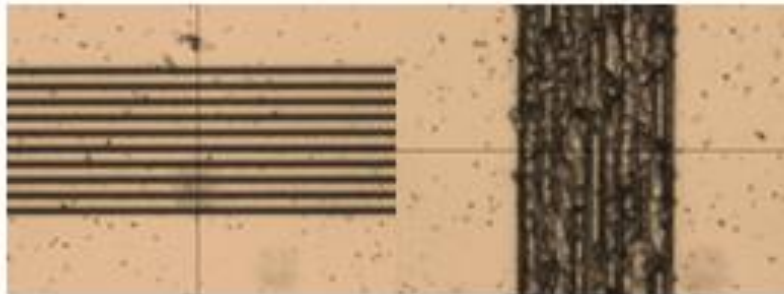


Figure 4.8: Grooves with similar parameters (3 μm spacing, 1 μm deep (left), 1.3 μm deep (right)) but orthogonal crystal orientation

4.2.3 Analysis

Force data was analyzed to identify, specific cutting energies/cutting force coefficients, normal and friction forces on the tool rake face and friction coefficient. The

data was analyzed with a Merchant model as shown in Figure 4.9. The friction force F and N are calculated using the following equations originally derived by Merchant [17], shown in Eq 4.1, Eq 4.2, and Eq 4.3.

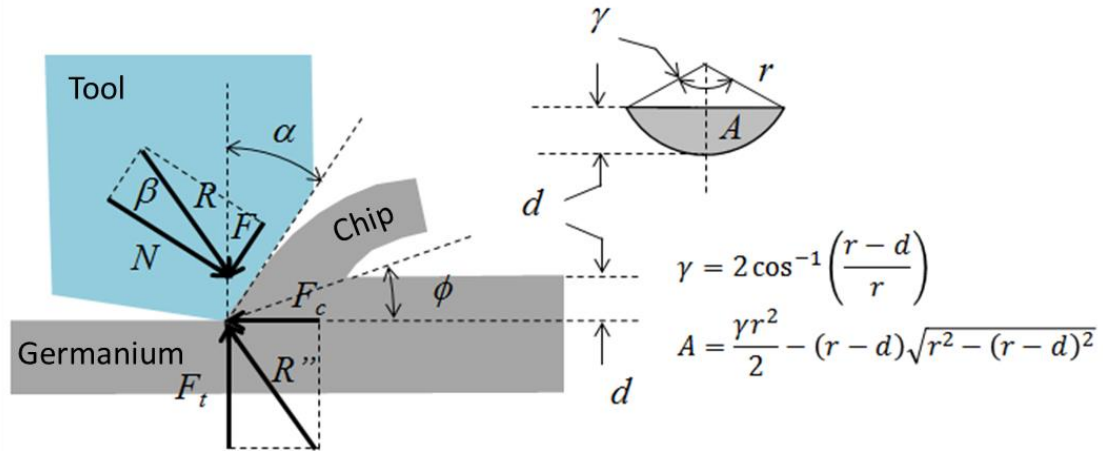


Figure 4.9: Cutting geometry and forces based on the Merchant model

$$F = F_c \sin \alpha + F_t \cos \alpha \quad \text{Eq 4.1}$$

$$N = F_c \cos \alpha - F_t \sin \alpha \quad \text{Eq 4.2}$$

$$\mu = \frac{F}{N} \quad \text{Eq 4.3}$$

Cutting force coefficients for the cutting and thrust directions were determined from Eq 4.4 and Eq 4.5.

$$K_c = \frac{F_c}{A} \quad \text{Eq 4.4}$$

$$K_t = \frac{F_t}{A} \quad \text{Eq 4.5}$$

In Eq 4.4 and Eq 4.5, A is the cross sectional area of the uncut chip - a section of a circle as shown in Figure 4.9.

The six ramp experiments were divided at the center of the cut (deepest point) overlaid. The mean and standard deviations of the cutting force coefficients as a function

of uncut chip area were calculated with a bucket size of 50 nm Figure 4.10. Error bars represent 2 standard deviations. At low depth/area of cut, K_c has a mean value just less than 10 kN/mm² and decreases to a value less than 5 kN/mm² at higher depths of cut/area. At low depth/area of cut, K_t has a mean value more than 30 kN/mm² and decreases to a value of approximately 6 kN/mm² at higher depths of cut/area. Figure 4.11 shows K_c versus chip area/depth for three different spiral cutting experiments. The values and trends are similar to Figure 4.10. The decrease in cutting force coefficients with increased chip area is correlated with the increase fracture dominated cutting mechanics.

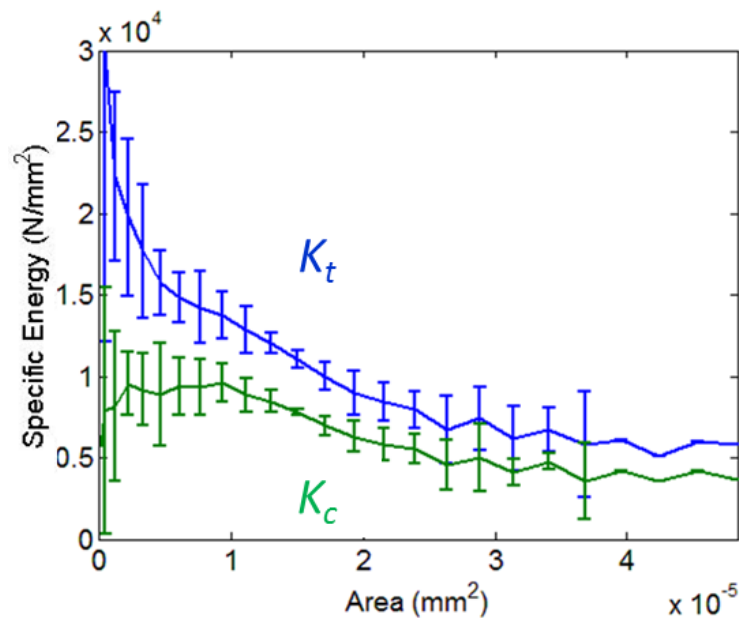


Figure 4.10: Specific Energy for the ramp-in/ramp-out round nose ruling

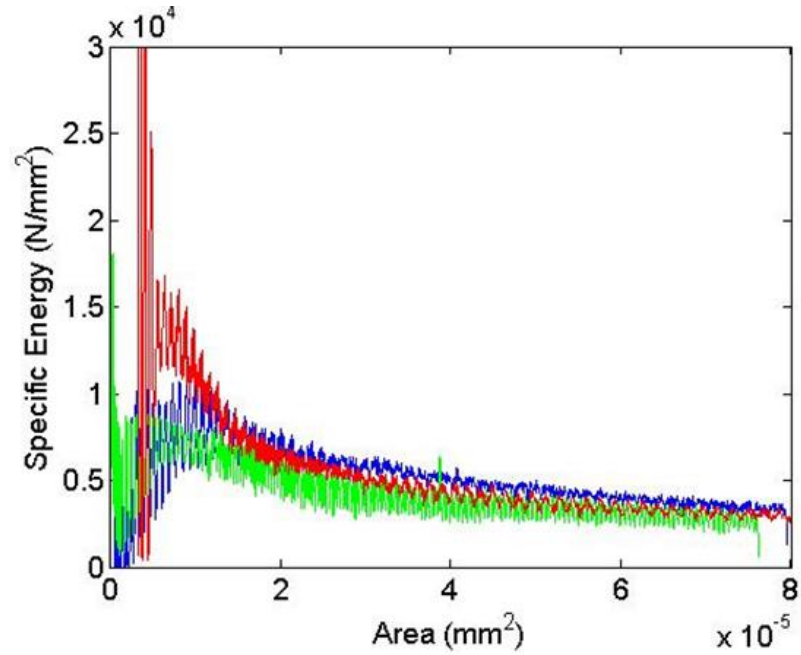


Figure 4.11: Specific Energy for the spiral ramp-in

Figure 4.12 shows F and N as a function of chip area for the three spiral cutting experiments. The normal force is higher than the friction force and this correlates to a relatively low value of the friction coefficient on the rake face of approximately 0.2 shown in Figure 4.13.

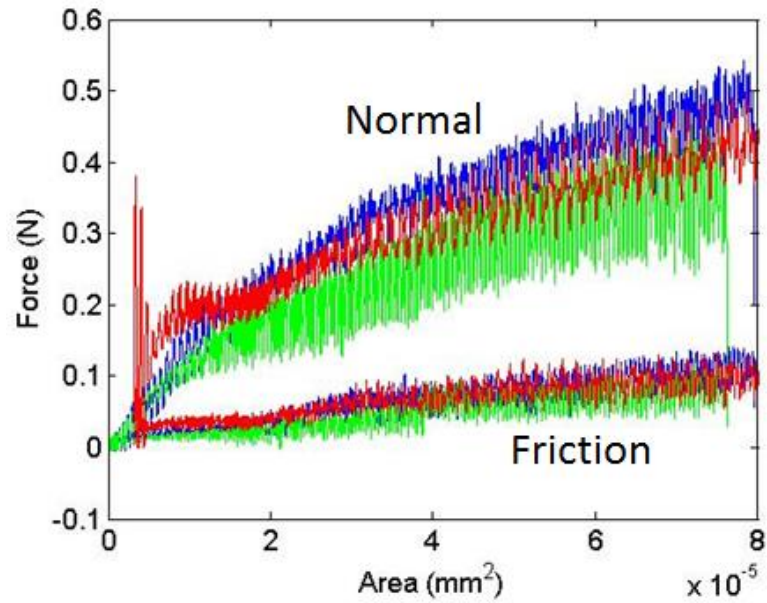


Figure 4.12: Spiral ramp: normal and friction forces.

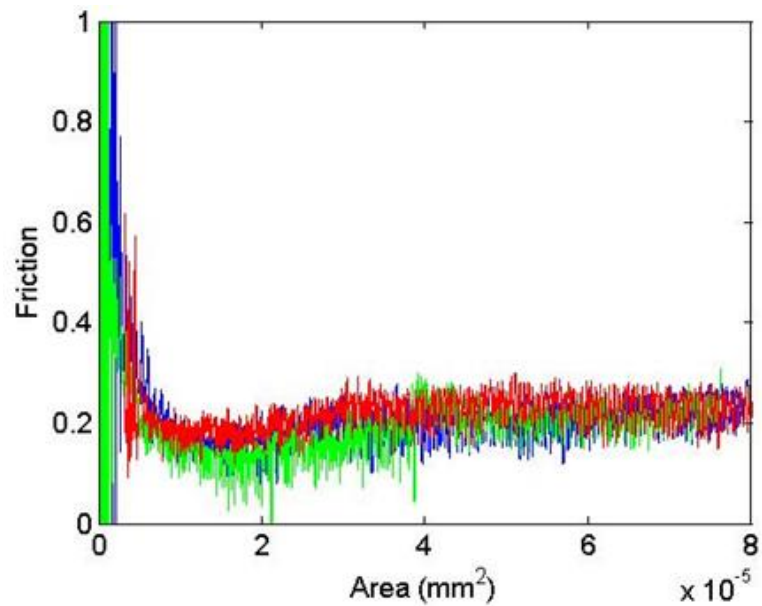


Figure 4.13: Spiral ramp: friction coefficient versus area.

In the spiral cutting arrangements, the force varies at three cycles per revolution. This correlated to the repetition in crystal orientations. At some orientations, more brittle chip formation occurred and led to a decrease in the average force. Figure 4.14,

shows the increase in the three-times per revolution force variation as a function of part rotation number and hence increased depth.

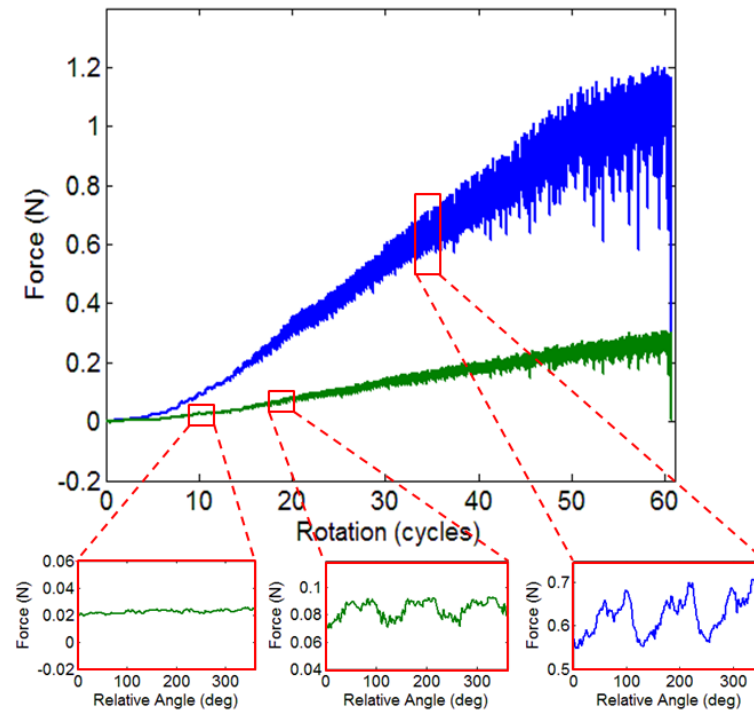


Figure 4.14: Spiral ramp: Cutting and Thrust forces showing the changes in force relative to different crystal orientations.

4.2.4 Discussion

The ability to structure an optical surface by ultra-precision ruling has many useful optical applications. Infrared optics are an application area because materials are diamond machinable and the wavelengths of operation are long, decreasing the required positioning uncertainty needed to produce a sub-wavelength structure. Here we have conducted fundamental ruling experiments in germanium to begin to identify cutting mechanics for successful ultra-precision ruling. The following are the key observations of the ruling experiments.

- Cutting forces show increased fluctuation and decreased mean amplitude as fracture begins to dominate the cutting mechanics.
- Cutting force coefficients decrease with depth of cut and the decrease correlates to fracture dominated cutting mechanics.
- Ruling behavior changes with crystal orientation for both dead-sharp and round-nosed tools.

4.3 Orthogonal Turning of Germanium

To further understand the cutting mechanics of germanium, orthogonal cutting tests were completed. The arrangement was modified from that described in Chapter 2 to include an angled adapter plate that imposes a negative rake angle at the cutting edge.

4.3.1 Experimental Description

The angled adapter plate produced a -25° rake angle when used with a nominal 0° rake tool. The adapter plate allowed the flexibility to rotate the tool in order to give a flat leading edge, but always keeping a constant rake regardless of the rotation of the tool. An image of the dynamometer setup is shown in Figure 2.6 showing the spindle, workpiece, coolant nozzle, an air jet used for cleaning the tool between tests, a riser block, dynamometer, adapter plate, and tool.

A -25° rake angle was selected to better represent the typical rake angle used when turning germanium. Also, since the tool needed to be tilted to achieve a negative rake, this weakens the cutting edge by increasing the clearance angle. So in order to better preserve the cutting edge, a lesser rake angle was selected over the -45° described in the ruling tests. All tests were performed with a chip width of 0.200 mm and a range of chip thicknesses from 10 nm up to 10 μm . Measurements were taken with a constant

surface speed of 4 m/s with varying chip thickness and with variable cutting speeds with constant chip thickness of 0.2 μm and 0.5 μm .

4.3.2 Results

4.3.2.1 Force Versus Chip Thickness

The cutting parameters span nearly 3 orders of magnitude in feed per revolution. To better depict the trends in the results, a logarithmic scale has been used for the fpr axis of the plots. A small overlay plot with linear axes to is also overlaid.

Unlike the IRG 26, cutting forces in germanium continuously increase with uncut chip thickness as shown in Figure 4.15. At lower chip thicknesses, the thrust force is greater than the cutting force. A negative rake angle tends to increase the ratio of thrust to cutting force such that it is sometimes greater than 1. However at a t_c of approximately 60 nm/rev the cutting force begins to exceed the thrust force suggesting an edge effect - the edge radius is causing a higher effective rake angle and thus an even greater thrust force [14].

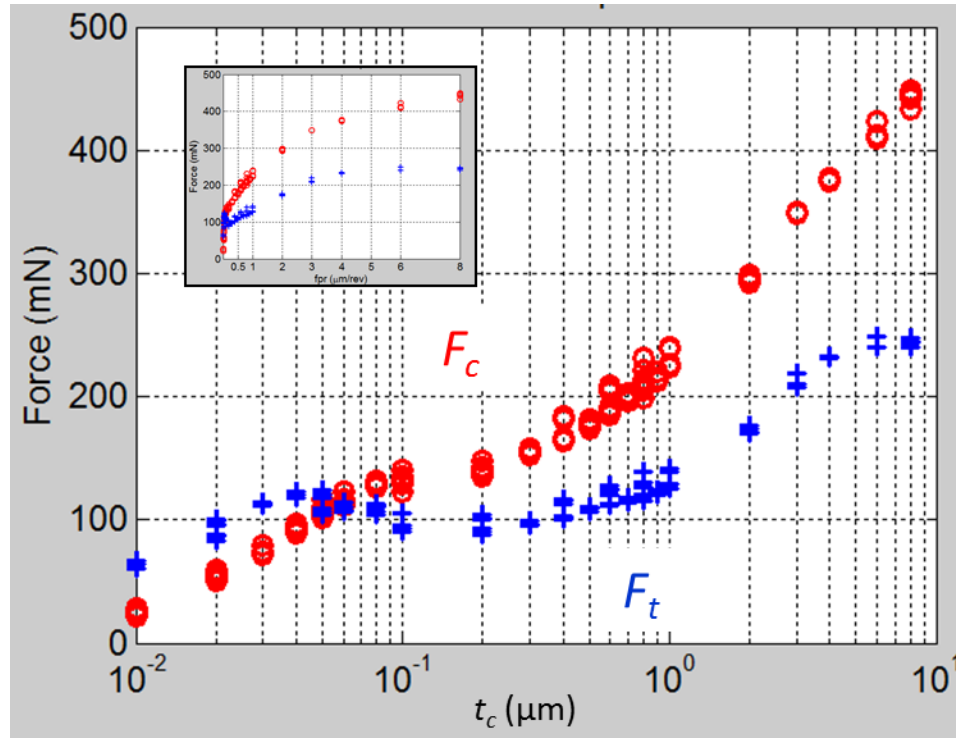


Figure 4.15: Cutting and thrust forces for orthogonal turning of germanium at 4 m/s cutting speed (inset shows same data range but with linear scales)

The cutting force coefficients are computed and shown in Figure 4.16. The linear scale plot shows the significant decrease in force coefficients until a t_c of approximately 200-300 nm. The decrease in force coefficients continues even below 0.5 kN/mm^2 . This is inconsistent with the planing tests that showed the cutting force coefficient leveling off around 5 kN/mm^2 .

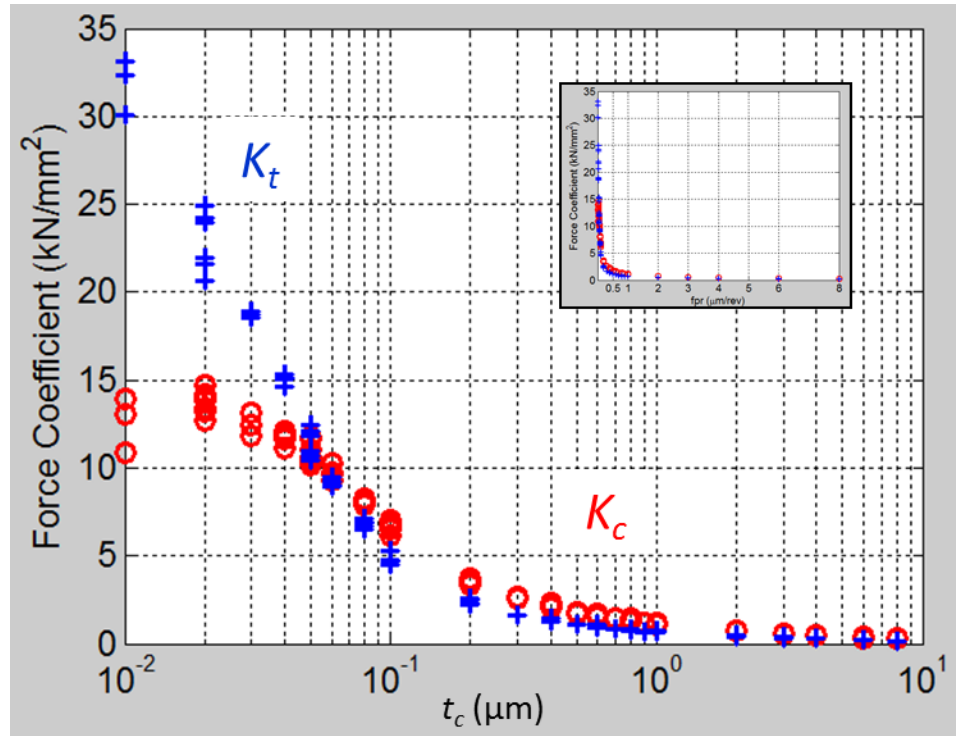


Figure 4.16: Force coefficients for orthogonal cutting of germanium with a cutting speed of 4 m/s (inset shows same data range but with linear scales)

The cross over in the force curves occurring at a t_c of 60 nm also coincides with the resultant force (shown in Figure 4.17) dropping below 45°. This may correspond to a more tensile region of stress in the cutting zone and the onset of brittle fracture.

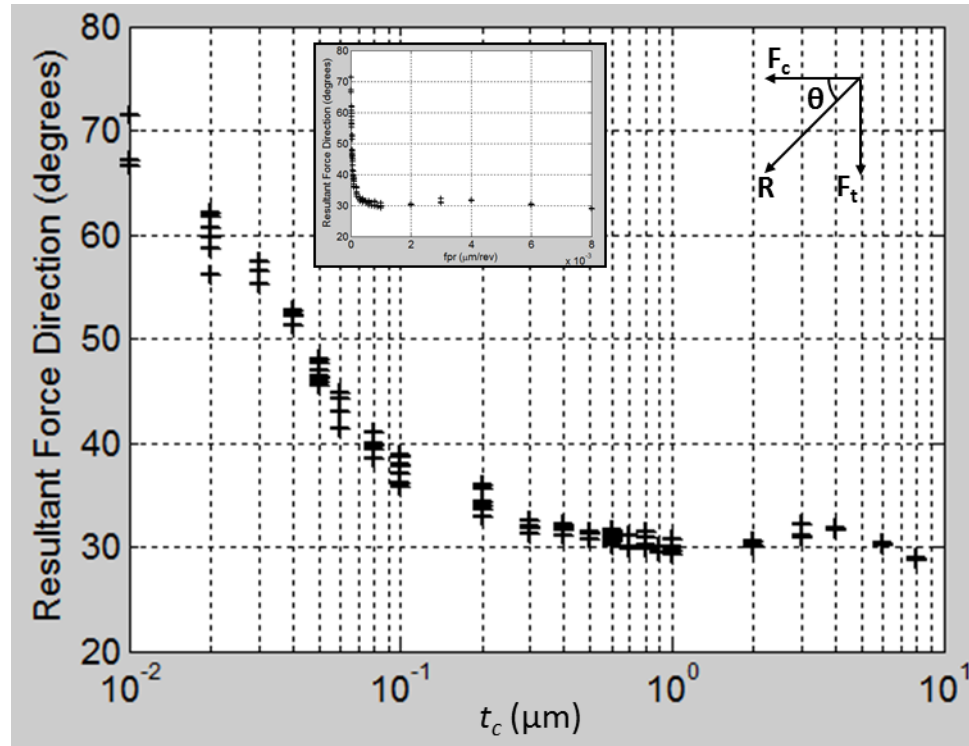


Figure 4.17: Resultant force direction of germanium orthogonal cutting at 4 m/s cutting speed (inset shows same data range but with linear scales)

4.3.2.2 Force Versus Speed

Other than the anomalous result discussed, a speed effect has not been verified in IRG 26. However, germanium shows a significant speed dependence, seen in Figure 4.18, Figure 4.19, and Figure 4.20. Two different chip thicknesses were measured for the same range of cutting speed: 200 nm and 500 nm. Both chip geometries showed a drop in forces by at least half from the slowest speed (0.5 m/s) up to the fastest speed (8 m/s). This may suggest that the higher speeds are causing more fracture in the material and the slower speeds are producing a more “ductile” type cut. If the germanium is undergoing a metallic phase transformation the drop in force may also be due to temperature. Further research is required to understand the phenomenon.

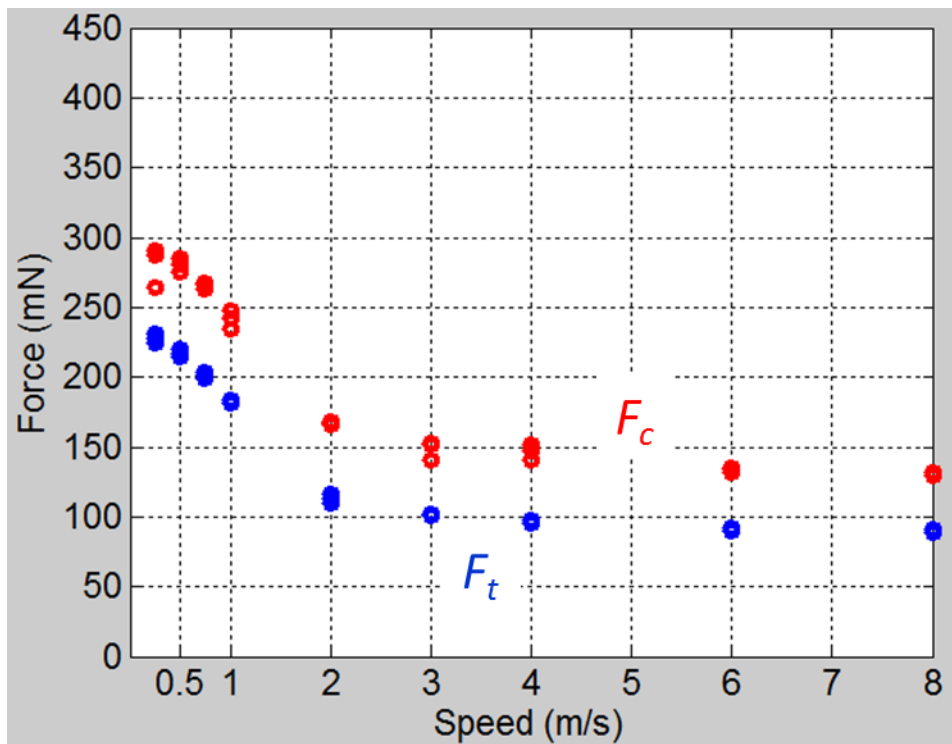


Figure 4.18: Force versus speed for a constant t_c of 200 nm

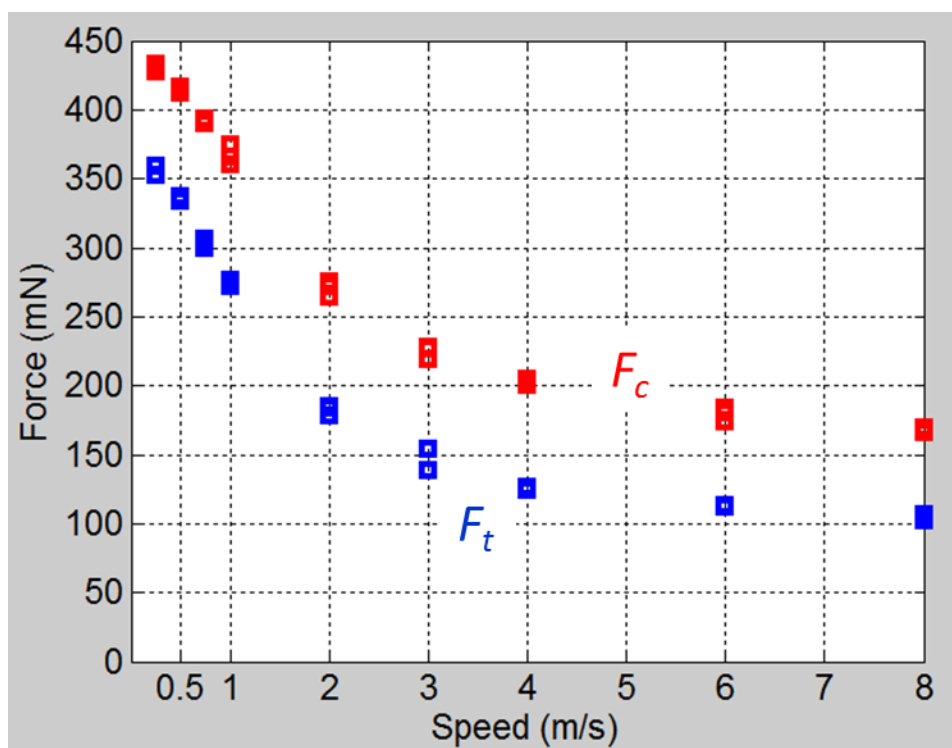


Figure 4.19: Force versus speed for a constant t_c of 500 nm

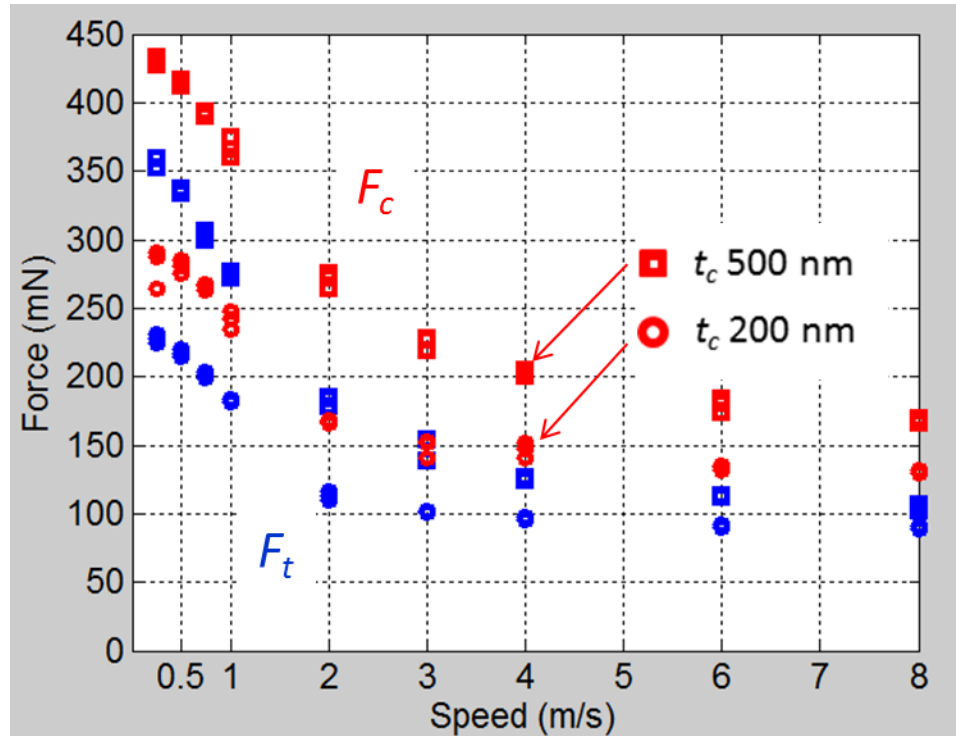


Figure 4.20: Force versus speed for two t_c values of 200 nm and 500 nm as shown.

As expected the lower chip thickness shows a higher cutting force coefficient, shown in Figure 4.21. The qualitative character of the curves for the two values of t_c appears to be similar. Thus, for the two chip thicknesses tested, the cutting mechanics that leads to the speed dependence appears to be the same.

One common mechanism for decreased cutting force with speed is thermal softening. To determine whether that is possible here we can use the measured specific cutting energies to estimate the average temperature rise in the chip and compare to the melting temperature of germanium (938°C). The highest value measured for K_c in germanium is approximately 12.5 kN/mm² or 12.5 J/mm³. The thermal mass of a cubic millimeter of germanium is $m * c_p$ where c_p is the specific heat (320 J/kg-°C). One cubic millimeter of germanium has a mass of $5.323 * 10^{-6}$ kg. Thus, the thermal mass is $1.7 * 10^{-3}$ J/°C. If we assume half the cutting energy is contributing to ductile deformation

and heat generation in the chip and half is overcoming friction at these low depths of cut. Further since diamond is highly conductive ($2200 \text{ W/m}\cdot\text{C}$) we might assume only 25% of the heat remains in the chip. In that case the average temperature rise would still reach the melting temperature of germanium. Therefore it seems possible that thermal soften could be playing a role but further investigation is needed.

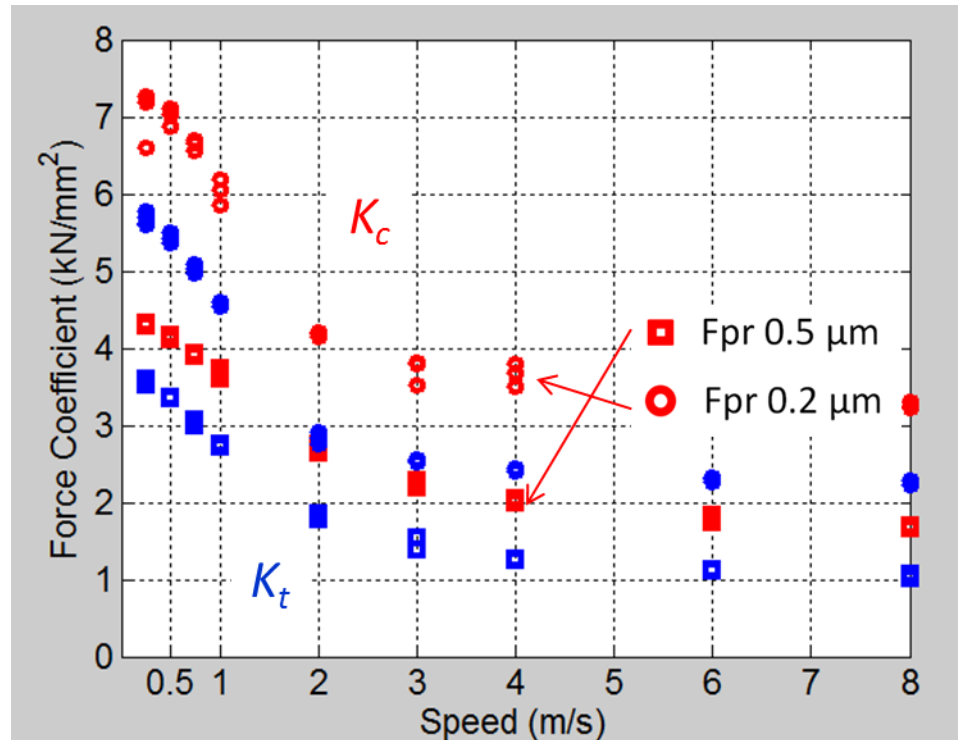


Figure 4.21: Force coefficients from the forces shown in Figure 4.20

After observing a change in cutting force by only varying speed, the cutting tests when varying t_c with a constant 4 m/s speed were repeated but with a speed of 0.5 m/s, results are shown in Figure 4.22 combined with data from Figure 4.15. To elucidate trends, data for Figure 4.22 has undergone further processing. Each test was divided into “buckets” of data with a bucket width of one revolution of the spindle. The mean and standard deviation of each bucket was found and designated as a single data point. Then the mean of the entire test consisting of 80 revolutions and therefore 80 data points was

determined. The mean and standard deviations were then combined for each repeated test with identical parameters: 3 tests with 80 revolutions in each for a total of 240 data points. The trend lines represent the change in mean for and the error bars represent two standard deviations.

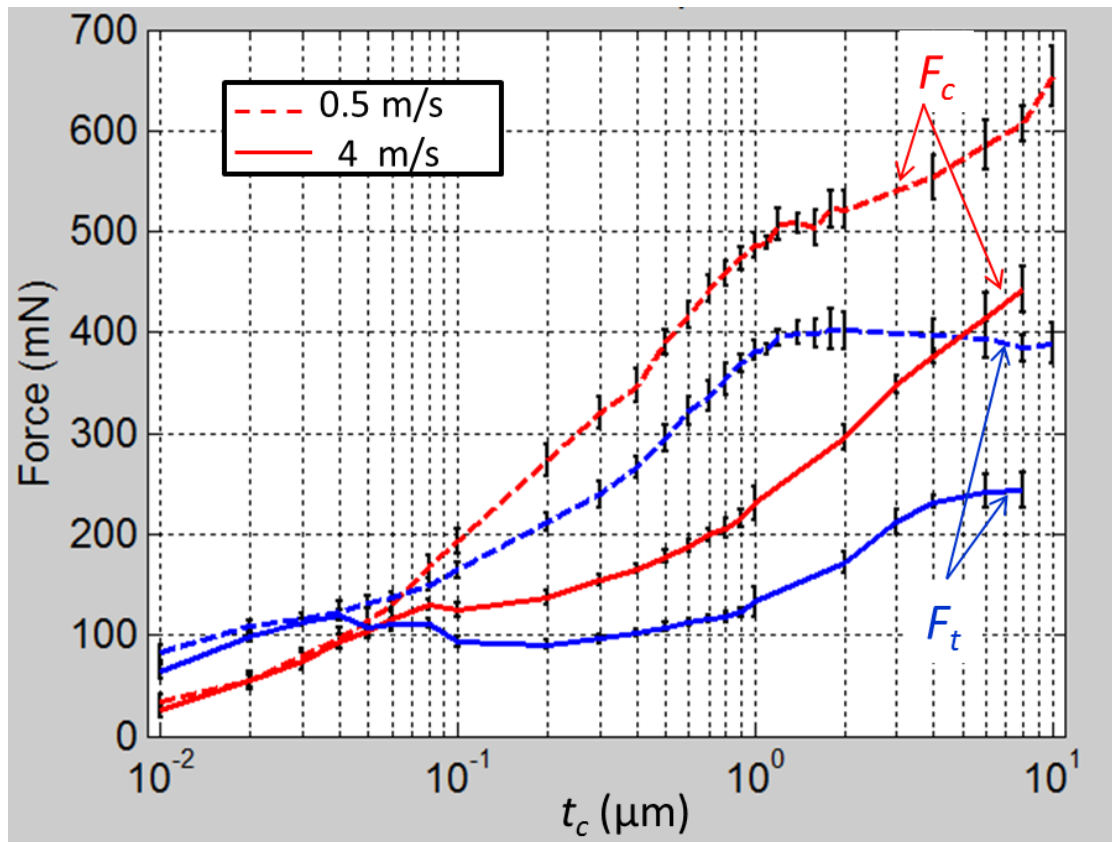


Figure 4.22: Varying feed/rev with two different surface speeds, 0.5 m/s (dashed lines) and 4 m/s (solid lines). Error bars show $\pm 2\sigma$.

4.3.2.3 Force Versus Spindle Position

It has been shown by many [16] that the single crystal infrared material like germanium and silicon have a cutting force that depends on the crystallographic orientation of the material. In the spiral experiments, the force was seen to vary three times per revolution. In the orthogonal turning, the same is true. A sample test was selected to demonstrate the crystal orientation effects on the cutting forces in orthogonal

cutting. The sample test had the following parameters: 0.5 m/s cutting speed, 0.200 mm chip width, and 200 nm/rev chip thickness. After the lead-in and lead-out of the test were cropped, about 75 revolutions of data remained. Figure 4.23 shows the cutting and thrust forces during the remainder of the test. What appears to be a noisy signal is in fact a 100 mN of force variation due to the orientation of the crystallographic structure. The inlay of Figure 4.23 represents a section of the force data only showing 2 revolutions of data. The cyclic force variation with a frequency of three cycles per revolution is evident.

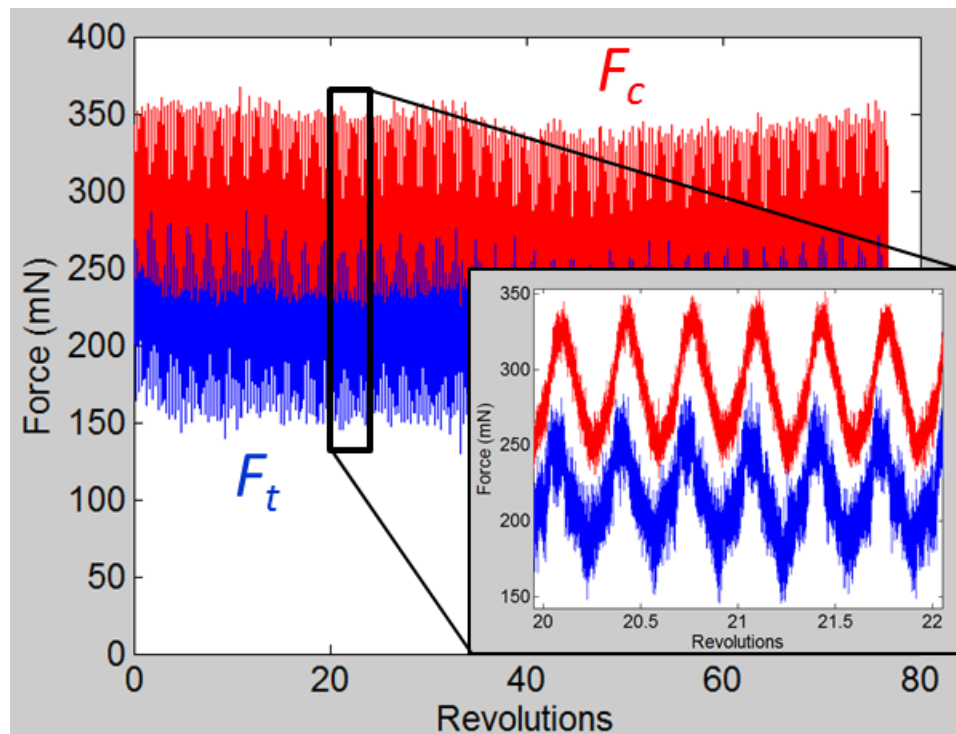


Figure 4.23: Example force measurement showing crystal orientation effects on force

In order to analyze the entire test worth of data, the relative angle for each point was computed and reduced to angles between 0° and 360° . Then points were found in buckets of 3° wide and the forces were averaged and a standard deviation was found. Figure 4.24 shows the relative spindle orientation with $\pm 1\sigma$ error bars at 3° bucket widths. Several things are interesting about the resulting plots: (1) the variations show higher

harmonic content likely related to the six cycles per revolution frequencies observed by Horiuchi et al. [16]; (2) the thrust force shows an apparent discontinuity, not directly seen in the cutting force; (3) there appears to be a phase lag in the thrust force relative to the cutting force. Points (2) and (3) have not been observed previously in literature, perhaps because little data on orthogonal cutting of single crystal germanium exists. The data points towards future research directions on the modeling of cutting mechanics and the effect of crystal orientation of cutting forces.

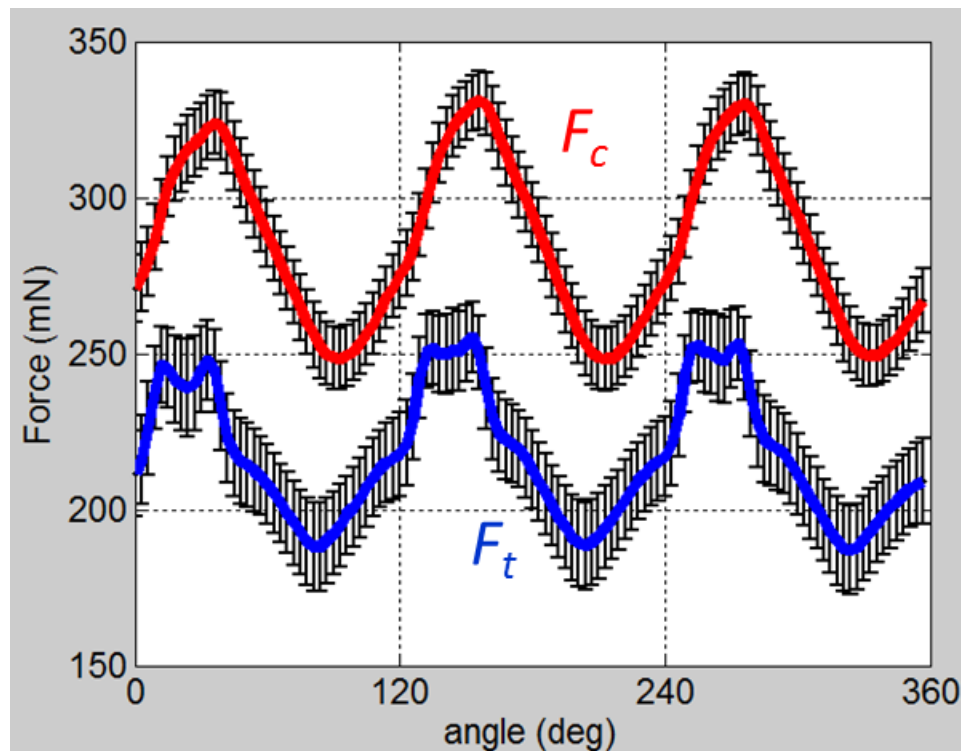


Figure 4.24: Averaged force measurement every three degrees of spindle rotation

4.3.3 Analysis

The Merchant [49] model was used to compute the normal and friction forces on the rake face. Figure 4.25 shows the normal and friction forces using an angle of -25° in the Merchant model. Looking at the results of the Merchant model shows that the friction force stays relatively low throughout the range of t_c 's and the normal force

continues to rise. It is unclear from the results where (or if) a ductile/brittle transition occurs. Each test performed removed the previous surface created therefore making surface quality inspection impossible for this configuration.

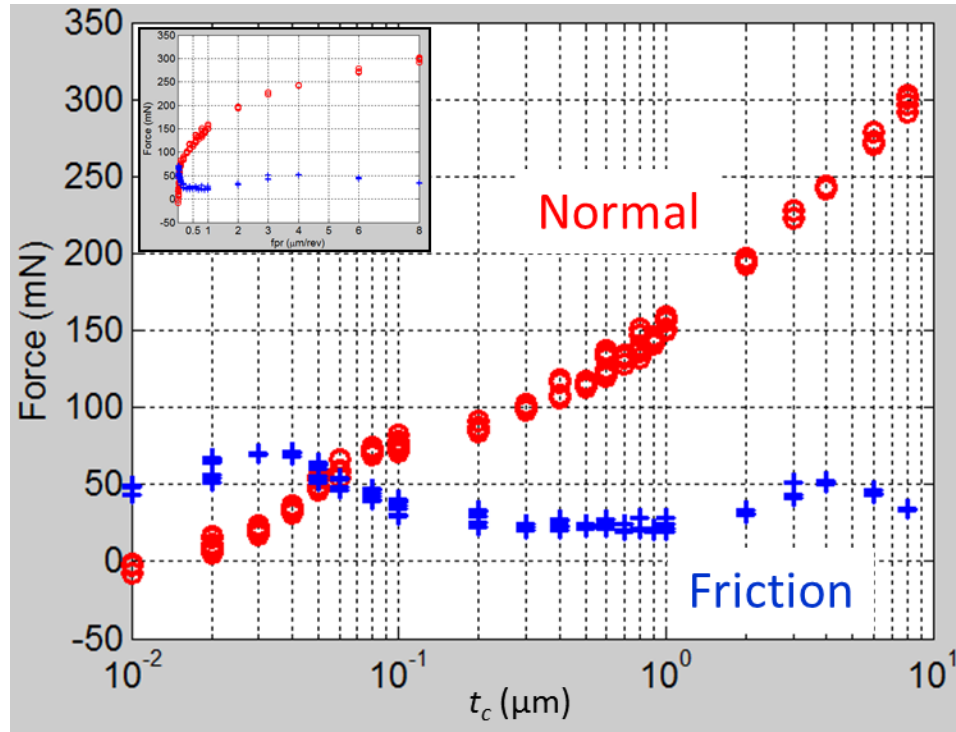


Figure 4.25: Normal and friction forces of orthogonal cutting of germanium at a cutting speed of 4 m/s

CHAPTER 5: TOOL ERROR CORRECTION

5.1 Introduction

Machine tool geometric and thermal errors are the dominant source of error in the machined part for conventional machining. However, in ultra-precision machining, the errors in the tool geometry are relatively large, and can be the dominant source of errors in the machined part. In ultra-precision milling, tool errors, both static and synchronous dynamic errors, are a large source of error. In order to correct the effect on surface form error a new procedure was developed to calibrate and correct the errors of the tool.

This is an extension of the correction methods used in diamond turning for tool decentering. However, the complex three dimensional and dynamic nature of milling makes the situation much more complicated. A new procedure for correcting milling tool errors is outlined in this chapter.

5.2 Sources of Tool Errors

The three sources of tool error are: absolute radius, tool location, and edge waviness. The latter two are shown in Figure 5.1. For stable machining, tool location error arises from static misalignment of the diamond tool relative to the axis of rotation and from dynamic errors that are synchronous with the spindle rotation. Diamond waviness is a deviation in the form of the tool shape from a perfect circular shape with a given radius of curvature.

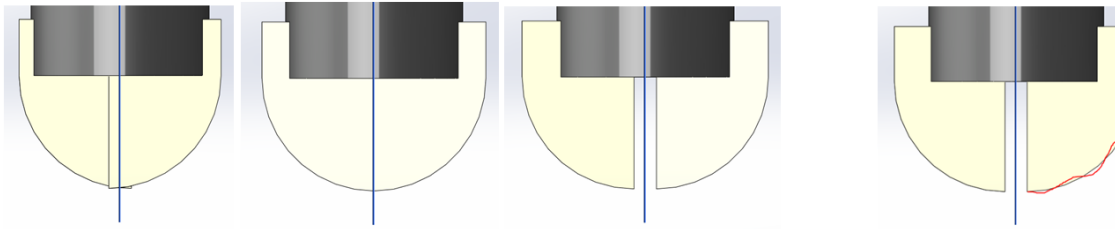


Figure 5.1: Tool Location Error (left) and Diamond Waviness (right)

5.2.1 Tool Location Error

Tool location error can be defined as a radial shift of the diamond relative to the axis of rotation. One method for correcting this error is to cut and measure an artifact, for example a sphere, and measure the difference between the artifact and the programmed shape. Then the part program is adjusted assuming a radial error and a corrected artifact is cut assuming an imperfect tool. In order to do this, the radial error of the tool must be determined from the form error on the machined artifact. Correction for tool decentering is done in diamond turning. The method for radial error in flute location in milling can be derived from that method. Tool location error detection in diamond turning is accomplished by turning a sphere with the tool and measuring the deviations of the artifact from a “perfect” spherical shape. These errors qualitatively have the shape of an “M or W” and can be measured, for example, on a Fizeau interferometer. In Figure 5.2 on the left, the location of the flute of an end mill relative to the center of rotation is shown with the center figure showing zero errors. On the right are the errors from the perfect spherical shape which are qualitatively M-shaped (top left) or W-shaped (bottom left).

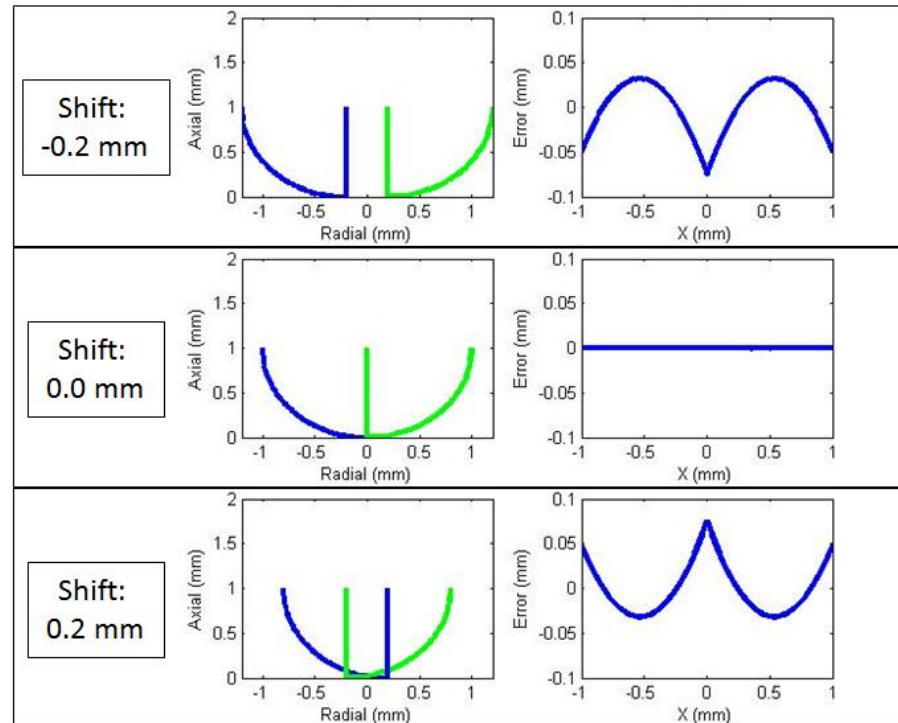


Figure 5.2: Demonstration of an M or W residual form error. The images on the left side show the possible positioning error/shift of the end mill flute relative to the rotational axis of the spindle.

5.2.2 Diamond Waviness

Once the tool location error has been determined and corrected, the remaining of the rotationally invariant errors is due to the diamond edge waviness. Diamond tools can be manufactured with “controlled waviness” – the waviness is measured and corrected periodically during the manufacturing operation. A typical “controlled waviness” diamond has a peak-to-valley error 20-100 nanometers and a “non-controlled” diamond can have up to 2 μm of peak-to-valley error. If an accurate method for correcting diamond waviness can be developed, as demonstrated here it may not be necessary to spend the additional cost of a “controlled waviness” tool to achieve optics with well controlled form errors.

5.3 Measuring Tool Errors

An alternative technique for correcting for tool errors would be to directly measure the tool edge at various positions and generate a map of tool error versus angle around the tool nose. These values could then be used to make a correction to the machine position as a function of the angle of the surface tangent (contact point) on the part being cut. The difficulties of this procedure are: (1) uncertainty in the tool measurement system; (2) verification that the tool edge measured is the edge that would actually generate the part surface; (3) the measurement of the tool errors is static and does not take into account errors from synchronous vibration as in milling; (4) damage to the tool by the measurement device. An artifact based technique avoids many of these error sources. Such a technique was developed in this work.

5.3.1 Calibration Artifact

The calibration artifact must sample/measure the errors of the tool around its useable periphery and be measurable by a technique with uncertainties less than the form errors allowed in the final component. The calibration artifact geometry selected was an 8 mm radius of curvature sphere with an aperture of 8 mm. This geometry gives a total of 60° angle or $\pm 30^\circ$ sweep of a circle shown in Figure 5.3 below. For the case where the spindle is aligned perpendicular to the XY-plane, 30° of the milling tool starting from the tip would be used to generate the surface (for a turning tool, only one side of the tool would be used) shown in Figure 5.4.

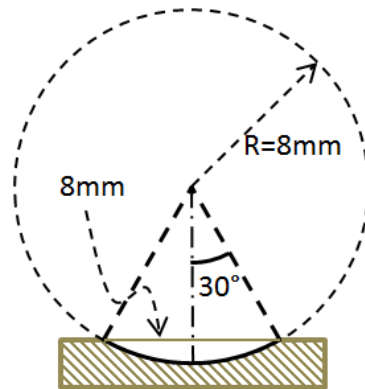


Figure 5.3: Calibration artifact cross-sectional geometry showing $\pm 30^\circ$ of an 8 mm radius of curvature sphere with an 8 mm aperture

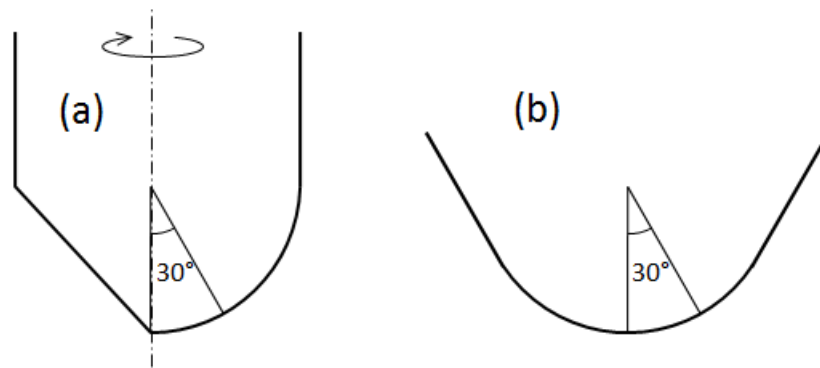


Figure 5.4: Schematic of the rake face of a milling tool (a) or turning tool (b) showing the amount of cutting edge measured in the standard calibration artifact shown in Figure 5.3

The original procedure was to machine the calibration artifact with the same machining parameters as those intended for the final optic. However the process of machining the artifact is thus slow. For example, the first artifact was an IRG26 sphere machined with a 0.005 mm stepover and a 0.0025 mm/rev feedrate, but the cycle time was a few hours per part and it was decided that we needed a faster solution. Simulations showed that the geometric errors incurred by using more aggressive parameters were small compared to the tool errors. Thus, the second IRG26 sphere was machined with a 0.020 mm stepover and a 0.005 mm/rev feedrate finishing in just under 30 minutes. The

faster cycle time allowed for multiple artifacts to be machined and corrected in a single day.

5.3.2 Metrology of Calibration Artifact

The calibration artifact would be measured on a Zygo Verifire™ Fizeau Interferometer (Figure 2.4) using a transmission sphere with an F/# of 0.75. The F/0.75 transmission sphere (83.6° sweep) used would help to ensure that the entire artifact (60° sweep) would be measured and the aperture of the measurement corresponded to the aperture of the artifact and not the aperture stop of the measurement system.

The settings used in the interferometer measurements were: 16 averages, 7% threshold, and no optical zoom. The analysis within the Zygo software was only used to ensure a good quality measurement, but the raw data was exported to MATLAB® in order to finish the full analysis.

5.4 Analysis of the Calibration Artifact Measurement

MATLAB® R2013a is the software used to analyze the raw data of the calibration artifact measurement. The procedure for analyzing the data follows the following steps:

1. Read the Z height values z_0 and the pixel size from the raw data file, see Figure 5.5.

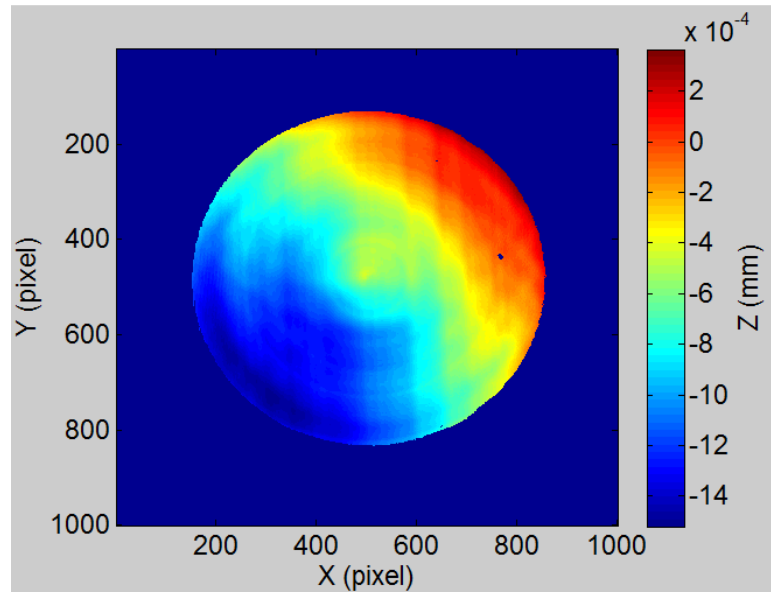


Figure 5.5: Calibration artifact measurement raw height data

2. Define the corresponding X and Y value arrays centered on the non-NaN (Not-a-Number) values of Z.
3. Calculate Z Remove the best fit Zernike terms for piston, tilt, and power from Z_0 , see Figure 5.6.

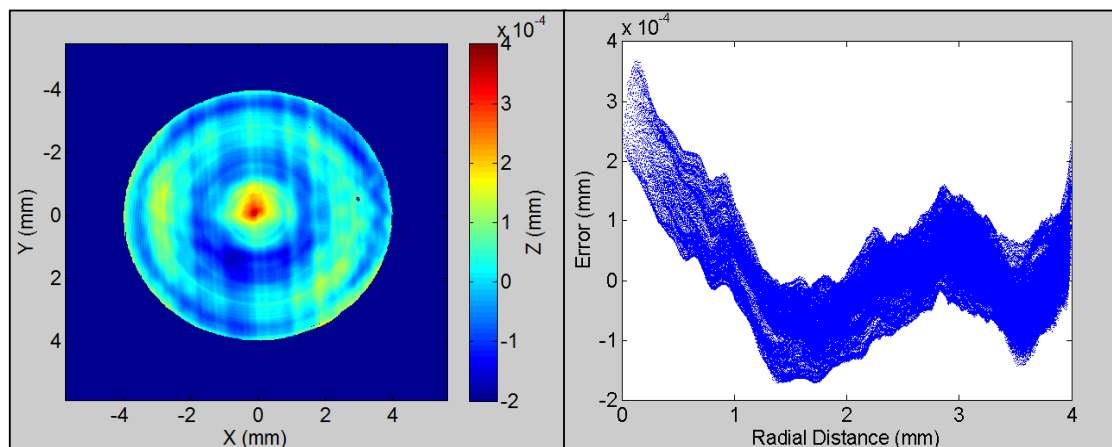


Figure 5.6: Calibration artifact measurement with the best fit Zernike terms for piston, tilt, and power removed

4. Change from Cartesian to polar coordinates ($X \ \& \ Y \rightarrow R \ \& \ TH$).

5. Trim the aperture to only allow points less than or equal to the radius of the known aperture.
6. Create a sphere Z_{base} with the programmed radius of curvature and add it to Z in order to simulate the true shape Z_{act} of the sphere instead of the deviation from a sphere, see Figure 5.7.

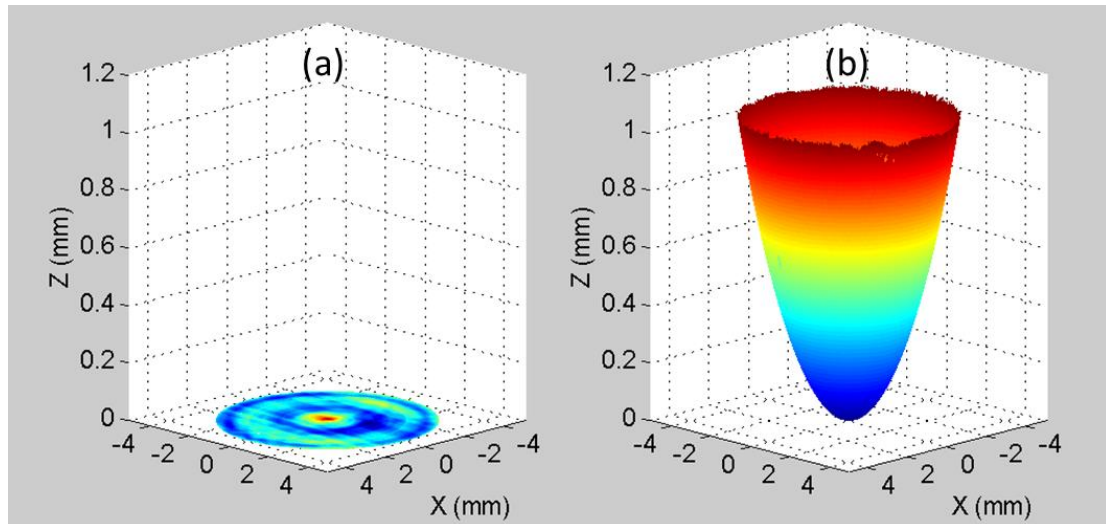


Figure 5.7: Calibration artifact measurement before (a) and after (b) adding a sphere with the same radius of curvature as the programmed part

7. In a loop (see Figure 5.8) :
 - a. Add a known `shift` to the polar coordinate R to get R_{new} .
 - b. Switch R_{new} back to Cartesian coordinates X_{new} and Y_{new} .
 - c. Find the best fit sphere of Z_{act} with the X_{new} and Y_{new} .
 - d. Subtract the best fit sphere from Z_{act} to get $Z_{stretch}$.
 - e. Find the peak-to-value PV of the difference.
 - f. Repeat the loop with a new shift value.

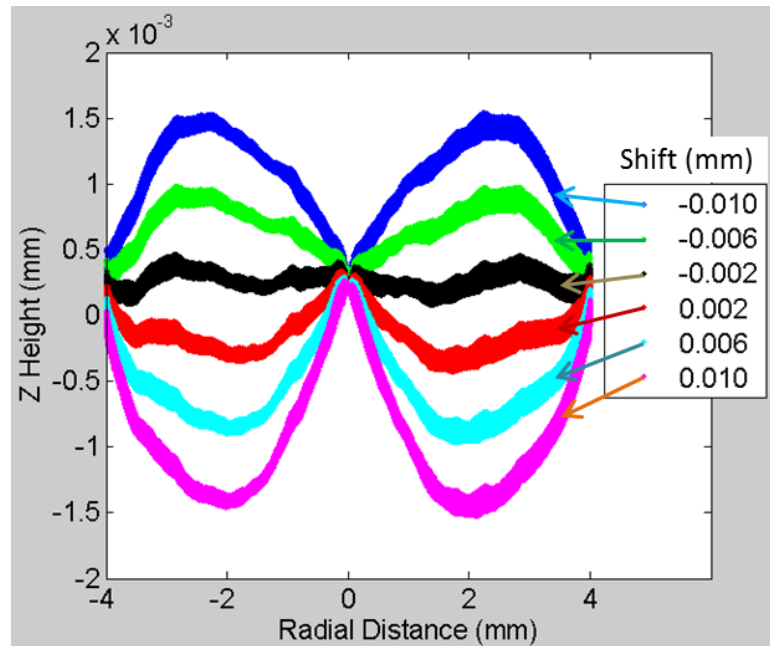


Figure 5.8: Varying the shift and removing best fit sphere

8. Find the shift value corresponding with the minimum PV found in the previous step, see Figure 5.9.

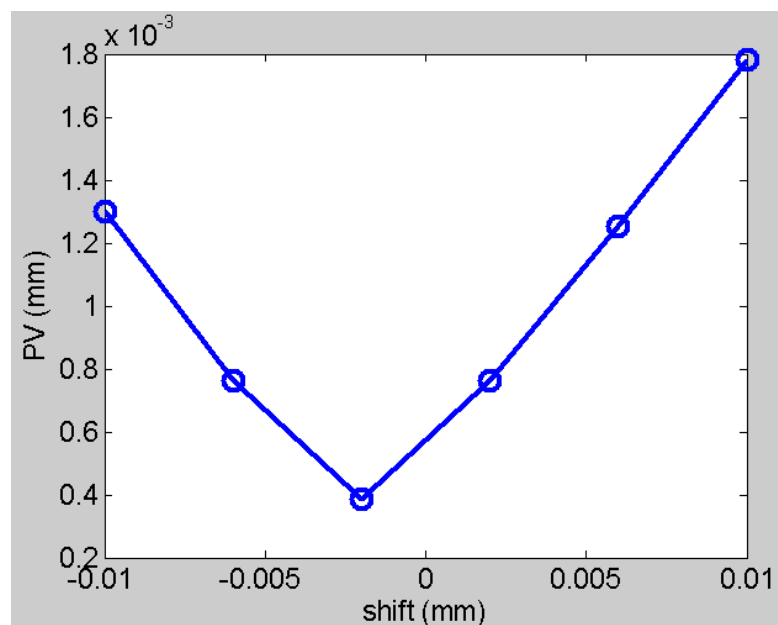


Figure 5.9: Coarse shift range with the PV error of the data shown in Figure 5.8

9. Repeat steps 7 and 8 reducing the resolution and range of `shift` narrowing in to a more precise value for `shift`, see Figure 5.10 and Figure 5.11.

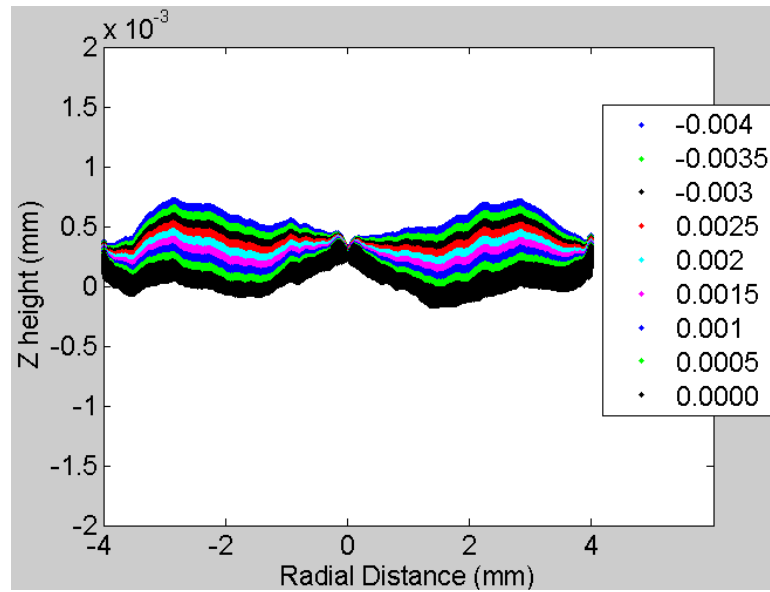


Figure 5.10: Finer resolution radial shifting to narrow in on a minimum PV

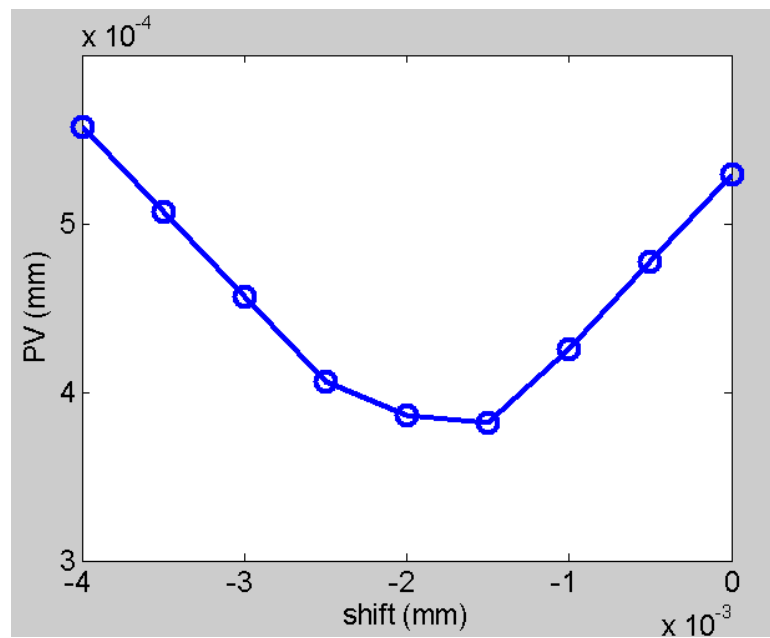


Figure 5.11: Fine `shift` range with the PV error of the data shown in Figure 5.10

10. After finding the desired `shift`, use that value to shift `R` to get `Rnew` to simulate the surface that would be created after correcting only tool location error, see Figure 5.12.

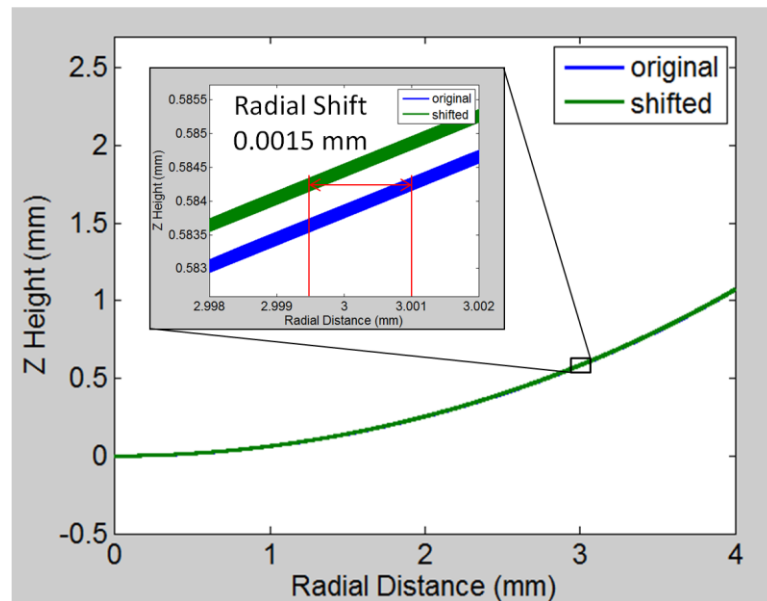


Figure 5.12: Radially shifted data showing before and after comparison

11. Switch back to Cartesian coordinates ($R_{new} \ \& \ TH \rightarrow X_{new} \ \& \ Y_{new}$).
12. Remove the best fit sphere from `Zact` using `Rnew` in order to simulate the residual error left over after correcting tool location error, `Zshifted`, see Figure 5.13.

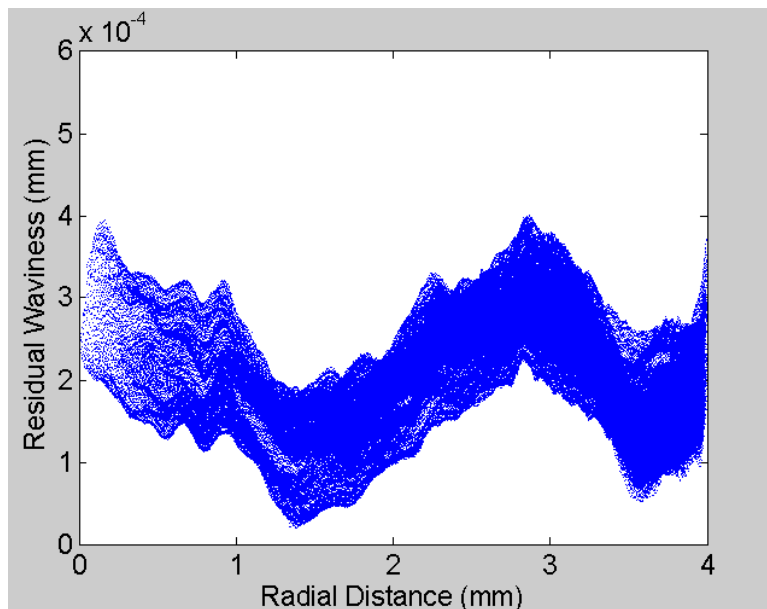


Figure 5.13: Residual waviness versus radial distance from the center after applying the desired `shift` and removing the best fit sphere

13. Compute the `Slope` of the nominal spherical surface at `R`, see Figure 5.14. The deviation in slope between the nominal and actual sphere is negligible since the returned values from the interferometer are directly related to a slope not position.

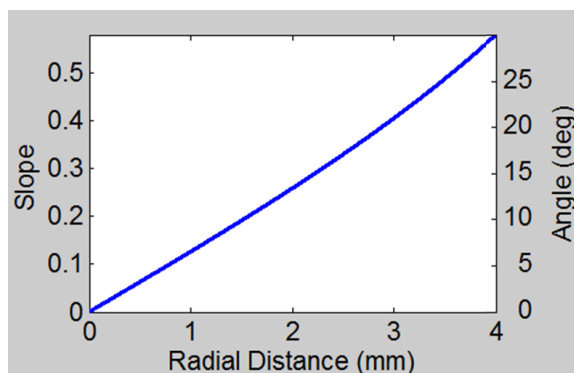


Figure 5.14: Slope/angle versus radial distance of an 8 mm radius of curvature sphere

14. Fit a polynomial to `Zshifted` and the `Slope`, Figure 5.15.

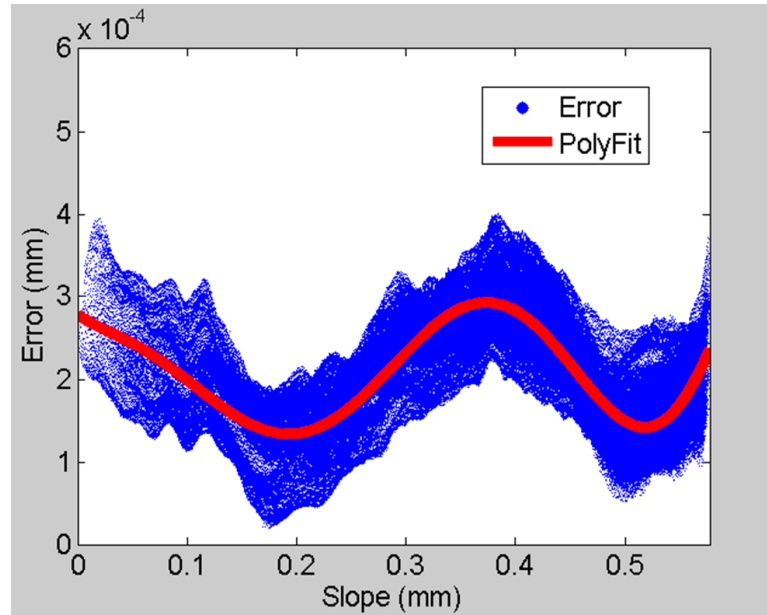


Figure 5.15: Slope dependent error with an 8th order polynomial fit

15. Estimate the final residual error after correcting the slope dependent waviness of the tool, Figure 5.16.

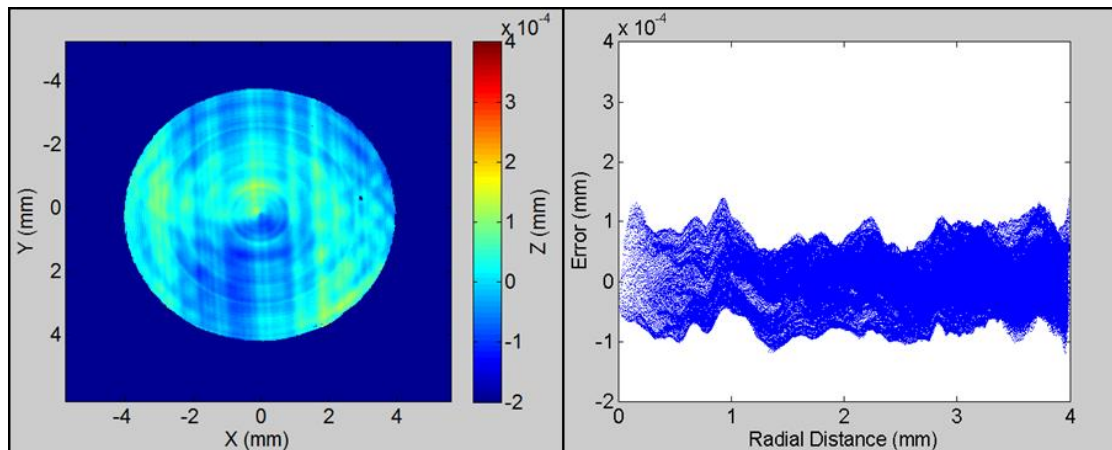


Figure 5.16: Final estimated residual Z error of a fully corrected calibration artifact. Compare to Figure 5.6 for the full affect.

5.5 Tool Path Generation

The theory behind the tool compensation described here is to compute the surface normal vector for every location on the surface to be machined. The points to be computed for the tool path are typically an array with element width as the stepover and

length as the feed per revolution. A surface describable by an equation of the form shown in Eq 5.1 will have a gradient vector, shown in Eq 5.2. The gradient vector also points in the direction normal to the surface at a given point (X, Y) . The normal direction to the surface is the direction the tool path must be offset in order to cut the select point. Figure 5.17 shows an example of the normal vector at various points on a circular profile.

$$Z = f(X, Y) \quad \text{Eq 5.1}$$

$$\vec{\nabla}f = \left\langle -\frac{\partial f}{\partial X}, -\frac{\partial f}{\partial Y}, 1 \right\rangle \quad \text{Eq 5.2}$$

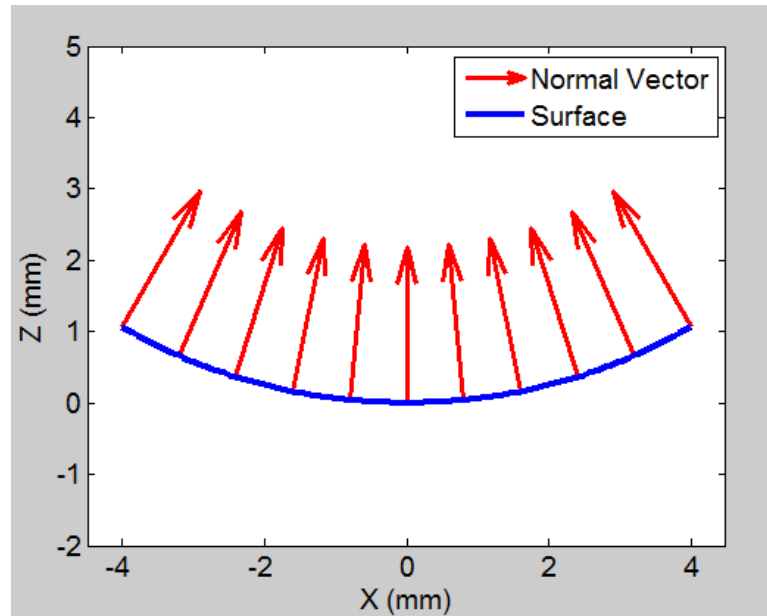


Figure 5.17: Example of normal vectors of a profile

Next the tool errors were compensated using the surface normal vector and the tool parameters. The typical tool/setup description must include: tool radius, spindle inclination, radial tool location offset, and an equation representing the edge waviness. These four tool setup parameters must be measured or assumed before starting the tool path generation.

The procedure for generating the tool compensated path for a calibration artifact is as follows:

1. Start with the tool parameters (tool radius, tool offset, spindle inclination, and tool waviness) and the surface equation. See Figure 5.18.

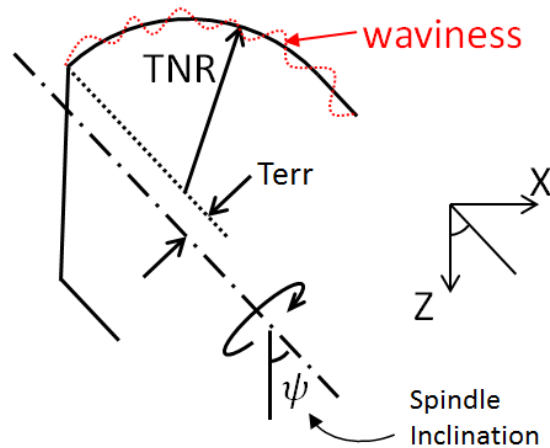


Figure 5.18: Tool parameters needed to compensate the tool path for the shape of the tool

2. Input the machining parameters: stepover, fpr, dimensions of the machining boundary (aperture), and direction of cut (up-milling or down-milling and raster direction). See Figure 5.19.

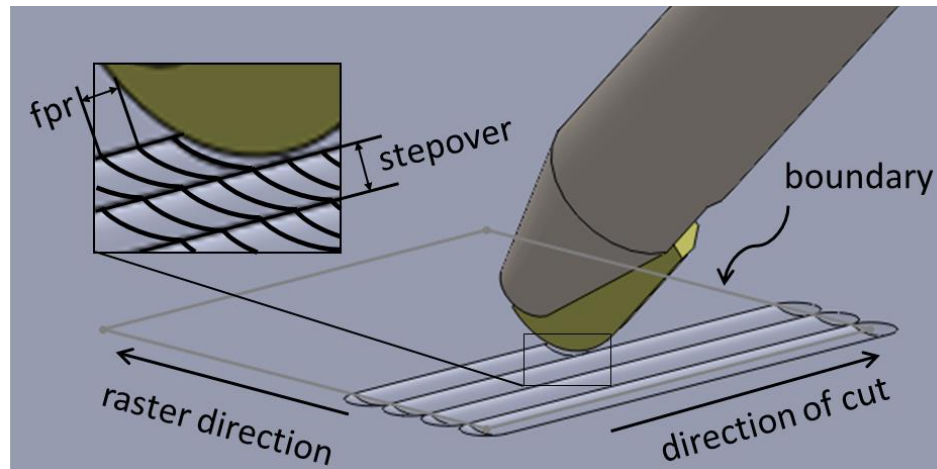


Figure 5.19: Machining parameters needed to generate a tool path: stepover, fpr, aperture, and directions of cutting

3. Generate the array of points of the desired cutting locations.
4. Compute the partial derivatives of the surface equation as a function of X and Y .
5. Assemble the gradient at each point of the surface shown in Eq 5.2.
6. Normalize the gradient by dividing each vector by its magnitude at the given spatial position.
7. Create a rotation matrix to transform the gradient vectors by the angle of the spindle inclination. This rotation will simplify the tool radial shifting correction by transferring the spindle rotation angle to the surface and utilizing the correction procedure as if the spindle were not rotated.
8. Rotate the normalized gradient vector.
9. Compute the tool compensation due to tool error location
 - a. Since all the correction will occur in the X - Y plane, zero the Z components of the normalized gradient and normalize again.

- b. Multiply the new Z-zeroed normalized gradient vector by the desired tool location error radial shift
10. Compute the tool compensation due to the edge waviness
 - a. Since the waviness correction will be made based on the slope of the surface relative to the tip of the tool, compute the component of the rotated normalized gradient that gives the length of the vector in the X-Y plane (referred to here as the radial component).
 - b. Normalize the radial component of the rotated normalized gradient vector to the Z component in order to simplify the relation to the slope of the tool to a single value at each point. This gives you the slope of the surface that the tool will experience, T_{slope} .
 - c. Using the T_{slope} , compute the magnitude of correction needed at each point using the equation for the waviness that is a function of slope.
 - d. Compute the waviness correction by multiply the magnitude of the waviness correction by the original rotated normalize gradient vectors.
11. Compute the compensation for the base radius of the tool by multiplying the rotated normalized gradient vectors by the tool nose radius.
12. Sum the rotated tool location error correction, waviness correction, and tool radius compensation.
13. Transform the summed tool compensation back to the machine orientation by rotating the opposite direction as the original rotation.

14. Add the tool compensation to the original points of the surface to get the tool compensated tool path for the surface.
15. Since the origin of the part is defined at longest part of the tool in the negative Z direction, offset the entire program by the distance from the most negative Z point of the tool to the center of the rotation of the tool, a tool radius from the tip. See Figure 5.20.

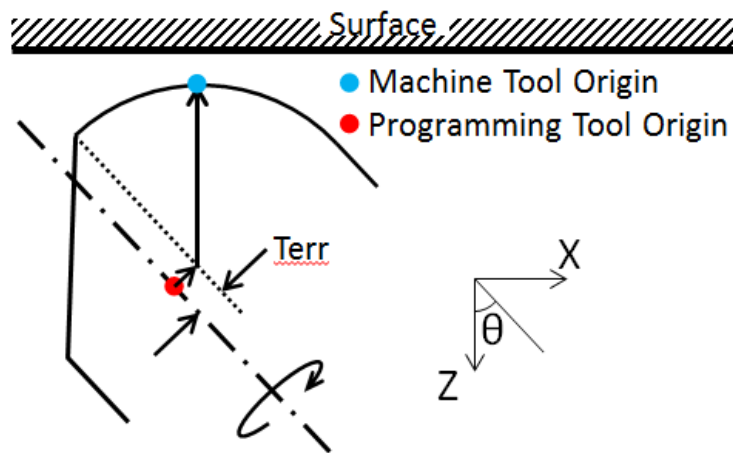


Figure 5.20: Diagram showing the relationship between the machine tool origin and the programming tool origin

5.6 Tool Path Validation

In order to confirm the tool path before actually cutting, a tool path validation program was written. The procedure of the validation code is given:

1. Describe the tool with an equation.
2. Create a surface with the desired resolution for X and Y and a height greater than the highest tool path point for Z .
3. Cycle through the tool path points and compute the tool shape at each tool path point.

4. Compare the surface to the tool shape at each point and keep the Z values that have the lowest value.
5. Filter the surface with a Gaussian filter to remove the cusps made by the feed, stepover, and tool shape.
6. Subtract the intended surface to see the deviation from the desired shape.
7. The filtering will not completely remove the surface roughness, so the purpose is to look for form errors and mid-spatial errors and ignore short wavelength features.

5.7 Additional Sources of Error

A source of tool error not covered in this dissertation is absolute tool radius. The artifact based technique is capable of measuring and correcting for tool radius; However, at the time of this dissertation, the radius measuring apparatus for the Zygo Verifire was not functioning. Another technique would be necessary to measure the radius of curvature of the artifact, because the Zygo Verifire only measures the departure from sphere. If we had two spheres with the same slope dependent error but different radius of curvatures, the Verifire could not distinguish between the two spheres.

The technique used during the process of preparing to make an actual optic was to use the on machine LVDT system to probe the sphere to measure the true radius of curvature. The LVDT probe had a 2mm diameter, but the steel ball used to calibrate the LVDT probe was damaged. Before the steel ball was damaged, the LVDT probe had been confirmed to be as good as or better than the steel ball. The other technique to confirm the tool radius was to program the artifact to have a very specific depth and

measure the diameter of the artifact's aperture. The radius of curvature can be found directly from the diameter of the aperture and depth of the apex using Eq 5.3.

$$ROC = \frac{Dia^2}{8 * Depth} + \frac{Depth}{2} \quad \text{Eq 5.3}$$

The ability to measure the artifact diameter with the on machine microscope has an uncertainty of about 1 μm . A 1 μm error in the aperture diameter equates to a 1.8 μm error in the tool radius.

An alternative method for measuring the artifact would be a profilometer. A calibrated sphere could be used to confirm calibration on the profilometer prior to measuring each artifact. A profilometer should be able to achieve a tool radius measurement on the order of 50-100 nm.

CHAPTER 6: APPLICATION

6.1 Making Optics

The culmination of extensive cutting tests and software development is making functioning optics. Using the results from various parameter tests to determine which parameters are most likely to achieve the necessary surface requirements of a functioning infrared optic. Cutting test results can be used to determine milling parameters for adequate surface quality. Error correction is used to map the tool and generate compensated machining code.

6.2 Aspheric Thermal Landscape Imaging Lens in IRG 26

The first proposed optic was an aspheric long wavelength infrared landscape imaging lens. The demonstration of raster milling was to show freeform capability, so for a first axisymmetric optic it was decided to add alignment features that, when combined with the optic, demonstrate the capability of freeform machining.

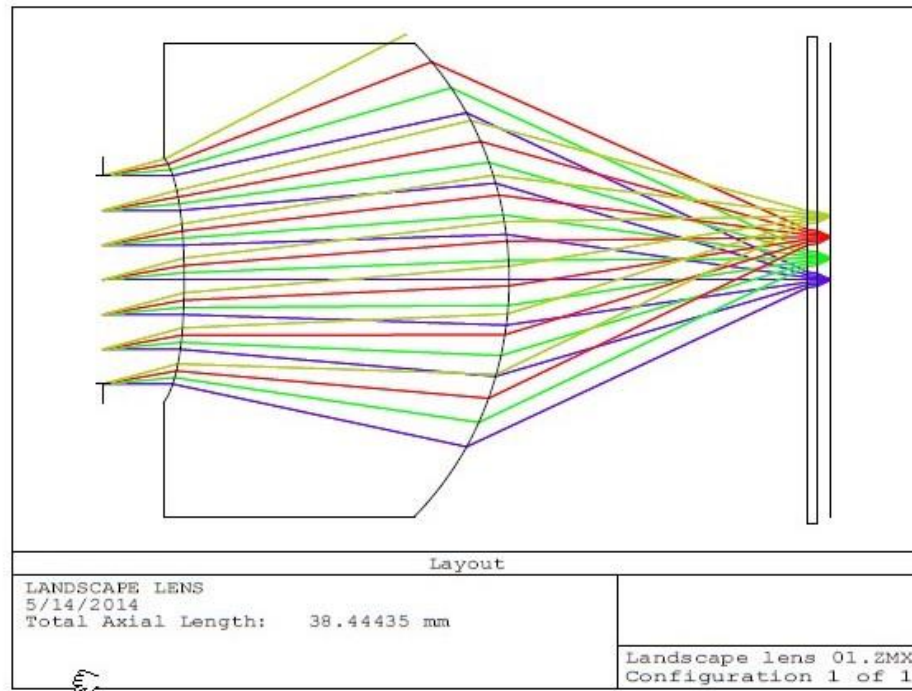


Figure 6.1: LWIR landscape lens ray trace diagram

The LWIR lens was designed and tested by David Schmidt at Rochester Precision Optics in Rochester, NY. The asphere was defined with a base radius and a polynomial equation. Here is the equation used to define the LWIR prescription:

$$Z = \frac{r^2}{ROC \left(1 + \sqrt{1 - \frac{r^2}{ROC^2}} \right)} + \sum_{i=1}^n A_i * r^{2i} \quad \text{Eq 6.1}$$

The variables in Eq 6.1 are: Z is the sagittal deviation, r is the radial distance from the centerline, ROC is the radius of curvature, and A is the set of coefficients of the aspheric polynomial. The parameters for the LWIR lens prescription are found in Table 6.1.

Table 6.1: LWIR lens prescription following Eq 6.1's naming convention, the values for Surface 2 will all be negative if you were to orient the optic to look directly at the surface instead of through Surface 1

| | Surface 1 | Surface 2 |
|-----|---------------|---------------|
| | concave | convex |
| ROC | 39.324 | 162.926 |
| A1 | 0 | -2.378170E-02 |
| A2 | -1.874820E-04 | -2.504970E-05 |
| A3 | 1.720550E-06 | 1.118830E-08 |
| A4 | -3.250080E-07 | -9.589650E-10 |
| A5 | 1.942756E-08 | 9.018070E-12 |
| A6 | -8.188120E-10 | -5.785620E-14 |
| A7 | 2.301425E-11 | 1.827476E-16 |
| A8 | -4.617730E-13 | -2.459020E-19 |
| A9 | 6.238525E-15 | 0 |
| A10 | -4.411110E-17 | 0 |

The machining process plan is outlined below:

1. Starting with a plano-plano blank with ground surfaces 20 mm thick and 25.4 mm diameter. (Figure 6.2)

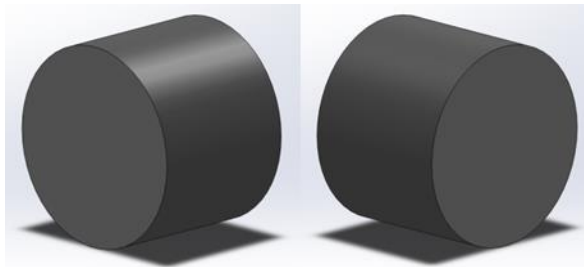


Figure 6.2: Rough blanks with ground surfaces, side 1 (left) and side 2 (right)

2. The blank was mounted on the vacuum chuck (and centered) and side 2 was diamond turned to a surface roughness of approximately 5 nm RMS. (Figure 6.3)

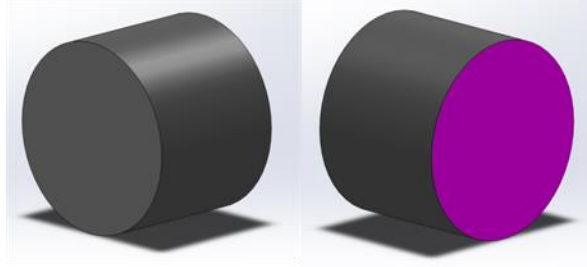


Figure 6.3: Side 2 diamond turned flat.

3. Before dismounting, the outer diameter was turned down from side 2 back 18.5 mm to a diameter of 25 mm. (Figure 6.4)

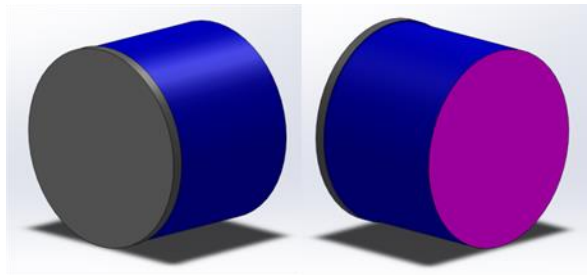


Figure 6.4: Turn front 18.5 mm of side 2

4. The blank was then flipped over (and centered) and side 1 was faced to a final thickness of 18.5 mm. This last facing pass will remove the extra diameter not machined in step 3. (Figure 6.5)

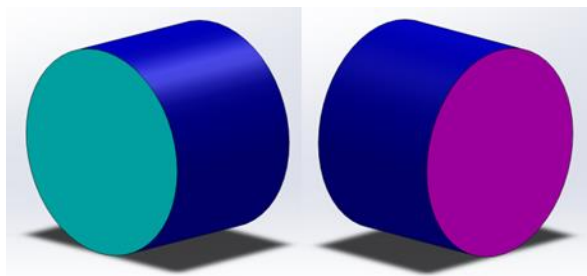


Figure 6.5: Flipped over and faced side 1

5. Mill the plano face of side 1 with a goal surface finish of 10 nm RMS. (Figure 6.6a)
6. Mill the kinematic features. (Figure 6.6b)

7. Rough and finish mill Surface 1 onto side 1. (Figure 6.6c,d)

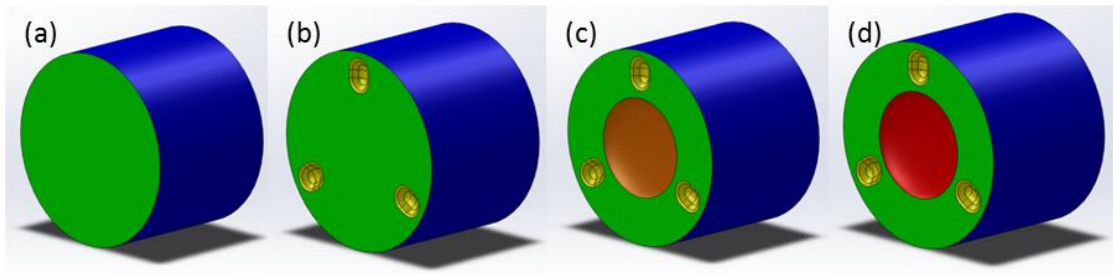


Figure 6.6: Milling side 1 process steps

8. Flip over and center to better than $1\ \mu\text{m}$ of run-out. (Figure 6.7a)

9. Rough and finish mill Surface 2 onto side 2. (Figure 6.7b,c)

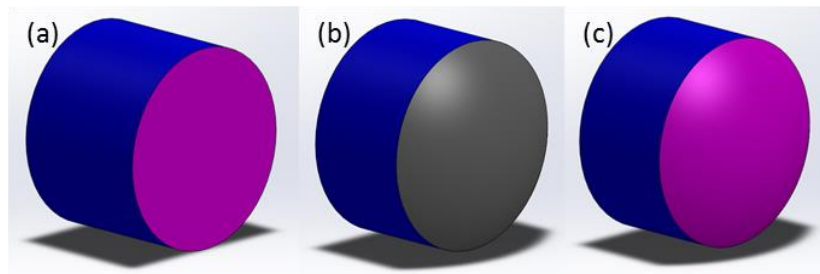


Figure 6.7: Milling side 2 process steps

The original design did not include any kinematic features, but in order to show true freeform capability and demonstrate possible mounting techniques three grooves were added on the concave lens side. A second part with three mating spheres was separately machined. As stated earlier a major advantage of combining optics with freeform surfaces is the ability to include alignment features with an optical surface *in one operation*. This transfers the accuracy of the manufacturing equipment to a monolithic opto-mechanical component.

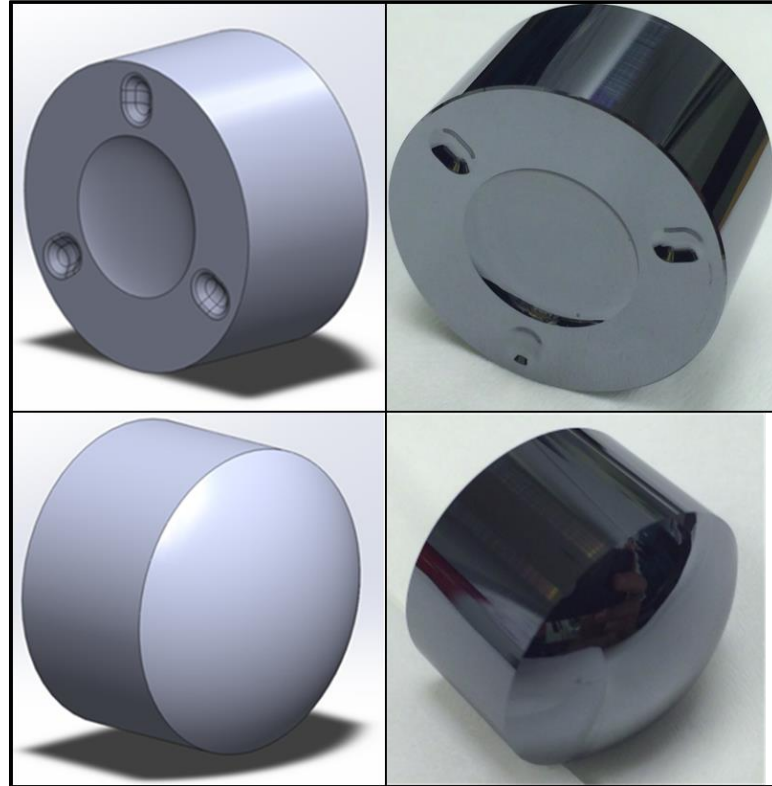


Figure 6.8: Modeled (left) and machined (right) LWIR landscape lens with kinematic features

6.2.1 Characteristics of Final Component

The maximum specified surface roughness was 30 nm with a goal surface roughness of 5 nm. The final measured surface roughness was between 5 nm and 10 nm. The specified figure error was less than 1 fringe meaning less than 632 nm peak-to-valley. At the time of this work, we did not have the capability to independently measure the form on site. However, preliminary measurements were made with the on machine linear variable differential transformer (LVDT) for surface 2 (Figure 6.7). The measurement procedure was to center the LVDT probe at the apex of the lens and then go to discrete X and Y position and plunge Z until the LVDT read zero. The machine positions were then recorded and a new (X,Y) position was selected, producing a point cloud of measurements. The results are shown in Figure 6.9.

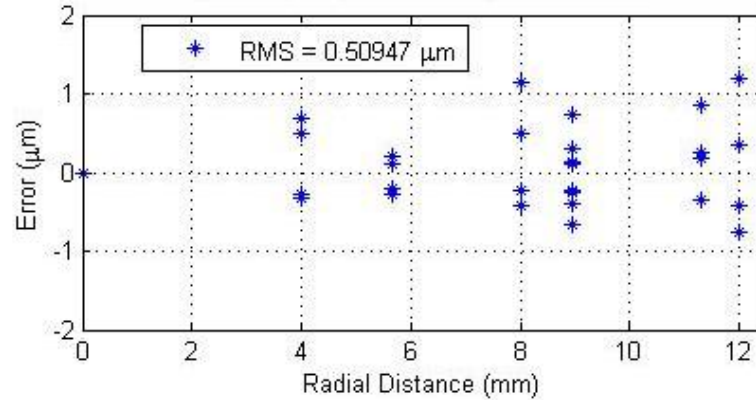


Figure 6.9: On machine LVDT measurements of Surface 2 assuming the LVDT probe is perfect

The on-machine measurements were within the desired form tolerance of 1 μm. Two more lenses were made after confirming the tool error correction and form error. One of the lenses was shipped to Rochester Precision Optics to be functionally tested. It was also measured at OptiPro using the OptiTrace 5000. The measurements showed that the surface 1 was on specification and surface 2 was out of specification. Figure 6.10 shows the analysis results from the OptiTrace 5000. Form tolerances were defined at 1 fringe using a wavelength of 632 nm. The errors shown in the measurements for surface 1 could have been corrected using a combination of improved tool radius measurement and diamond waviness tool compensation, but waviness compensation had not been developed at the time. Surface 2 showed significant errors that were both rotationally variant and rotationally invariant errors. The rotationally invariant errors could have been corrected with waviness compensation and improved measurement of the tool radius, but the rotationally variant errors were most likely due to machine drift, internal stresses in the material, either inherent or due to fixturing, or errors in mounting the part during the machining operations or during measurement.

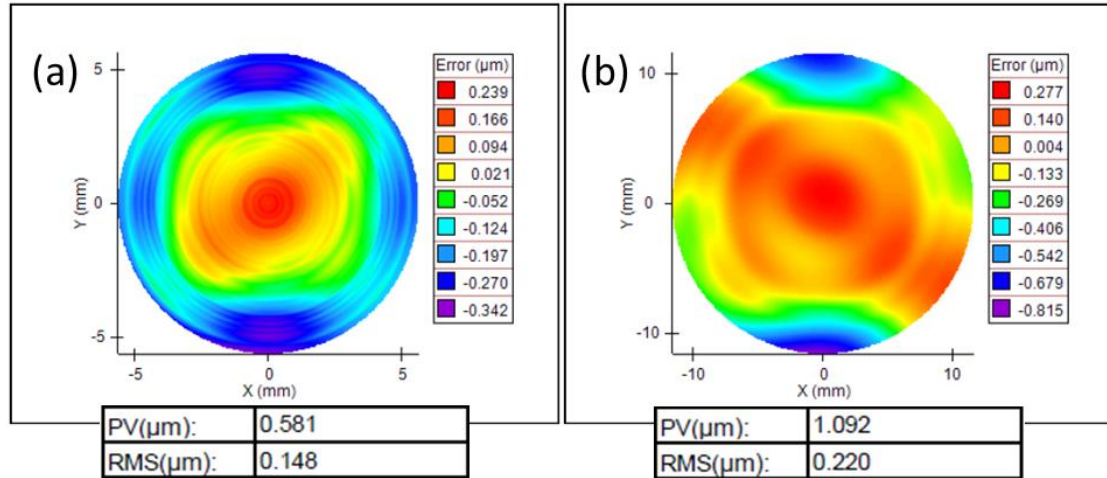


Figure 6.10: OptiPro measurement analysis of Surface 1 (a) and Surface 2 (b)

6.3 Higher Order Alvarez Freeform in IRG 26

Demonstrating a raster milled freeform was the ultimate goal of the work in IRG 26. After demonstrating the LWIR landscape asphere lens, we manufactured a functionally testable freeform. A modified Alvarez lens design was the design selected [60] [61]. An Alvarez lens is a pair of plano-freeform lenses. In the original Alvarez design, the freeform surfaces are identical and described by the cubic polynomial in Eq 6.2. The variables A and C are the Alvarez constant and the surface base height, respectively.

$$z_i(x, y) = Ax \left(\frac{x^2}{3} + y^2 \right) + C \quad \text{Eq 6.2}$$

When one surface is rotated by 180° relative to the other, and then the two surfaces face each other with the origins of the surfaces aligned, the composition of the lenses is a flat plano-plano lens with no focusing power. However, when the lenses are translated by an amount d along the equation x -direction the lens combination becomes a plano-concave or plano-convex lens depending on the direction of the translation d . The effective focal length of the lens system is defined by Eq 6.3.

$$f = \frac{1}{4Ad(n-1)} \quad \text{Eq 6.3}$$

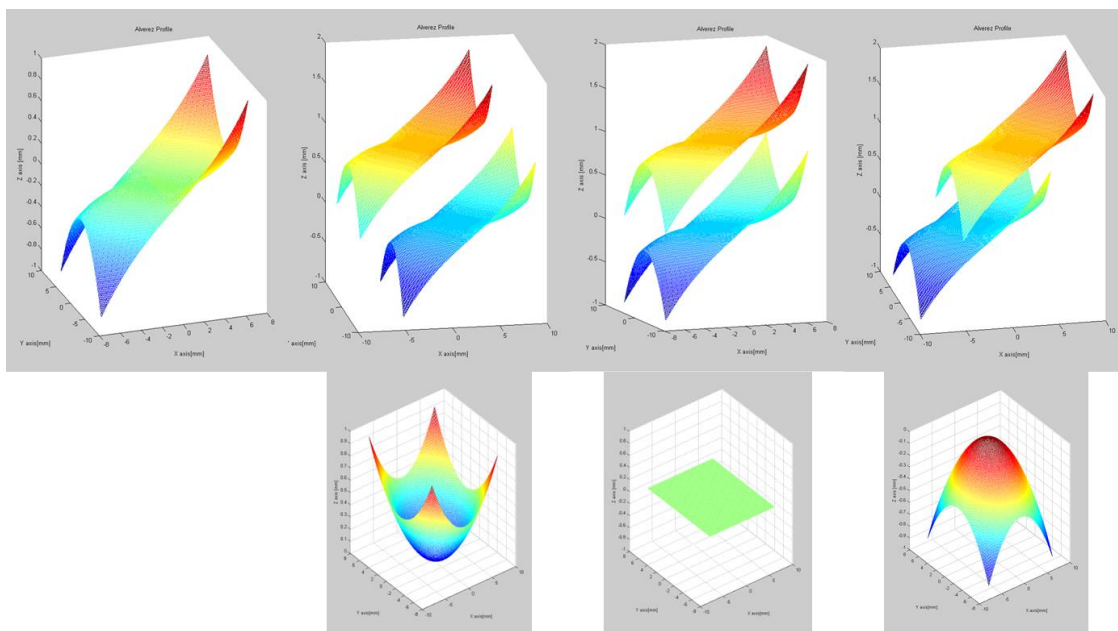


Figure 6.11: Alvarez lens surface with lateral shift and composite of the surfaces into a spherical lens

The nominal design has no power at zero shift and depending on the direction the power is either positive or negative. For functional testing of the focal length change, the negative power is not easily measured. Therefore, a design where the nominal, non-shifted position would have positive power and the shift would reduce or increase that positive power was chosen. The portion of the lens needed to make a negative power system was not useful for our application. Also, the use a ray tracing software could allow for the optimization of higher order terms.

Shultz et al. designed a high order Alvarez lens that was software corrected using Zemax®. As stated above the surface was designed so that negative power was not generated. This allowed the aperture size to be reduced and also for the overall surface

height variation to be minimized. In the final design a lateral shift of ± 1.8 mm led to a focal length change of the composite lens from infinity to 38.5 mm. An Alvarez lens has many possible applications particularly where small motions of optical components are needed to produce a rapid change in focal length. Example applications include thermal imaging, adjustable eye glasses, intraocular lens implants, etc. The optimized lens design is shown in Figure 6.12 which is a high order polynomial freeform. When laterally shifted the lens would go from zero power to a positive power through the full designed range. Including a base power reduced the amount of optical surface needed for the same aperture since the surface needed for the negative power side did not need to be included. This also helped to reduce the overall height of the optical surfaces.

Surface Equation

$$z_F(x, y) = \sum_{k=1}^n \frac{1}{2} a_{2k} (x^2 + y^2)^k + \sum_{k=1}^n b_{2k} \int (x^2 + y^2)^k dx + c_0 x$$

Freeform surface coefficients ($c_0 = 0.0262$)

| Order (k) | a_{2k} (mm^{-2k+1}) | b_{2k} (mm^{-2k}) |
|-----------|----------------------------------|--------------------------------|
| 1 | -3.62E-03 | -1.01E-03 |
| 2 | 8.50E-08 | 9.45E-08 |
| 3 | -4.00E-12 | -1.78E-11 |
| 4 | 2.88E-16 | 4.39E-15 |
| 5 | -1.61E-18 | -7.61E-18 |
| 6 | 2.31E-20 | 9.49E-20 |
| 7 | -1.31E-22 | -5.34E-22 |

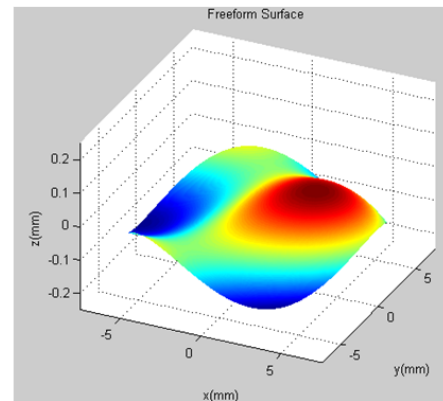


Figure 6.12: High order Alvarez lens design provided by Jason Shultz

The manufacturing plan for the Alvarez lens was similar to the LWIR landscape lens.

1. Create a solid model of the finished part.
2. Start with a ground blank.
3. Diamond turn the back side to a goal surface finish of 5 nm RMS.

4. Diamond turn the back 1 mm diameter down to 25 mm.
5. Flip part and diamond turn through the ground surface.
6. Turn a shelf into the front face leaving a 14.5 mm diameter platform in the middle with a 1mm thick locating “flange” surrounding it.
7. Raster diamond mill the alignment features.
8. Generate the tool path.
9. Rough and finish the Alvarez surface by raster diamond milling.

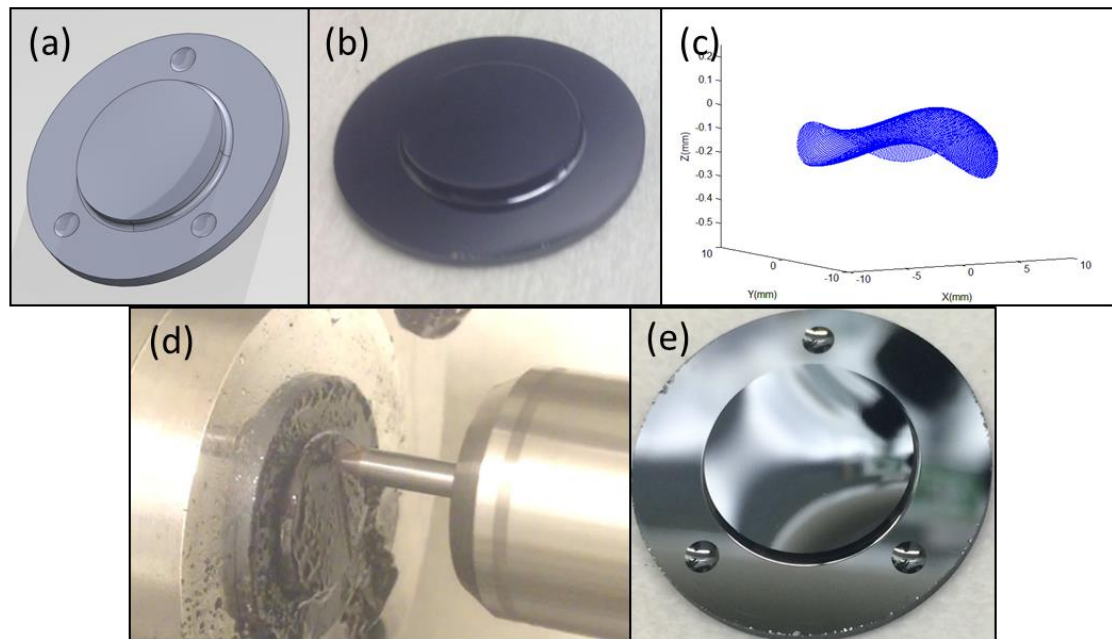


Figure 6.13: Alvarez lens manufacturing process: (a) step 1, (b) step 6, (c) step 8, (d) step 9, (e) finished part

Figure 6.13 demonstrates the manufacturing process and shows the final lens surface (Figure 6.13(e)). The final surface has been examined with SWLI and the average surface finish was found to be approximately 10 nm RMS. Mid spatial errors on the order of 150 nm with a wavelength of approximately 1 millimeter was also seen. This appears to be the result of thermal cycling in the milling spindle. Eliminating this is the subject of future work.

6.4 Extreme Freeform Twisted Pyramid

Spheres, aspheres, and mild freeforms are not good demonstrators of the true capability diamond milling brings to the infrared optics field. Following a programming error that resulted in a full slot with a 1.6 mm radius ball mill, approximately 4 mm deep, that only damaged the part when the steel shank hit the workpiece, we wanted to push the roughing parameters in IRG 26. A surface with no known optical function, but with true ‘freeform’ geometries was designed and machined in IRG 26. The shape is a seven tier, 7 mm tall twisting/spiraled pyramid. Each tier level was roughed at full depth (1 mm axial depth) with a radial stepover of 0.250 mm and a feed of 400 mm/min (0.010 mm/rev at 40,000 RPM). The material removal rate was 100 mm/min. That is double the typical roughing rate used in diamond turning a 1 inch disk of Al 6061 at UNC Charlotte. We believe that the material removal rate is limited by the tool geometry and not the material, evident by the specular surface achieved during the accidental full slot described above. The spiral pyramid can be seen in Figure 6.14.



Figure 6.14: Spiral pyramid extreme freeform diamond milling demonstration

CHAPTER 7: DISCUSSION AND CONCLUSIONS

7.1 Summary

This dissertation adds to the knowledge base for the cutting mechanics of IRG 26 and germanium. It has been shown that IRG 26 has a sharp transition in cutting forces around 700 nm to 900 nm when using a 0° rake tool. Forces drop by approximately 80% between 900 nm and 1000 nm chip thickness during a simplified, orthogonal cutting test (see Figure 3.1). It was also shown that in IRG 26 that the cutting force during a test cut depends on the quality of the surface prior to the test. For example, if a surface is free of fracture and is machined with aggressive parameters the force will start high and drop as the surface becomes more fractured due to the aggressiveness of the cut (see Figure 3.9). Orthogonal turning results were able to predict the force trends in round nose face turning, though the magnitude of the forces did not match (see Figure 3.16). Also, a set of parameters were found to achieve surface finishes suitable for IR optics in diamond ball milling.

In germanium orthogonal turning, we found a significant variation in forces as a function of cutting speed. For a 500 nm chip thickness, a drop of nearly 50% in the force level occurred when the speed was increased four times. (see Figure 4.19). Also, crystal orientation resulted in a force fluctuation of nearly 30% of the maximum force at 0.5 m/s speed and 200 nm chip thickness. There also appears to be a phase shift between the cutting and thrust force when observing the force fluctuation as a function of spindle/crystal orientation.

Tool errors have been modeled and corrected to reduce surface form errors from approximately 350 nm peak-to-valley down to approximately 50 nm. Mid-spatial errors

remain the dominate error in the artifact however the geometry of the mid-spatial errors is not correctable by modifying the tool geometry.

7.2 Future Work and Open Questions

7.2.1 High Speed Machining

We began to explore the cutting mechanics of these materials to better understand how to machine sharp periodic grooves on a surface. The results of initial testing opened up many other questions than just how to machine grooves. We realized that the mechanics could help to predict the forces of more complex machining operations like facing and milling. The results of the IRG 26 testing indicate that roughing forces could be significantly less than predicated from finishing parameters. Low roughing forces could mean faster roughing and faster prototyping. Also, knowing the transition depth from brittle surface to ductile when finish cutting could reduce the number of finish passes needed to leave a fracture free surface.

Would it be possible to take severely rough cuts (full tool radius depths ~ 1 mm) and finish cut with one pass at an optimized depth of cut based on the orthogonal turning information? Could we cut a 1 mm depth optic in one single pass using the finishing stepover and feed but with a full depth? These questions remain to be answered but if the answers are yes, then milling of IRG 26 could become quite competitive with molding for even medium batch production of optics. This leads to the question; can similar increases in speed be realized in other brittle materials, for example germanium or other chalcogenide glasses?

7.2.2 Dead Sharp Grooves

Understanding the behavior of orthogonal cutting in germanium led to a re-evaluation of the surface-tool interaction during dead sharp ruling tests. It was realized that the actual rake angle between the tool and the new surface would be significantly less than the rake between the tool and the uncut surface. As the included angle of the tool decreases the rake angle between the tool and the new surface is also reduced. In the case where a tool with an included angle of 30° is tilted to give a rake of -45° , the effective rake angle with the new surface is only approximately -15° . Also, the effective included angle is increased to about 42° . We have theorized that the tool needs to be tipped in the direction of the new surface not the direction of the old to obtain a high quality groove. Doing so would allow the cutting of the groove with a more “orthogonal-like” cutting operation where you were forming one side of the groove with the diamond edge and tracing the other side of the groove with only the tool tip. By tipping the tool towards, for example, the right side you effectively reduce the rake on the left side by as much as you increased the rake on the right side. This new view of the ruling operation allows direct use of the orthogonal cutting data to attempt to improve the fidelity of the ruled structures.

7.2.3 Speed Dependence

Germanium showed a dependency on speed at two different chip thicknesses. A full range of parameters for different speeds should be tested to better understand the variations. The IRG 26 did not show any speed dependency higher than 1 m/s at the parameters tested, but an open question is would smaller chip thicknesses exhibit a speed dependency higher than 1 m/s just as germanium did? Also, would slower speeds than 1

m/s show any speed dependencies in IRG 26 that were more conclusive than tests previously performed.

7.2.4 Fracture Depth Prediction

One question arising from the research is could orthogonal cutting be used to measure subsurface damage depth? For example, roughing parameters could be used to produce a surface and then finishing parameters could be used until the forces reach steady state indicating a ductile cut? This could be a way of testing the depth of fracture. For production purposes, it is also important to determine the maximum roughing parameters that still allow a minimal finish pass to remove subsurface damage.

7.2.5 Rake Angle Variations

A new testing configuration has also been proposed. This would allow the continuous adjustment of rake angle using a rotary axis during an orthogonal cutting test. This would provide data for a continuously changing rake angle and more quickly determine an optimum value for rake angle to produce the optimal cutting conditions. The normal and friction forces would be measured and the cutting and thrust forces could be computed. To the best of my knowledge, no one has changed the tool rake angle during the cutting operation in order to measure the change in forces.

7.2.6 Interrupted Cutting

Some milling parameters are 10 μm , it is unclear whether material behavior under these dynamics conditions is the same as in quasi-static conditions such as turning or indenting. We are developing an interrupted cutting apparatus that replicates the geometry in the orthogonal cutting but with variable time of contact. If the results are different, this may lead to new fundamental conclusions about material behavior under

dynamic loading conditions. From a practical prospective it could also lead to better understand of what materials can be milled to produce optical quality surfaces.

REFERENCES

- [1] KP Thompson and JP Rolland, "Freeform optical surfaces: A revolution in," *Optics and Photonics News*, 23(6):30-35, 2012.
- [2] BS Dutterer et al., "Diamond milling of an Alvarez lens in germanium," *Precision*, 38:398-408, 2014.
- [3] ML Barkman, BS Dutterer, MA Davies, and TJ Suleski, "Free-form machining for micro-imaging systems," *Proc. SPIE 6883, Advanced Fabrication Technologies for Micro/Nano Optics and Photonics*, p. 68830G, 2008.
- [4] MA Davies, BS Dutterer, TJ Suleski, JF Silny, and ED Kim, "Diamond machining of diffraction gratings for imaging spectrometers," *Precision Engineering*, 36(2):334-338, 2012.
- [5] GE Davis, JW Roblee, and AR Hedges, "Comparison of freeform manufacturing techniques in the production of monolithic lens arrays," *Proc. SPIE 7426, Optical Manufacturing and Testing VIII*, p. 742605, 2009.
- [6] PJ Smilie, BS Dutterer, JL Lineberger, MA Davies, and TJ Suleski, "Freeform micromachining of an infrared Alvarez lens," *Proc. SPIE*, 7927, 79270K, 2011.
- [7] PJ Smilie, BS Dutterer, JL Lineberger, MA Davies, and TJ Suleski, "Design and characterization of an infrared Alvarez Lens," *Optical Engineering*, 51(1):013006, 2012.
- [8] TJ Suleski, MA Davies, and BS Dutterer, "Diamond Machining of Freeform Infrared Optics," *Imaging and Applied Optics Technical Papers*, p. OW2D.4, 2012.
- [9] Rusnaldy, Tae Jo Ko, and Hee Sool Kim, "Micro-end-milling of single-crystal silicon," *International Journal of Machine Tools & Manufacture*, 47:2111-2119, 2007.
- [10] T Ono and M Takashi, "Influence of Tool Inclination on Brittle Fracture in Glass CUtting with Ball End Mills," *International Journal of Materials Processing Technology*, 202:61-69, 2008.
- [11] JC Morris, DL Callahan, J Kulik, JA Patten, and RO Scattergood, "Origins of the Ductile Regime in Single-Point Diamond Turning of Semiconductors," *Journal of the American Ceramic Society*, 78(8):2015-2020, 1995.

- [12] PN Blake and RO Scattergood, "Ductile-regime machining of germanium and silicon," *Journal of the American Ceramic Society*, 73(4): 949-957, 1990.
- [13] TG Bifano, PN Blake, TA Dow, and RO Scattergood, "Precision Finishing Of Ceramics," *Proc. SPIE 0803, Micromachining of Elements with Optical and Other Submicrometer Dimensional and Surface Specifications*, p. 12, 1987.
- [14] DA Lucca, P Chou, and RJ Hocken, "Effect of tool edge geometry on the nanometric cutting of Ge.," *CIRP Annals - Manufacturing Technology*, 47(1): 475-478, 1998.
- [15] JH Giovanola and I Finnie, "On the machining of glass," *Journal of Materials*, 15:2508-2514, 1980.
- [16] Osamu Horiuchi, Riyo Itabashi, and Yoshikazu Mitoma, "Diamond Turning of Single Crystal Germanium with and Oscillating Rotary Tool," *Advances in Abrasive Technology*, 238-239:395-398, 2003.
- [17] TP Leung, WB Lee, and XM Lu, "Diamond turning of silicon substrates in ductile regime ," *Journal of Materials Processing Technology*, 73(1-3):42-48, 1998.
- [18] RR Donaldson, CK Syn, JS Taylor, and RA Riddle, "Chip science: A basic study of the single point turning process.," *Thrust area report: Eng. Res. and Dev., LLNL UCRL-*, 53868-87:6.12-15, 1987.
- [19] FZ Fang and LJ Chen, "Ultra-Precision Cutting for ZKN7," *Annals of the CIRP*, 49(1):17-20, 2000.
- [20] C Jeynes et al., "Laterally resolved crystalline damage in single-point-diamond-turned silicon," *Nuclear Instruments and Methods in Physics Research B*, 118:431-436, 1996.
- [21] K Liu, XP Li, and SY Liang, "The mechanism of ductile chip formation in cutting of brittle materials," *International Journal of Advanced Manufacturing Technology*, 33:875-884, 2007.
- [22] T Shibata, S Fujii, E Makino, and M Ikeda, "Ductile-regime turning mechanism of single-crystal silicon," *Precision Engineering*, 18(2-3):129-137, 1996.
- [23] Y Takeuchi, K Sawada, and T Sata, "Ultraprecision 3D micromachining of Glass," *Annals of the CIRP*, 45/1:401-404, 1996.
- [24] (2015, March) II-VI Infrared. <http://www.iiviinfrared.com/Optical-Materials/optical->

materials.html.

- [25] D-S Bae, J-B Yeo, and H-Y Lee, "A study on a production and processing technique for a GeSbSe aspheric lens with a mid-infrared wavelength band," *Journal of the Korean Physical Society*, 62(11): 1610-1615, 2013.
- [26] WA Rogers, "A critical study of the action of a diamond in ruling lines upon glass," *Proceedings of the American Society of Microscopists, 6th Annual Meeting*, 5:149-165, 1883.
- [27] GF Ballou, "The Cornell Dividing Engine - 1," *American Machinist*, p. 18(13), 1895.
- [28] DB Marshal, BR Lawn, and AG Evans, "Elastic/Plastic Indentation Damage in Ceramics: The Lateral Crack System," *Journal of The American Ceramic Society*, 65(11):561-566, 1982.
- [29] BR Lawn and TR Wilshaw, "Indentation fracture: principals and applications," *Journal of Materials Science*, 10(6):1049-1081, 1975.
- [30] BR Lawn and AG Evans, "A model for crack initiation in elastic/plastic indentation fields," *Journal of Materials Science*, 12(11):2195-2199, 1977.
- [31] T Nakasuji et al., "Diamond turning of brittle materials for optical components.," *CIRP Annals – Manufacturing*, 39(1):89-92, 1990.
- [32] J Yan, K Maekawa, J Tamaki, and A Kubo, "Experimental study on the ultraprecision ductile machinability of single-crystal germanium.," *JSME Int. Journal*, 47(1): 29-36, 2004.
- [33] J Yan, K Maekawa, J Tamaki, and T Kuriyagawa, "Micro grooving on single crystal germanium for infrared Fresnel lenses," *J. Micromechanics and Microengineering*, 15: 1925-1931., 2005.
- [34] KE Puttick, MR Rudman, KJ Smith, A Franks, and K Lindsey, "Single-point diamond machining of glass," *Proceedings of the Royal Society of London A, Mathematical, Physical & Engineering Sciences*, 426(1870):19-30, 1989.
- [35] W-C Chiu, WJ Endres, and MD Thoules, "An experimental study of orthogonal machining of glass," *Machining Science and Technology*, 4(2):253-275, 1999.
- [36] WS Blackley and RO Scattergood, "Chip Topography for Ductile-Regime Machining of Germanium," *Journal of Manufacturing Science and Engineering*,

116(2), 263-266, 1994.

- [37] TG Bifano, TA Dow, and RO Scattergood, "Ductile-regime grinding: A new technology for machining brittle materials," *Journal of Engineering for Industry*, 113(2):184-189, 1991.
- [38] KE Puttick, LC Whitmore, P Zhdan, AE Gee, and CL Chao, "Energy scaling transitions in machining of silicon by diamond," *Tribology International*, 28(6):349-355, 1995.
- [39] BKA Ngoi and PS Sreejith, "Ductile regime finish machining - a review," *The International Journal of Advanced Manufacturing Technology*, 16(8):547-550, 2000.
- [40] I Ogura and Y Okazaki, "Ductile-regime machining of optical glasses by means of single-point diamond turning," *Journal of the Japan Society for Precision Engineering*, 66:1431-1435, 2000.
- [41] BR Lawn, *Fracture of Brittle Solids*, 2nd ed. US: Cambridge, 1993.
- [42] T Matsumura and T Ono, "Glass Machining with Ball End Mill," *Transactions of NAMRI/SME*, 33:319-326, 2005.
- [43] T Matsumura, T Hiramatsu, T Shirakashi, and T Muramatsu, "A Study on Cutting Force in the Milling Process of Glass," *Journal of Manufacturing Processes*, 7/2:102-108, 2005.
- [44] T Matsumura and T Ono, "Cutting Process of Glass with Inclined Ball End Mill," *Journal of Material Processing Technology*, 200:356-363, 2008.
- [45] K Foy, Z Wei, T Matsumura, and Y Huang, "Effect of tilt angle on cutting regime transition in glass micromilling," *International Journal of Machine Tools & Manufacturing*, 49:315-324, 2009.
- [46] M Arif, M Rahmen, WY San, and N Doshi, "An experimental approach to study the capability of end-milling for microcutting of glass," *International Journal of Advanced Manufacturing Technology*, 53:1063-1073, 2011.
- [47] M Arif, M Rehman, and WY San, "Analytical model to determine the critical feed per edge for ductile-brittle transition in milling process of brittle materials," *International Journal of Machine Tools & Manufacturing*, 51:170-181, 2011.
- [48] M Arif, M Rahman, and WY San, "Analytical model to determine the critical conditions for the modes of material," *Journal of Materials Processing Technology*,

212:1925-1933, 2012.

- [49] ME Merchant, "Mechanics of the Metal Cutting Process: I-Orthogonal Cutting and the Type 2 Chip," *Journal of Applied Physics*, 16:267-275, 1945.
- [50] EM Trent, *Metal Cutting*, 3rd ed. Oxford: Butterworth-Heinemann Ltd, 1991.
- [51] EJ Armarego and NP Deshpande, "Computerized predictive cutting models for forces in end-milling including eccentricity effects," *Annals of CIRP*, 38(1):45-49, 1989.
- [52] EJ Armarego and NP Deshpande, "Computerized end-milling forces prediction with cutting models allowing for eccentricity and cutter deflections," *Annals of CIRP*, 40(1):25-29, 1991.
- [53] Y Altintas and A Spence, "End Milling force algorithms for CAD Systems," *Annals of CIRP*, 40(1):31-34, 1991.
- [54] S Smith and J Tlusty, "An Overview of Modeling and simulation of the milling process," *Journal of Engineering for Industry*, 113:169-175, 1991.
- [55] Y Altintas and P Lee, "A general mechanics and dynamics model for ball end mills," *CIRP Annals – Manufacturing Technology*, 45(1):59-62, 1996.
- [56] OptiPro. (2015) <http://www.optipro.com/asphere-measurement.html>.
- [57] (02/11/2011) Dartmouth. <http://remf.dartmouth.edu/images/insectPart3SEM/>.
- [58] CG Bernhard, "Structural and functional adaptation in a visual system," *Endeavour*, 26:79-84, 1967.
- [59] B Macleod and G Sonek, "THIN FILMS - Motheye surfaces reflect little light," *Laser Focus World*, 35(8):109, 1999.
- [60] LW Alvarez, "Two-element variable-power spherical lens," US Patent 3,305,294, February 21, 1967.
- [61] LW Alvarez and WE Humphrey, "Variable-power lens and system," US Patent 3,507,565, April 21, 1970.

APPENDIX A: MATLAB CODE

MATLAB[®] was used to analyze and generate the necessary files for the setup sphere artifact. Many programs and sub-functions were used to perform the tasks of analyzing the measured sphere and generating the tool path to create the sphere. Here is the listed of necessary programs:

Table A.1: MATLAB[®] functions and sub-functions

| Program Name | Purpose |
|-----------------------------------------|----------------------------------------|
| Analyze_SetupSphere.m (Main) | Analyze the fizeau measurements |
| SetupSphere_ToolPath_Generator.m (Main) | Tool path generator |
| BestFitSphere.m (Sub) | Fit a radius of curvature to 3-D data |
| ROCKpoly.m (Sub) | Creates profile for asphere equation |
| ROCKpolySlope.m (Sub) | Computes slope of asphere equation |
| Torus_center_yawed_Zeroed.m (Sub) | Tool shape generator |
| Zernpolyfitn.m (Sub) | Zernike polynomial fitting |
| Zernpolyvaln.m (Sub) | Zernike polynomial generator |
| evenpolyval.m (Sub) | Even order polynomial generator |
| evenpolyfit.m (Sub) | Even order polynomial fitting |
| radiusCurvature.m (Sub) | Fit a radius of curvature to a profile |

A.1 Setup Sphere Analysis Code

```
% Setup Sphere Analyze Standard ROC=8mm, CA=8mm
% Author: Joseph Owen
% Date: 03/02/15

clear all
close all
tic

% data file must have X0, Y0, Z0 matrices in millimeters
load('IRG26SetupSphere_102914.mat');

% Sphere parameters
ROC=8; % Sphere Radius of Curvature
CA=8; % Clear aperture of the sphere cut

X=X0; % Initialize the working X variable
Y=Y0; % Initialize the working Y variable
```

```

% Centering the data on non-NaN heights
Xca=X; % Initialize temp X matrix
Yca=Y; % Initialize temp Y matrix
loc=isnan(Z0); % Find elements that have NaN values in the
Z data
Xca(loc)=NaN; % NaN all elements with a Z NaN
Yca(loc)=NaN; % NaN all elements with a Z NaN
X=X-nanmean(Xca(:)); % Center X data on non-NaN data
Y=Y-nanmean(Yca(:)); % Center Y data on non-NaN data
X0=X0-nanmean(Xca(:)); % Center X0 data on non-NaN data
Y0=Y0-nanmean(Yca(:)); % Center Y0 data on non-NaN data
% Xca=Xca-nanmean(Xca(:));
% Yca=Yca-nanmean(Yca(:));

% Plot Raw Data for inspection
surf(X,Y,Z0); shading interp
figure(1)
imagesc(1:1000,1:1000,Z0); h=colorbar; ylabel(h,'Z
(mm)', 'FontSize',14);
xlabel('X (pixel)');ylabel('Y (pixel)');
zlabel('Z (mm)');
set(findall(gca, 'type', 'text'), 'FontSize',14)
set(gca, 'FontSize',14)
% set(gca, 'Xtick', -4:2:4)
% set(gca, 'Ytick', -4:2:4)
% caxis([-0.0002 0.0004])

[Zern,CAr]=Zernpolyfitn(X,Y,Z0,1:4); % Find Piston,
Tip/tilt, and Power Zernike Terms
Z=Z0-Zernpolyvaln(Zern,X,Y,CAr); % Remove Piston,
Tip/tilt, and Power

% Plot Zernike Removed Data
figure(2)
imagesc(X(1,:),Y(:,1),Z); h=colorbar; ylabel(h,'Z
(mm)', 'FontSize',14);
xlabel('X (mm)');ylabel('Y (mm)');zlabel('Z (mm)');
set(findall(gca, 'type', 'text'), 'FontSize',14)
set(gca, 'FontSize',14)
set(gca, 'Xtick', -4:2:4)
set(gca, 'Ytick', -4:2:4)
caxis([-0.0002 0.0004])

%%

% Compute Polar Coordinates

```

```

R=(X.^2+Y.^2).^5; % Radial components
TH=atan2d(Y,X); % Angle components

figure(12)
plot(R(:),Z(:),'.','MarkerSize',1)
xlabel('Radial Distance (mm)');ylabel('Error (mm)');
set(findall(gca,'type','text'),'FontSize',14)
set(gca,'FontSize',14)
% legend('Error','PolyFit')
xlim([0 4])
ylim([-0.0002 0.0004])

% Trim all the values larger than the clear aperture
OB=R>CA/2; % elements outside the CA
X(OB)=NaN; % NaN X elements in OB
Y(OB)=NaN; % NaN X elements in OB
Z(OB)=NaN; % NaN X elements in OB
R(OB)=NaN; % NaN X elements in OB
TH(OB)=NaN; % NaN X elements in OB

Zbase=ROCKpoly(R,ROC,0,0); % Create the base sphere
(reMOVED by transmission sphere)

Zact=Zbase+Z; % Actual surface of part

plot(R(:),Z(:))
plot(R(:),Zact(:))

% Comparison plots
figure(3)
subplot(1,2,1)
surf(X,Y,Z); shading interp;
xlabel('X (mm)');ylabel('Y (mm)');zlabel('Z (mm)');
set(findall(gca,'type','text'),'FontSize',14)
set(gca,'FontSize',14)
set(gca,'Xtick',-4:2:4)
set(gca,'Ytick',-4:2:4)
zlim([0 1.2])
% axis equal
view([1 1 .3])
subplot(1,2,2)
surf(X,Y,Zact); shading interp;
xlabel('X (mm)');ylabel('Y (mm)');zlabel('Z (mm)');
set(findall(gca,'type','text'),'FontSize',14)
set(gca,'FontSize',14)
set(gca,'Xtick',-4:2:4)

```

```

set(gca, 'Ytick', -4:2:4)
zlim([0 1.2])
% axis equal
view([1 1 .3])
% caxis([-0.0002 0.0004])

%% Radial Shifting
% shift=0.0015:0.00002:0.0017;
snom=0;      % starting nominal shift
smult=3;    % number of values on each side of shift
sdiff=ROC/CA*(max(Z(:))-min(Z(:)))*8; % start spacing
between shifts using the Nanotech X-Shift estimate
colors={'b','g','k','r','c','m','b','g','k','r','c','m'};
PVlimit=1e-5;
loop=0;

while(1)
    loop=loop+1;      % loop counter
    shift=(-smult*sdiff:sdiff:smult*sdiff)+snom; % Next
iteration shift
    PV=zeros(size(shift)); %Initialize PV
    disp(['loop ', num2str(loop)])

    for i=1:length(shift)
        Rnew=R+shift(i); % Shift Radial Distance
        Rnew(Rnew<0)=0; % Remove negative R values
        Xnew=Rnew.*cosd(TH); % Cartesian
        Ynew=Rnew.*sind(TH); % Cartesian
        ROCfit=BestFitSphere(Xnew(:),Ynew(:),Zact(:)); %
Best Fit Sphere
        Zfit=ROCKpoly(Rnew,ROCfit,0,0); % Generated Best
Fit Sphere
        Zstretch=Zact-Zfit; % New error after shift
        % Uncomment if you wish to watch the M or W
changing
        %{
        figure(4)

plot(Rnew(:).*TH(:)./abs(TH(:)),Zstretch(:),[colors{i},'.']
)
        ylim([-0.010 0.010])
        hold on
        pause(.01)
        %}
        shift(i);

```

```

        PV(i)=max(Zstretch(:))-min(Zstretch(:));    %
Compute PV
        PV(i);
    end

    nomloc=find(PV==min(PV));    % element of minimum PV
    lowB=nomloc-1;    % element to left of nomloc
    if(lowB==0); lowB=1; end    % check if element exists
    highB=nomloc+1; % element ot right of nomloc
    if(highB>length(PV)); highB=length(PV); end % check if
element exists

    % If neighboring shifts are less than PVlimit from
minimum, break loop
    if( max(PV(lowB:highB))-min(PV(lowB:highB)) < PVlimit);
        break;
    end

    snom=shift((PV==min(PV)));    % Value of shift at minimum
PV
    sdiff=sdiff/smult;    % Set new shift spacing for next
iteration
end
hold off
%{
figure(4)
% legend('-0.010','-0.006','-
0.002','0.002','0.006','0.010');
h0=legend('-0.004','-0.0035','-
0.003','0.0025','0.002','0.0015','0.001','0.0005','0.0000')
;
% set(h0,'FontSize',10)
xlabel('Radial Distance (mm)')
ylabel('Z height (mm)')
set(gca,'Xtick',-4:2:4)
xlim([-4 6])
%}
% Plot final shifting iteration
figure(5)
plot(shift,PV,'o-','LineWidth',3,'MarkerSize',10)
xlabel('shift (mm)');ylabel('PV (mm)');
set(findall(gca,'type','text'),'FontSize',14)
set(gca,'FontSize',14)
%%
% Post shift correction preparation for slope correction
Terr=shift((PV==min(PV)));    % Set X-shift to best value
found above

```

```

Rnew=R+Terr;      % Radial shift values by Terr
Rnew(Rnew<0)=0;  % Eliminate any negative Radial values
Xnew=Rnew.*cosd(TH);    % Polar to Cartesian
Ynew=Rnew.*sind(TH);    % Polar to Cartesian
ROCfit=BestFitSphere(Xnew(:),Ynew(:),Zact(:)); % Compute
Best fit ROC of new R-shifted data
Zfit=ROCKpoly(Rnew,ROCfit,0,0); % Generate best fit ROC to
remove
Zshifted=Zact-Zfit; % Z error as would be measured on
Fizeau after radial correction (simulated)

% Plot residual error after R-shifting
figure(6)
plot(R(:),Zshifted(:),'.','MarkerSize',1)
xlabel('Radial Distance (mm)');ylabel('Residual Waviness
(mm)');
set(findall(gca,'type','text'),'FontSize',14)
set(gca,'FontSize',14)

% Plot before and after R-shifting
figure(7);
plot(R(:),Zact(:),'-',Rnew(:),Zact(:),'-','LineWidth',2)
xlabel('Radial Distance (mm)');ylabel('Z Height (mm)');
set(findall(gca,'type','text'),'FontSize',14)
set(gca,'FontSize',14)
legend('original','shifted')
axis equal

%% Slope Error Fitting
%
Slope=ROCKpolySlope(R,ROC,0,0); % Slope using the nominal
sphere geometry
Angle=atan2d(Slope,1); % Angle computed from slope

temp=~isnan(Zshifted(:)); % find non-NaN values for
fitting
ToolError=polyfit(Slope(temp),Zshifted(temp),8); %
polynomial fit to residual slope dependent error
Zsmooth=polyval(ToolError,Slope); % Generated polynomial
from above fit

% Overlaid error and polynomial fit
figure(9)
plot(Slope(:),Zshifted(:),'.',Slope(:),Zsmooth(:),'r','Line
Width',5,'MarkerSize',20)
xlabel('Slope (mm)');ylabel('Error (mm)');
set(findall(gca,'type','text'),'FontSize',14)

```

```

set(gca, 'FontSize', 14)
legend('Error', 'PolyFit')
xlim([0 max(Slope(:))])

% simulated residual error after final correction
Zcorrected=Zshifted-Zsmooth;

% Plot Final residual error
figure(10)
plot(Rnew(:), Zcorrected(:), '.', 'MarkerSize', 1)
xlabel('Radial Distance (mm)'); ylabel('Error (mm)');
set(findall(gca, 'type', 'text'), 'FontSize', 14)
set(gca, 'FontSize', 14)
% legend('Error', 'PolyFit')
xlim([0 4])
ylim([-0.0002 0.0004])

% Plot final residual error 3D map
figure(11)
imagesc(X0(1, :)-
nanmean(Xca(:), Y0(:, 1)+nanmean(Yca(:)), Zcorrected);
h=colorbar; ylabel(h, 'Z (mm)', 'FontSize', 14);
xlabel('X (mm)'); ylabel('Y (mm)'); zlabel('Z (mm)');
set(findall(gca, 'type', 'text'), 'FontSize', 14)
set(gca, 'FontSize', 14)
set(gca, 'Xtick', -4:2:4)
set(gca, 'Ytick', -4:2:4)
caxis([-0.0002 0.0004])

% Height parameters with No Slope Error
SDnse=nanstd(Zcorrected(:))*10^6
PVnse=(nanmax(Zcorrected(:))-nanmin(Zcorrected(:)))*10^6

toc

```

A.2 Setup Sphere Tool Path Generator

```

clear all;
close all;
tic

CA=8; % Clear Aperture
TNR=1.5789; % Tool nose radius
Terr=-0.00144; % tool mounting error

Tslope=-[-5.57580861674416; % Slope dependent tool error
polynomial fit
    8.72695409905091;
    -3.36082742132256;
    -0.959384603514789;
    0.888259403161751;
    -0.174792982147409;
    0.0111225640729522;
    -0.000972807932473773;
    0.000278219587710996];

fittingtype='odd'; % fitting type (either 'odd' or 'even')

yaw=0; % Yaw
stepover= 0.20; % raster stepover
fpr=0.20; % Spacing in the y-direction between points
RPM=40000; % Estimated RPM
raster='both'; % up/down milling or 'both'
% filename for output nc program
filename=[pwd, 'SetupSphereCode.nc'];
write=0; % 1=write, 0=do not write

% Symbolic equations to compute the partial derivatives
syms X Y ROC; % Create symbolic variables
f=((X.^2+Y.^2)./(ROC*(1+(1-(X.^2+Y.^2)/ROC^2).^5))); %
Function of a sphere
fx=diff(f,X); % partial x derivative
fy=diff(f,Y); % partial y derivative
g=matlabFunction(f); % convert to actual function
gx=matlabFunction(fx); % convert to actual function
gy=matlabFunction(fy); % convert to actual function
disp('Created Surface Equation')
toc % timer output
clear X Y ROC f fx fy % Clear symbolic variables

```

```

yp0=1; % plot basic figures
yp=0; % plot tool path vectors
yp2=0; % plot tool operation graphic
dx=stepover; %CA/50; % stepover
dy=fpr; %CA/50; % feed/rev
x0=-CA/2:dx:CA/2; % x axis values
y0=-CA/2:dy:CA/2; % y axis values
[X0,Y0]=meshgrid(x0,y0); % X-Y plane matrix

OB=X0.^2+Y0.^2>(CA/2)^2; % Out of Bounds
X0(OB)=NaN; % NaN OB values
Y0(OB)=NaN; % NaN OB values

X=X0; % initialize X
Y=Y0; % initialize Y

if strcmp(raster,'both') % adjusted X,Y tool path for
raster preference
    for i=2:2:length(x0)
        X=X0; % X doesn't change
        Y(:,i)=flipud(Y0(:,i)); % every other Y column
    flips
    end
end

ROC=8; % Radius of Curvature
Zlens=g(ROC,X,Y); % Surface being created

if yp0;
    figure(1);surf(X,Y,Zlens);shading interp;
    xlabel('X (mm)'); ylabel('Y (mm)'); zlabel('Z
(mm)');title('Surface');
end % plot surface if yp

x=X(:); % Columnize
y=Y(:); % Columnize
x(isnan(x))=[]; % Remove NaN's
y(isnan(y))=[]; % Remove NaN's
z=g(ROC,x,y); % Surface SAG
fx=gx(ROC,x,y); % x partial derivative
fy=gy(ROC,x,y); % y partial derivative

TSR=TNR+Terr; % Tool swing radius ( only used for Torus
comp )

fz=ones(length(fx),1); % z partial derivative (set to 1 at
all locations)

```

```

grad=[-fx,-fy,fz]; % Gradient
mag=(fx.^2+fy.^2+fz.^2).^5; % Gradient Magnitude at each
point
gradn=grad./[mag,mag,mag]; % Normalized Gradient

%% Align yawed Terr vectors with the X-Y plane for
simplified calculations
angle=-yaw; % Milling inclination angle: CCW=negative and
CW=positive
Ry=[cosd(angle) 0 sind(angle); % Rotation Matrix forward
    0 1 0;
    -sind(angle) 0 cosd(angle)];

if yp;figure;
    quiver3(x,y,z,gradn(:,1),gradn(:,2),gradn(:,3));view([0
-1 0]);
    title('TNR gradient unit vectors at each position');
    xlabel('X (mm)'); ylabel('Y (mm)'); zlabel('Z (mm)');
end

grady=(Ry*gradn)'; % Rotated gradient to simplify Terr
vector

grady_r=(grady(:,1).^2+grady(:,2).^2).^5; % Vector length
in the XY plane (radial component)
grady_z=grady(:,3); % Vector length in the Z direction

grady_r_z1=grady_r./grady_z; % radial component normalized
so that the Z component equals 1 so that a single value can
be passed into the slope error fit equation

if yp;
    figure;
    quiver3(x,y,z,grady(:,1),grady(:,2),grady(:,3));view([0
-1 0]);
    xlabel('X (mm)'); ylabel('Y (mm)'); zlabel('Z (mm)');
    title('TNR gradient unit vectors Rotated to match
yaw');
end

% Terr vector in the X-Y plane
grady_noz=zeros(size(grady)); % initialize gradient to zero
grady_noz(:,1:2)=grady(:,1:2); % Assign values
mag_noz=sum(grady_noz.^2,2).^5; % Magnitude of each vector
grady_nozn=grady_noz./[mag_noz,mag_noz,mag_noz]; %
Normalize vectors
TNRcomp=TNR*grady; % Vector and length due to TNR

```

```

if strcmp(fittingtype, 'even');
    SCMag=SMet.evenpolyval(Tslope,grady_r_z1); % magnitude
of the slope dependent correction
elseif strcmp(fittingtype, 'odd')
    SCMag=polyval(Tslope,grady_r_z1);
end

Tslopecomp=grady.*[SCMag,SCMag,SCMag]; % X, Y, Z components
of the tool error due to waviness
Terrcomp=Terr*grady_nozn; % Vector and length due to Terr
Terrcomp(isnan(Terrcomp))=0; % Remove any NaN's

tempcomp=TNRcomp+Terrcomp+Tslopecomp; % Full Vector of tool
comp

%% Rotate vectors back to standard Machine Coordinates
angle=yaw; % Rotation Angle: opposite of above angle
Ry=[cosd(angle) 0 sind(angle); % Rotation Matrix Backward
    0 1 0;
    -sind(angle) 0 cosd(angle)];

R_TNRcomp=(Ry*TNRcomp)'; % TNR partial Tool Comp
R_Terrcomp=(Ry*Terrcomp)'; % Terr partial Tool Comp
ToolComp=(Ry*tempcomp)'; % Total Tool Comp

xt_cent=x+ToolComp(:,1); % Final X comped
yt_cent=y+ToolComp(:,2); % Final Y comped
zt_cent=z+ToolComp(:,3); % Final Z comped

if yp;
    figure;

quiver3(x,y,z,ToolComp(:,1),ToolComp(:,2),ToolComp(:,3));vi
ew([0 -1 0]);
    xlabel('X (mm)'); ylabel('Y (mm)'); zlabel('Z (mm)');
    title('Full Tool Comp vector')
end

if yaw==0
    xt=xt_cent; % Adjust Torus center for actual touchoff
point
    yt=yt_cent;
    zt=zt_cent-TNR; % match depth to touch off = 0.000
else

```

```

        xt=xt_cent+Terr*cosd(yaw); % Adjust Torus center for
actual touchoff point
        yt=yt_cent;
        zt=zt_cent-TNR-Terr*sind(yaw); % match depth to touch
off = 0.000
end
disp('Finished generating tool path')
toc
%% Plot tool along path demonstration

if yp2;
    xtemp=-TSR:TSR/100:TSR; % tool display spacing
    [Xtemp,Ytemp]=meshgrid(xtemp,xtemp); % matrixize

[Xn,Yn,Zn]=Torus_center_yawed_Zeroed(Xtemp,Ytemp,TNR,TNR+Te
rr,yaw,1); % Torus shape comped for touchoff position
    %
[Xn,Yn,Zn]=Torus_center_yawed(Xtemp,Ytemp,TNR,TSR,yaw); %

    xfin=-CA/2:CA/500:CA/2; % Surface values
    [Xfin,Yfin]=meshgrid(xfin,xfin); % Surface Matrix
    Zfin=g(ROC,Xfin,Yfin); % Surface SAG
    Zfin(SRSS(Xfin,Yfin)>=CA/2)=NaN;
    for i=1:length(x(:))

        if
i/round(length(x(:))/50)==round(i/round(length(x(:))/50))
            figure(5);
            surf(Xfin,Yfin,Zfin);shading interp % Surface
            hold on
            % Torus Tool Comp vectors for TNR and Terr

plot3([x(i),x(i)+R_TNRcomp(i,1),x(i)+R_TNRcomp(i,1)+R_Terrc
omp(i,1)],...

[y(i),y(i)+R_TNRcomp(i,2),y(i)+R_TNRcomp(i,2)+R_Terrcomp(i,
2)],...

[z(i),z(i)+R_TNRcomp(i,3),z(i)+R_TNRcomp(i,3)+R_Terrcomp(i,
3)]);

            surf(Xn+xt(i),Yn+yt(i),Zn+zt(i)); % Tool
            plot3(0,0,3.5)
            axis([-CA/2 CA/2 -CA/2 CA/2 -5 5]); % axis

equal

            % view([-1 -1 -1]);
            hold off

```

```

        pause(0.1);
    end

    Zsurf=g(ROC,Xn+xt(i),Yn+yt(i)); % Surface SAG based
on tool values
    Diff=Zn+zt(i)-Zsurf; % Difference between tool and
SAG
    touch(i)=min(Diff(:)); % Point of contact occurs at
minimum distance
    end
    figure;plot(touch(:));
    xlabel('X (mm)'); ylabel('Y (mm)'); zlabel('Z (mm)');
    title('Error is due to the coarse resolution of the
generated tool');
end

if yp0
    figure;
    plot3(xt,yt,zt)
    xlabel('X (mm)'); ylabel('Y (mm)'); zlabel('Z (mm)');
    title('Tool Path');
    view([0 -1 0]);

    ROCfit3=SMet.BestFitSphere(xt,yt,zt,0);
    Zfit3=SMet.ROCKpoly((xt.^2+yt.^2).^5,ROCfit3,0,0);
    zres=zt-Zfit3;

    figure
    plot((xt.^2+yt.^2).^5,zres,'.')

    figure
    plot3(xt,yt,zres)
end

%% Write NC file
%
if write
    fid=fopen(filename,'wt+');
    fprintf(fid,'%\nG1 Z%8.6f F100\n',zt(1)+10);
    fprintf(fid,'X%8.6f Y%8.6f F500\n',xt(1),yt(1));
    fprintf(fid,'Z%8.6f F100\n',zt(1)+1);
    fprintf(fid,'Z%8.6f F20\n',zt(1));
    fprintf(fid,'G4 P5\n()\n');
    fprintf(fid,'F%4.3f\n',fpr*RPM);
    for i3=1:length(xt)
        fprintf(fid,'X%8.6f Y%8.6f
Z%8.6f\n',xt(i3),yt(i3),zt(i3));
    end
end

```

```

end
fprintf(fid, 'Z%8.6f \n', zt(1)+1);
fprintf(fid, 'Z%8.6f F500\n', zt(1)+10);
fprintf(fid, 'M99\n');
fclose(fid);
disp('Finished Writing NC program')
toc
end
%}

```

A.3 Best Fit Sphere

```

%% Program Name: BestFitSphere.m
%% -----
-----
% Best Fit Sphere
% Author: Joseph Owen
% Date: 03/02/15

function ROCfit=BestFitSphere(X,Y,Z)
R=(X.^2+Y.^2).^5;      % Radial Component
CAr=max(R(:));        % Clear aperture
P=evenpolyfit(R,Z,14); % 14th order even polynomial fit
x=-CAr:CAr/500:CAr;   % new x vector
circ=evenpolyval(P,x); % Smoothed profile
ROCfit=radiusCurvature(x,circ); % radius of curvature
estimator

```

A.4 ROCKpoly

```

%% Program Name: ROCKpoly.m
%% -----
-----
% Asphere equation
% Author: Joseph Owen
% Date: 03/02/14
function z = ROCKpoly(x,ROC, k, a2_16)
% z = ROCKpoly(x,ROC, k, a2_16)
% x is radial distance from origin.  If X and Y input,
x=(X.^2+Y.^2).^5
% a2_16 is an array of the 16 order polynomial terms with
the first index of x^2

zpoly=0;
for i=1:length(a2_16)

```

```

        zpoly=zpoly+a2_16(i)*x.^(2*(i));
end

z=(x.^2/ROC)./(1+(1-(1+k)*(x/ROC).^2).^5)+zpoly;

end

```

A.5 ROckpolySlope

```

%% Program Name: ROckpolySlope.m
%% -----
-----
% Asphere equation slope
% Author: Joseph Owen
% Date: 03/02/14
function zSlope = ROckpolySlope(x,ROC, k, a2_16)
% a2_16 is an array of the 16 order polynomial terms with
the first index of x^2

zpolySlope=0;
for i=1:length(a2_16)
    zpolySlope=zpolySlope+(2*i)*a2_16(i)*x.^(2*(i)-1);
end

% zSlope=x.*(2*ROC^2*((1-
(k+1).*x.^2/ROC^2).^5+1)+(k+1).*x.^2/(1-
(k+1).*x.^2/ROC^2).^5) ...
%      ./ (ROC^3*((1-(k+1).*x.^2/ROC^2).^5+1).^2) ...
%      + zpolySlope;

zSlope= (x/ROC)./(1-(k+1)*(x/ROC).^2).^5 ...
        + zpolySlope;

end

```

A.6 Torus_center_yawed_Zeroed

```

%% Program Name: Torus_center_yawed_Zeroed.m
%% -----
-----
% Simulated tool shape of a diamond tool
% Author: Joseph Owen
% Date: 03/02/14
function
[Xn,Yn,Zn]=Torus_center_yawed_Zeroed(X,Y,TNR,TSR,yaw,ytrim)

```

```

% Inputs:   X and Y matrices
%           TNR is the tool nose radius
%           TSR is the torus sweep radius (cross-sectional
radius)
%           yaw si the tool inclination angle
%           ytrim is the command to trim the trim the
excess torus
% Outputs:  Xn, Yn, Zn matrices of the tool torus shape

r=abs(TNR);
R=TSR-TNR;

if nargin < 6
    ytrim=0;
end

if TNR == TSR
    % Basic Sphere
    Z= (X.^2+Y.^2) ./ (TNR*(1+(1-(X.^2+Y.^2)/TNR^2).^5))-
abs(r)-abs(R);
else
    Z=abs(r)-(r^2-(R-(X.^2+Y.^2).^5).^2).^5-abs(r); %
main axis of Torus along Z
end

temp=real(Z) ~= Z; % find complex numbers
X(temp)=NaN;
Y(temp)=NaN;
Z(temp)=NaN;

X=X-(TSR-TNR); % Center the tool based on the shifts

% Rotate the tool by the spindle inclination
Ry=[cosd(yaw) 0 sind(yaw); % Rotation Matrix
    0 1 0;
    -sind(yaw) 0 cosd(yaw)];

[nx,ny]=size(X);

Temp=Ry*[X(:)';Y(:)';Z(:)'];
Xn=reshape(Temp(1,:),nx,ny);
Yn=reshape(Temp(2,:),nx,ny);
Zn=reshape(Temp(3,:),nx,ny)+abs(r);

figure;surf(Xn,Yn,Zn);shading interp; axis equal
xlabel('X');ylabel('Y');zlabel('Z');

```

```

% If desired, trim the excess parts of the torus
if ytrim
    slopepex=atan2d(diff(Zn,1,2),diff(Xn,1,2));
    slopepex1=[zeros(nx,1),slopepex];
    slopepex2=[slopepex,zeros(nx,1)];
    slopepy=atan2d(diff(Zn,1,1),diff(Yn,1,1));
    slopepy1=[zeros(1,ny);slopepy];
    slopepy2=[slopepy;zeros(1,ny)];
    trimAngle=90.1-yaw;
    trim=abs(slopepex1) > trimAngle | abs(slopepex2) >
trimAngle | abs(slopepy1) > trimAngle | abs(slopepy2) >
trimAngle;
    Xn(trim)=NaN;
    Yn(trim)=NaN;
    Zn(trim)=NaN;
    [a1,b1]=find(abs(Yn)==min(min(abs(Yn))));
    [a2,b2]=find(Xn==min(min(Xn)));
    Zn(Zn >= Zn(a1(1),b2(1))-.15)=NaN;
end

```

A.7 Zernpolyfitn

```

function [ Zern,CA2 ] = Zernpolyfitn(
X0,Y0,Z0,terms,CAr,cutoff,method )
%Takes in X, Y, Z Matrices with or without NaNs in Z and
gives back the
%Zernike terms you requested or first 38 if not requested
% created by: Joseph Owen
% References: wikipedia.com
% Detailed explanation goes here

if nargin < 4
    terms=1:38;
end

X=X0(:); % matrix to column vector
Y=Y0(:); % matrix to column vector
Z=Z0(:); % matrix to column vector

Znans=isnan(Z); % Locate NaNs in the Z data
X(Znans)=[]; % Remove NaNs
Y(Znans)=[]; % Remove NaNs
Z(Znans)=[]; % Remove NaNs

```

```

rho=(X.^2+Y.^2).^5; % Radial Polar Component
psi=atan2(Y,X); % Angular Polar Component

if nargin < 5
    CAR=max(rho);
end

j=max(terms); % Initialize j to the largest term used

rho=rho/CAR; % Normalize Radius

TZ=zeros(length(rho),max(terms)); % Initialize TZ to
zeros
modes=Zernike_modes(j); % convert j to standard n and m
nodes
n=modes(:,1);
m=modes(:,2);

% create generic terms
for i=1:length(terms)

TZ(:,terms(i))=Zern_Polynomials(rho,psi,n(terms(i)),m(terms
(i)));
end

if nargin < 7
    method=1;
end

% find best coefficients for the Zernike Terms provided
if method==2
    Zern=pinv(TZ)*Z;
else
    Zern=TZ\Z;
end
if nargin < 6
    cutoff = 10^-10;
end

Zern(abs(Zern)<cutoff)=0; % Set all coefficients less than
an Angstrom to zero

if nargin > 1

```

```

        CA2=CAr;
    end

end

function modes=Zernike_modes(j)
% find the n and m modes of the Zernike Polynomials and
order them the way
% Zemax prefers them by magnitude of m and n

temp_mode=zeros(j*j,2); % Initialize modes

% find many more terms so they can be sorted and selected
for i=2:j*j
    n=temp_mode(i-1,1);
    m=temp_mode(i-1,2);
    if m>0
        temp_mode(i,:)=[n,-m];
    elseif abs(m)+2 <= n
        temp_mode(i,:)=[n,abs(m)+2];
    elseif abs(m)+2 > n
        if ~rem((n+1),2) % check n+1 for even
            temp_mode(i,:)=[n+1,0];
        else
            temp_mode(i,:)=[n+1,1];
        end
    end
end
end

mag=[temp_mode,sqrt(temp_mode(:,1).^2+temp_mode(:,2).^2)];
mag2=sortrows(mag,3);
modes=mag2(1:j,1:2); % Select the first j terms after
sorting
end

function Z=Zern_Polynomials(rho,psi,n,m)

R=0; % Initialize R to zero
msign=0; % set msign to zero
if m~=0
    msign=m/abs(m); % find sign on m
end
m=abs(m); % make m positive

% rotationally invariant Zernike terms
for k=0:(n-m)/2

```

```

    R=R+(-1)^k*factorial(n-
k)/(factorial(k)*factorial(0.5*(n+m)-k)*factorial(0.5*(n-
m)-k))*rho.^(n-2*k);
end

% rotationally variant Zernike terms
if msign>=0
    angle=cos(m*psi);
else
    angle=sin(m*psi);
end

Z=R.*angle; % combine each part

end

```

A.8 Zernpolyvaln

```

function [ Z ] = Zernpolyvaln( coeff,X0,Y0,CAr)
%Takes in X, Y, Z Matrices with or without NaNs in Z and
gives back the
%first 11 Zernike terms
% created by: Joseph Owen
% References: wikipedia.com
% Detailed explanation goes here

j=length(coeff);
% terms=1:j;

[a,b]=size(X0);

X=X0(:); % matrix to column vector
Y=Y0(:); % matrix to column vector

rho=(X.^2+Y.^2).^0.5; % Radial Polar Component
if nargin < 4
    CAr=max(rho);
end
rho=rho/CAr; % Normalize Radius
psi=atan2(Y,X); % Angular Polar Component

TZ=zeros(length(rho),j); % Initialize

modes=Zernike_modes(j); % find first j modes
n=modes(:,1);
m=modes(:,2);

```

```

% create zernike polynomials
for i=1:j
    TZ(:,i)=Zern_Polynomials(rho,psi,n(i),m(i))*coeff(i);
end

Z=reshape(sum(TZ,2),a,b);

end

function modes=Zernike_modes(j)
% find the n and m modes of the Zernike Polynomials and
order them the way
% Zemax prefers them by magnitude of m and n

temp_mode=zeros(j*j,2); % Initialize modes

% find many more terms so they can be sorted and selected
for i=2:j*j
    n=temp_mode(i-1,1);
    m=temp_mode(i-1,2);
    if m>0
        temp_mode(i,:)=[n,-m];
    elseif abs(m)+2 <= n
        temp_mode(i,:)=[n,abs(m)+2];
    elseif abs(m)+2 > n
        if ~rem((n+1),2) % check n+1 for even
            temp_mode(i,:)=[n+1,0];
        else
            temp_mode(i,:)=[n+1,1];
        end
    end
end
end

mag=[temp_mode,sqrt(temp_mode(:,1).^2+temp_mode(:,2).^2)];
mag2=sortrows(mag,3);
modes=mag2(1:j,1:2); % Select the first j terms after
sorting
end

function Z=Zern_Polynomials(rho,psi,n,m)

R=0; % Initialize R to zero
msign=0; % set msign to zero
if m~=0

```

```
    msign=m/abs(m); % find sign on m
end
m=abs(m); % make m positive

% rotationally invariant Zernike terms
for k=0:(n-m)/2
    R=R+(-1)^k*factorial(n-
k)/(factorial(k)*factorial(0.5*(n+m)-k)*factorial(0.5*(n-
m)-k))*rho.^(n-2*k);
end

% rotationally variant Zernike terms
if msign>=0
    angle=cos(m*psi);
else
    angle=sin(m*psi);
end

Z=R.*angle; % combine each part

end
```